Laser-Driven Acceleration of Gold Ions at the Centre for Advanced Laser Applications

Laura Desiree Geulig

München 2025

Laser-Driven Acceleration of Gold Ions at the Centre for Advanced Laser Applications

DISSERTATION

an der Fakultät für Physik der

Ludwig-Maximilians-Universität München

vorgelegt von

Laura Desiree Geulig

geboren in Aschaffenburg

München, den 16.09.2025

Erstgutachter: Prof. Dr. Peter G. Thirolf
Zweitgutachter: Prof. Dr. Jörg Schreiber
Tag der mündlichen Prüfung: 17.11.2025

Zusammenfassung

Die Mehrheit von Elementen schwerer als Eisen wird durch die Nukleosynthese über Neutroneneinfangprozesse gebildet, gefolgt von einem β^- Zerfall, durch den Neutronen in Protonen umgewandelt werden und so für die Entstehung schwerer Elemente verantwortich sind. Beim schnellen Neutroneneinfang (r-Prozess) erfolgt die Anlagerung von Neutronen schneller als der gegenläufige β^--Zerfall, wodurch Isotope weit abseits des Tals der Stabilität erzeugt werden. Bahnbrechende Beobachtungen der LIGO-Virgo Kollaboration im Jahr 2017 etablierten die Verschmelzung von Neutronensternen als eine bedeutende astrophysikalische Quelle des r-Prozesses. Eine präzise Modellierung dieses Prozesses erfordert jedoch experimentelle Daten zu den Kerneigenschaften der beteiligten Isotope. Von besonderem Interesse sind dabei Isotope in der Nähe des Wartepunkts bei der magischen Neutronenzahl von N=126, der maßgeblich die Entstehung von Aktiniden bestimmt.

Aus diesem Grund schlugen Habs *et al.* das Fission-Fusion Reaktionsschema vor, das auf der laserbasierten Beschleunigung schwerer, spaltbarer Ionen wie zum Beispiel von Thorium oder Uran beruht. In diesem Konzept werden die Ionen auf ein zweites Target aus demselben Material beschleunigt und induzieren dabei Kernspaltung. Die resultierende asymmetrische Fragmentverteilung liefert ein schweres Fragment sowie ein leichtes, neutronenreiches Fragment. Durch die Fusion zweier solcher leichter, neutronenreicher Spaltfragmente kann ein Kern nahe des Wartepunkts bei N=126 entstehen. Dies wird ermöglicht durch die hohen Teilchendichten, die mit laserbasierter Beschleunigung erreichbar sind.

Aufbauend auf früheren Arbeiten, in denen die Beschleunigung schwerer Ionen oberhalb der Spaltbarriere bei etwa 7 MeV/u demonstriert wurde, wurde der Versuchsaufbau in dieser Thesis in die High-Fields Kammer (HF) am Centre for Advanced Laser Applications (CALA) in Garching übertragen. Wie in den vorangegangenen Kampagnen wurde Gold als Stellvertreter für Aktiniden eingesetzt, worduch strahlenschutzrechtliche Auflagen vermieden werden konnten, während vergleichbare Beschleunigungseigenschaften erwartet werden.

Oberflächenverunreinigungen auf den dünnen Goldfolien unterdrücken die effiziente Beschleunigung von Goldionen. Daher wurde ein verbessertes Heizsystem implementiert, welches es ermöglicht, die Temperatur des Targets durch Anpassung des Planckschen Strahlungsgesetzes an das emittierte Infrarotspektrum zu bestimmen. Der Unterschied in der Beschleunigung zwischen erhitzten und nicht erhitzten Targets wurde für die

Laserpulsparameter des ATLAS-3000-Systems untersucht. Darüber hinaus wurden zwei Ansätze zur Online-Detektion schwerer Ionen getestet, um die hohen Schussraten moderner Lasersysteme wie des ATLAS-3000 zu nutzen. Schließlich wurden überraschende Signale schwerer Ionen beobachtet, deren Masse-zu-Ladungsverhältnis typischerweise nur von leichten Ionen erreicht werden kann und für Goldionen nicht zugänglich ist. Diese Signale konnten als Spaltfragmente von Gold identifiziert werden. Die vorliegende Arbeit untersucht daher potenzielle Mechanismen, die für diese Spaltung von Goldionen verantwortlich sein könnten.

Abstract

The majority of elements heavier than iron are produced through nucleosynthesis via neutron-capture processes, followed by β^- decay that converts neutrons into protons, thus producing heavier elements. For the rapid neutron capture (r-)process the accumulation of neutrons is faster than the counteracting β^- decay, producing isotopes far off the valley of stability. Groundbreaking observations of the LIGO-Virgo collaboration in 2017 established neutron star mergers as a major astrophysical site of the r-process. However, accurate modeling of this process requires experimental data on the nuclear properties of isotopes. Of special interest are isotopes around the waiting point at N=126, which governs the formation of actinides.

Therefore, Habs *et al.* proposed the fission-fusion reaction scheme enabled by the laser-based acceleration of heavy, fissile ions like thorium or uranium. In this concept, ions are accelerated onto a second target of the same material, hereby inducing fission. The resulting asymmetric fragment distribution produces a heavy fragment and a light, neutron-rich fragment. The fusion of two neutron-rich, light fission fragments can create a nucleus close to the waiting point at N=126, enabled by the high particle densities achievable by laser-based acceleration.

Building on earlier work that demonstrated the acceleration of heavy ions above the fission barrier at about 7 MeV/u, in the course of this thesis the experimental setup was transferred to the High Fields (HF) cave at the Centre for Advanced Laser Applications (CALA) in Garching. As for previous campaigns, gold was employed as a proxy for the acceleration of actinides, avoiding any safety regulations concerning radiation protection while similar acceleration characteristics are expected.

Surface contaminants on the thin gold foils suppress the efficient acceleration of the heavy ions. Therefore an improved heating system was implemented, allowing to determine the temperature of the target by fitting Planck's law to the emitted infrared spectrum. The differential acceleration for heated and unheated targets was investigated for the laser pulse parameters of the ATLAS-3000 system. Furthermore, two approaches for online detection of heavy ions were tested, aiming to exploit the high repetition rate capabilities of state-of-the-art laser systems like the ATLAS-3000. Finally, the surprising observation of heavy ion signals with a mass-to-charge ratio typically only attained by light ions and not reachable by gold ions were analyzed and identified as fission fragments of gold. This thesis therefore investigates potential mechanisms being responsible for this fission of gold ions.

Contents

List of Figures

List of Tables

Abbreviations

ASE Amplified Spontaneous Emission
CALA Centre for Advanced Laser Applications
CMOS Complementary Metal-Oxide Semiconductor
CPA Chirped Pulse Amplification
cw continuous wave
EMP Electromagnetic Pulse
FOP Fiber Optical Plate
FWHM Full-Width at Half-Maximum
HDR High Dynamic Range
HF High Field
LBD Laser Beamline Delivery
MCPs Microchannel Plate Detectors
NIR Near Infrared
OAP Off-Axis Parabolic Mirror
PET Polyethylene terephthalate
PIC Particle-In-Cell
r-process rapid neutron capture process
sCMOS scientific CMOS
Ti:Sa Titanium-doped Sapphire
TPS Thomson parabola spectrometer
TPW Texas Petawatt laser
XFA X-ray Fluorescence Analysis

1. Introduction

With the invention of chirped pulse amplification (CPA) by Strickland and Mourou in 1985 [1], new intensity regimes became accessible. Systems exceeding peak intensities of $1 \cdot 10^{18}\,\mathrm{W/cm^2}$, where the motion of electrons in the electric field becomes relativistic, became readily available (compare for example Ref. [2]) reaching peak intensities of up to $10^{23}\,\mathrm{W/cm^2}$ [3]. With the commissioning of the BErkeley Lab Laser Accelerator (BELLA) in 2012, intensities at the petawatt level could be produced at repetition rates of 1 Hz [4], improving the understanding of the experiments compared to a few shots per day in previous laser setups.

Current efforts mostly focus on the development of new particle and light sources by using intense laser pulses for the acceleration of electrons, protons and other light ions. More exotic goals are pursued applying the novel opportunities provided by high-power short pulse lasers (with high repetition rates) such as probing the quantum vacuum [5] via multiphoton Breit-Wheeler pair production [6], photon-photon scattering [7] as well as acceleration of heavier ions in dense bunches.

While the acceleration of electrons relies on stimulating wakefields in an underdense plasma, nowadays reaching energies of up to 10 GeV [8], the acceleration of ions relies on the interaction of the laser pulse with a near-critical to over-critical target. The first proposal of plasma-based ion acceleration was already made in the 1950s [9], until protons with more than 10 MeV were measured by groups at the Nova Petawatt Laser in Livermore [10] and the Vulcan laser at the Rutherford Appleton Laboratory [11] around the year 2000.

The ions accelerated by lasers exhibit properties that complement acceleration by conventional Radio Frequency (RF) accelerators. Multiple species with multiple charge states are simultaneously accelerated, accompanied by the emission of neutrons, X-rays and relativistic electrons [12, 13], featuring a large range of applications [14]. The most investigated and robust scheme is target normal sheath acceleration (TNSA) featuring a broad energy distribution, with a characteristic cutoff energy. More advanced acceleration mechanisms like radiation pressure acceleration (RPA) promise a more efficient conversion of laser energy with narrower bandwidth of the energy spectra and up to solid state like densities of the accelerated bunches [12, 13].

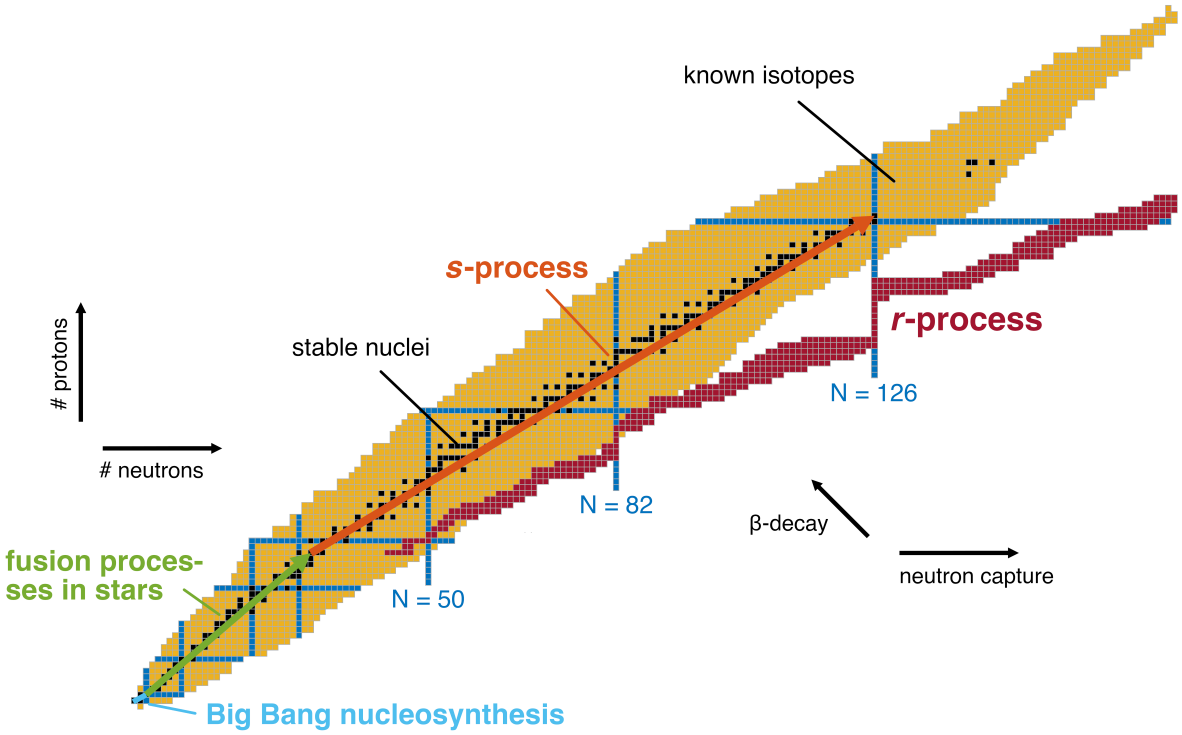

Figure 1.1.: Chart of nuclides including the location of magic neutron and proton numbers (i.e. closed nucleon shells) marked in blue. Stable nuclei are indicated in black, other known and unstable nuclei are marked in yellow. The primordial elements generated during the Big Bang nucleosynthesis are indicated in light blue, the pathway via thermonuclear fusion processes in stars in green and the s-process (slow neutron capture process) in orange. The assumed pathway of the production of heavy elements via the r-process (rapid neutron capture process) runs deep in the terra incognita of nuclei, far away from the valley of stability, indicated by red squares. Image taken from Ref. [15].

One of the proposed applications includes the fission-fusion reaction mechanism, proposed by Habs *et al.* [16], which is also the broader motivation for this thesis, aiming at gaining a deeper understanding of the nucleosynthesis of the heaviest elements in the universe. During the Big Bang, only light elements, including ^{4}He, D, ^{3}He and ^{7}Li were produced, largely dominated by hydrogen and ^{4}He, with abundances of 75 % and 25 %, respectively [17], indicated in light blue in Fig. 1.1. Thermonuclear fusion processes in stars are then responsible for the generation of heavier elements up to iron, where the binding energy inside the nucleus reaches a maximum [18] (green arrow in Fig. 1.1).

The generation of elements heavier than iron occurs via neutron capture processes in competition with β^- decay, converting the neutron into a proton. By this, the nucleus first moves to the right on the chart of nuclei and then moves up diagonally to the left

by the β^- decay, as indicated by the two black arrows in Fig. 1.1. By repeating this process, heavier elements can get created.

While the β^- decay is an inherent property of the specific nucleus, the neutron capture rate strongly depends on the neutron density. A neutron density of 10^6 to $10^{10}\,\mathrm{cm}^{-3}$ is considered low and the neutron capture rate is slow compared to the β^- decay. In such an environment, a captured neutron will decay before the next neutron is captured. This process is termed slow neutron capture (s-)process and follows the valley of stability up to polonium (^{210}Po) which decays by an α-decay into lead (^{206}Pb) before it captures further neutrons. This effectively leads to a cycle around lead, bismuth and polonium [19].

For the production of naturally abundant elements heavier than polonium, like thorium or uranium, astrophysical sites with very high neutron densities around $10^{23}\,\mathrm{cm}^{-3}$ are necessary. Here the neutron capture is much faster than the competing β^- decay. A nucleus can capture multiple neutrons before the decay to protons, leading it far away from the valley of stability, as indicated by the red squares in Fig. 1.1. This process is termed rapid neutron capture (r-)process.

The exact astrophysical site was under discussion for decades [20]. In 2017, along with the groundbreaking observation of a gravitational wave, the LIGO-Virgo collaboration detected spectroscopic signatures of a kilonova, powered by the synthesis of large amounts of very heavy elements via the r-process [21,22]. This provided evidence that neutron star mergers are the major site of r-process nucleosynthesis. This view has been confirmed by subsequent reviews, though work is still ongoing (and in need of experimental data) to refine existing models [23]. The consequence of lacking experimental data for theoretical models is well illustrated by Fig. 1.2, presenting the differences in the mass predictions of different theoretical models and experimental data as a function of the number of neutrons N of cesium isotopes (Z=55), using the Duflo-Zucker model (light orange line) as a reference. While the predictions by theories agree rather well in the region of known masses, differences between models quickly reach up to more than 20 MeV outside the region of data availability.

Of special interest are the nuclear properties close to the magic neutron numbers at N=50, 82 and 126, presenting closed neutron shells in the nuclei. As a consequence, the neutron capture cross section is significantly reduced, leading to a slowing down of the nucleosynthesis and an accumulation of elemental abundances. As such, the magic neutron numbers create so-called waiting points for the creation of heavier elements, acting as bottlenecks for the nuclear reaction networks used to model the r-process pathways.

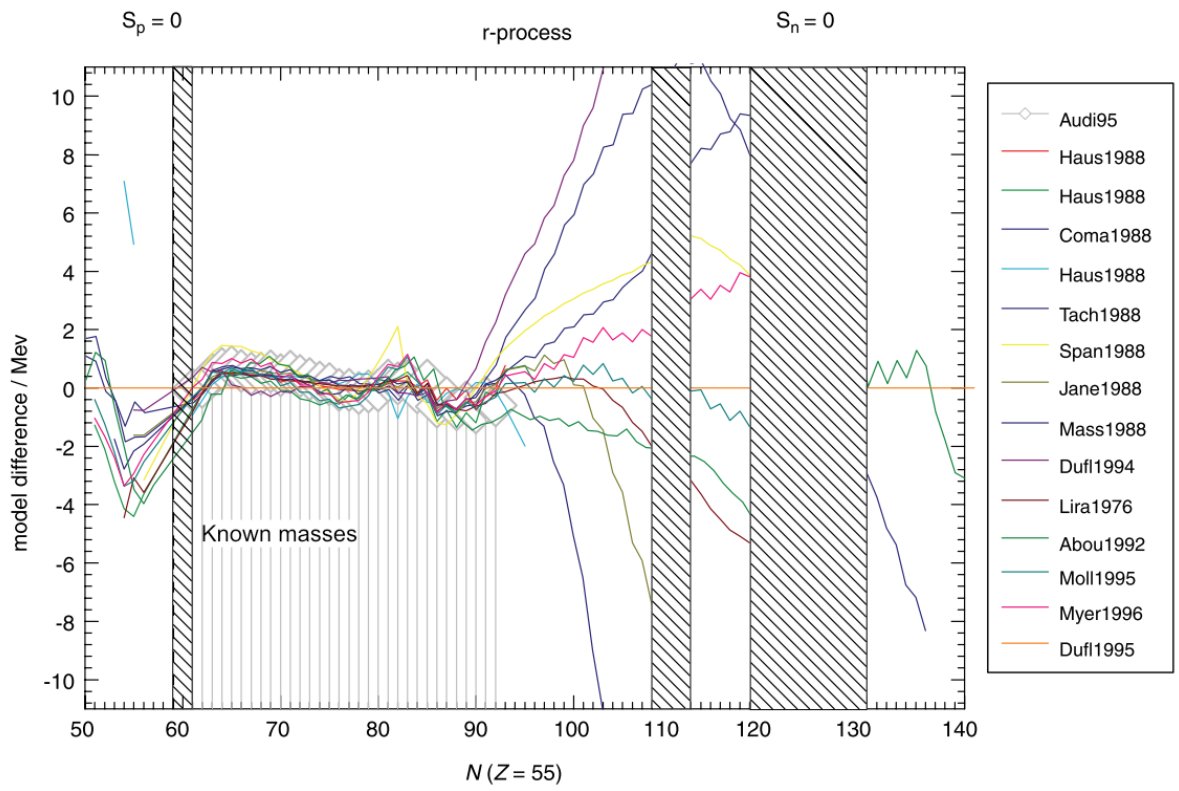

Figure 1.2.: Differences in the mass predictions of different theoretical models and experimental data as a function of the number of neutrons N for cesium isotopes (Z=55) relative to the Duflo-Zucker model (light orange line). S_p and S_n denote the regions, where the proton and neutron separation energy gets zero (so-called driplines). The differences in the predictions of masses by the theoretical models increase rapidly outside the region of known masses. Figure taken from Ref. [24].

While the waiting points at N=50 and N=82 are well investigated [25–27], current experimental data is still 15 neutrons away from the waiting point at N=126 [20]. Large effort goes into the design and construction of large-scale rare-isotope facilities like FRIB at the Michigan State University in the USA [28], RIBF at the RIKEN Nishina Center in Japan [29] or FAIR at GSI in Germany [30], aiming at producing experimental data in this region, which is of special interest, since it is the bottleneck for the production of actinides and additionally represents the last waiting point relatively close to the valley of stability.

The fission-fusion reaction scheme follows a different approach and exploits the unique features of laser-accelerated ion bunches. Fissile heavy ions are accelerated by a laser and then impinge on a second foil consisting of the same fissile material. With sufficient

energy of the accelerated ions, this leads to their fissioning. Subsequently, provided a high enough density, the neutron-rich, light fission fragments can fuse with each other, creating isotopes close to the waiting point at N=126. This reaction scheme relies on the solid-state-like density predicted for the laser-based ion acceleration via RPA, which cannot be achieved by conventional RF accelerators. Therefore, a prerequisite for this scheme is a good understanding and control of the laser-driven acceleration of heavy ions. As a primer, the acceleration of gold ions is investigated, as it is easier in the handling regarding radiation protection precautions compared to fissile ions.

While most efforts around the laser-based acceleration center around protons and lighter ions like carbon and oxygen ions, laser-based acceleration of heavy ions has received increasing interest over the recent years. In the work by Lindner *et al.* [31] a new record energy was set by the acceleration of gold ions above 7 MeV/u, reaching the energy necessary to overcome the typical fission barrier height for heavier ions of interest for the fission-fusion mechanism, e.g., thorium [32]. For this, the heating of the gold foils was investigated, aiming at suppressing the presence of surface contaminants on the target foils consisting of hydro-carbons and oxygen ions, otherwise potentially suppressing the efficient acceleration of gold ions. Furthermore, thanks to the exceptional resolution achieved in these experiments, realizing single charge-state resolution for gold ions up to energies of 4 MeV/u, simulations allowed to gain a deeper understanding of the ionization mechanism being present in the plasma created from the gold foils [33].

The goal of this thesis was to realize the acceleration of gold ions at the newly commissioned High Fields (HF) cave at the Centre for Advanced Laser Applications (CALA) in Garching, near Munich. Compared to the previous target heating and cleaning procedure [15], a more sophisticated setup was used in this thesis, allowing to determine the reached target temperatures depending on the output power of the dedicated continuous-wave (cw) laser used for heating. Furthermore, first steps towards the realization of reliable online detection of heavy ions accelerated by lasers were realized, necessary in order to take advantage of the nowadays accessible high repetition rates realized by state-of-the art, high-power laser systems. It is followed by a more in-depth analysis of surprisingly observed heavy ion signals with mass-to-charge ratios of $2 \leq m/q \leq 3$ not originating from gold ions.

Outline of this thesis

Chapter 2 introduces the theoretical background relevant for this thesis. It starts by describing the general interaction of ultra-intense laser pulses with matter before diving

into the details of laser-based acceleration of heavy ions. This is followed by a general overview of the interaction of accelerated, charged particles with matter. This is important to understand the underlying physics for online detectors, but also covers the principles of nuclear fission, laying the basis for the last chapter of this thesis. The chapter concludes by introducing the fission-fusion reaction scheme in greater detail.

In Chapter 3 the experimental infrastructure at CALA as well as the employed diagnostics are presented. First, the experimental facility at CALA, including its working horse, the ATLAS-3000 laser system, is covered, followed by the experimental setup in the HF vacuum chamber. Here the target fabrication as well as the heavy-ion Thomson parabola are discussed in greater detail. Finally, the charged particle detectors employed throughout this thesis are presented.

The impact of the target heating on the acceleration of heavy ions at CALA is discussed in Chapter 4. For this, first the principles of black-body radiation and Planck's law are introduced in order to explain the temperature measurements conducted in the course of this thesis using the heating setup, which is presented next. Following, the routine to calibrate the heating setup and the analysis for temperature retrieval are discussed, before the differential response to target heating observed during the experiments at CALA is portrayed.

Chapter 5 gives an overview of the first results investigating online detection of laser-plasma accelerated heavy ions. Two different setups were investigated, which are presented in separate sections.

This is followed in Chapter 6 by discussing the results of gold ion acceleration at HF. Besides presenting the reached charge-state distributions and cutoff energies, the unexpected observation of heavy ion signals in the mass-to-charge region of $2 \leq m/q \leq 3$ is discussed. The detailed analysis of the registered signal draws to the conclusion that they are fission fragments of gold generated inside the target and then get accelerated.

The potential processes leading to the induced fission of gold ions and hence creating the signals mentioned above are discussed in Chapter 7. It covers fission induced by neutrons, photons, electrons and positively charged particles.

The results of this thesis are discussed in Chapter 8, before giving a summary and outlook for future work in Chapter 9.

2. Theoretical Background

The experiments and results in this thesis rely on the focusing of an intense laser pulse on a target, whereby the target atoms are ionized and a plasma is created. Therefore, in the beginning of this chapter the interaction of an intense laser pulse with matter is introduced, covering the dominant ionization mechanisms as well as the absorption of the laser energy by the target electrons. This conversion of the laser pulse energy leads to the acceleration of ions, which is discussed next. In order to understand the experimental results achieved with these accelerated ions, the fundamentals of the interaction of charged particles with matter are presented, specifically the electronic stopping of accelerated particles in matter, fission of nuclei as well as the potential application of the laser-based acceleration of heavy elements, which is the fission-fusion reaction scheme.

2.1. Interaction of ultraintense laser pulses with matter

Short laser pulses start ionizing a target material when reaching intensities $I_L > 10^{12}\,\mathrm{W/cm^2}$ [34]. For large laser systems, this intensity level is already reached by light preceeding the main pulse, either in the coherent contrast region many picoseconds before the main pulse or by prepulses, situated in the intensity pedestal created by Amplified Spontaneous Emission (ASE) on a nanosecond time scale. The energy of an impinging photon can be absorbed by a bound electron. The energy of a photon is given via $E_{\mathrm{photon}} = \frac{h \cdot c}{\lambda_L} = \frac{h}{2\pi} \cdot \omega_L$, with the Planck constant h, the speed of light c, the laser wavelength λ_L and the laser angular frequency ω_L. For typical laser systems, this results in energies of a few electronvolts per photon (e.g. 1.55 eV for a Titanium-doped Sapphire (Ti:Sa) laser with a wavelength of $\lambda = 800\,\mathrm{nm}$). This is not sufficient to elevate the electron above the ionization threshold of the atom (e.g. $E_{\mathrm{atom}} = 13.6\,\mathrm{eV}$ for hydrogen atoms). The dominant ionization mechanisms are depicted in Fig. 2.1 and will be explained in detail in the following paragraphs.

Multiphoton ionization (MPI) If multiple photons deposit their energy in the same electron over a short period of time, the electron gains enough energy to be elevated above the atomic binding potential (see Fig. 2.1 left). The number of necessary photons

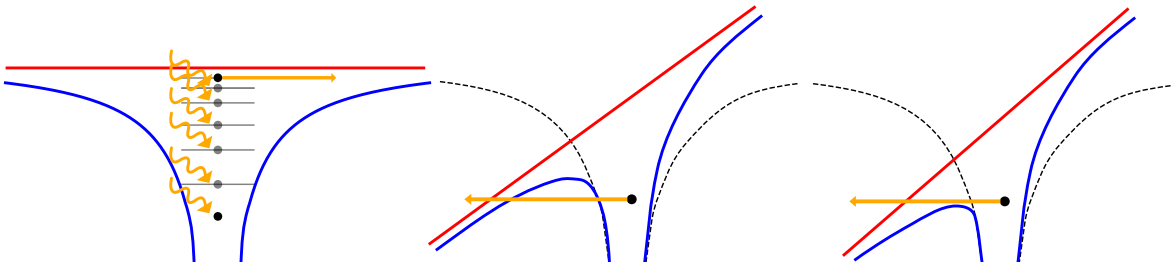

Figure 2.1.: The electron (black circle) is shown in the electric potential of the ion (blue), that was modified by an external field (potential plotted as red line), for three cases:
Left - For multiphoton ionization multiple photons (indicated in orange) elevate the electron above the atomic binding potential.
Middle - The initial binding potential of the ion (indicated by the black dotted line) was altered by the external laser field so that the ion can tunnel out of the potential.
Right - The binding potential is lowered so much by the laser that it is below the binding energy of the electron, leaving the latter unbound.

can be estimated to be $E_{\text{atom}}/E_{\text{photon}} \geq 9$. If the number of absorbed photons is larger than what is necessary to overcome the binding potential, the electron is left with a net energy gain, which is then termed *Above Threshold Ionization (ATI)*.

Field ionization For higher laser intensities the electric field of the pulse becomes strong enough to influence the binding potential, as illustrated by Fig. 2.1 in the middle. The electric laser field E_0 of the pulse is related to the laser pulse intensity by

$$I_L = \frac{\varepsilon_0 c}{2} \vec{E_0}^{\,2}, \tag{2.1}$$

with the vacuum permittivity ε_0 and the speed of light c. For *Tunnel Ionization (TI)* the potential is suppressed in a way that the quantum mechanical probability for the electron to tunnel through is high. This effect dominates for intensities $I_L \simeq 10^{14}\,\mathrm{W/cm^2}$. If the electric field of the laser pulse is even stronger, the potential can be lowered enough to be below the binding potential of the electron, leaving it unbound. This is referred to as *Barrier Suppression Ionization (BSI)*. Following Eq. (2.1) the intensity to ionize a hydrogen atom amounts to $3.5 \cdot 10^{16}\,\mathrm{W/cm^2}$, which is exceeded by typical values for lasers with ultra-high intensities with more than $10^{20}\,\mathrm{W/cm^2}$.

Collisional Ionization Once the electron is ionized from its bound state, it can further absorb energy from the laser pulse, as will be introduced in more detail later on. By

gaining additional energy and colliding with atoms, the free electron can transfer energy to bound electrons, contributing to further ionizations, which can lead to avalanche effects.

By the ionization of the target the latter changes its aggregate state into a plasma which is defined as a "quasineutral gas of charged and neutral particles which exhibits collective behaviour" [35]. Moving charged particles create currents, that will influence other charged particles and therefore induce collective behaviour. Further, when a charge is introdouced, the plasma particles rearrange and shield it, which is why it is termed "quasineutral". In general it is correct to assume that an external electromagnetic force will interact mostly with the electrons in the plasma, while the much heavier ions will form an immobile background, since the mass of the electron m_e is much smaller than the mass of the proton m_p by a factor $m_p/m_e \approx 1836$. Therefore, if an electron is displaced, this results in a local charge separation and the Coulomb force will act as a restoring force. When returning to its initial position, the electron will overshoot and start to oscillate. The frequency of this oscillation is called plasma frequency

$$\omega_p = \sqrt{\frac{n_e e^2}{\varepsilon_0 \gamma m_e}}, \tag{2.2}$$

including the elementary charge e, the electron mass m_e, the relativistic Lorentz factor $\gamma = \frac{1}{\sqrt{1-\frac{v^2}{c^2}}}$ with the electron's velocity v, and the electron density n_e as the only free parameter. The plasma frequency can be used to describe the refractive index of the plasma, η, for the incoming laser pulse with frequency ω_L by

$$\eta = \sqrt{1 - \frac{\omega_p^2}{\omega_L^2}}. \tag{2.3}$$

As a consequence, if $\omega_p < \sqrt{\gamma}\omega_L$, the refractive index stays real and the electrons cannot fully follow the motion of the electromagnetic wave, so that the laser can penetrate into the target. Conversely, for $\omega_p > \sqrt{\gamma}\omega_L$, the refractive index becomes complex and most part of the laser is reflected while only an exponentially decaying, evanescent wave penetrates into the target and can transfer energy. As a consequence of Eq. (2.3), the refractive index is depending on γ and the plasma density n_e. Therefore, spatial variation of these two factors leads to a spatially varying refractive index, which can lead to self-focusing of the laser.

The turning point for $\omega_p = \omega_L$ is defined as the critical density $n_c = \frac{m_e \varepsilon_0 \omega_L^2}{e^2}$ (with the

relativistic critical density defined via $n_{c,\text{rel.}} = \gamma n_c$). With this, Eq. (2.3) can be rewritten as $\eta = \sqrt{1 - \frac{n_e}{\gamma n_c}}$. For $n_e > n_c$ the plasma is called overdense, while $n_e < n_c$ is referred to as an underdense plasma. For an overdense plasma, the plasma skin depth l_s describes the distance at which the amplitude of the evanescent wave of the laser penetrating into the plasma has dropped to $1/e$:

$$l_s = \frac{c}{\sqrt{\omega_p^2 - \omega_L^2}}. \tag{2.4}$$

The normalized vector potential a_0 describes the transition where the laser field becomes strong enough so that the mass of the oscillating electron has to be treated relativistically via

$$a_0 = \frac{eE_0}{\omega_L m_e c} = 0.85 \cdot \sqrt{\frac{I_L[\mathrm{W\,cm^{-2}}]\lambda_L^2[\mu\mathrm{m}^2]}{10^{18}}}. \tag{2.5}$$

If $a_0 \geq 1$, the electron motion in the laser field is considered relativistic. In the case of a Ti:Sa laser system with $\lambda_L = 800\,\mathrm{nm}$, this is satisfied for intensities exceeding $I_L \simeq 2 \cdot 10^{18}\,\mathrm{W\,cm^{-2}}$. If the electron velocities become relativistic, this results in an increase of the electron mass. This in turn means that the plasma frequency is decreased. For very large mass increase of the electron (very high γ factor) this can make the plasma frequency drop below the frequency of the laser, turning the previously opaque plasma transparent to the laser, called relativistically induced transparency.

The movement of a charged particle in the presence of an electromagnetic field with its electric and magnetic field component, $\vec{E}$ and $\vec{B}$ respectively, can be described by the Lorentz force $\vec{F}_L$

$$\vec{F}_L = q\left(\vec{E} + \vec{v} \times \vec{B}\right), \tag{2.6}$$

with the charge q and the particle's velocity $\vec{v}$.

For nonrelativistic velocities of the electron, the $\vec{v} \times \vec{B}$ term is negligible and, therefore, its movement in the plasma oscillating due to the laser field can be described via a planar wave:

$$\vec{x} = \frac{e\vec{E}_0}{m_e \omega_L^2} \cos(\omega_L t + \varphi) + \vec{v}_0 t + \vec{x}_0, \tag{2.7}$$

for a point in time, t, with a random phase φ, the initial electron velocity $\vec{v}_0$ and the initial electron position $\vec{x}_0$. This results in a maximum oscillatory velocity v_{osc} and hence

maximum energy ε_{osc} of

$$v_{\text{osc}} = \frac{e|\vec{E}|}{m_e \omega_L}, \tag{2.8}$$

$$\varepsilon_{\text{osc}} = \frac{e^2 \vec{E}_0^2}{2 m_e \omega_L^2}. \tag{2.9}$$

To achieve the high intensities required for experiments, the laser is tightly focused in space and compressed in time. This leads to strong variations of the electromagnetic field strength. As a result, electrons can be accelerated from a region of high intensity in the first half cycle of the oscillating laser field into regions of lower intensity, therefore experiencing a weaker restoring force. This results in a quiver motion of the electrons and a net energy gain, pushing them out of areas with high intensity. The resulting force is called ponderomotive force and is described via

$$\vec{F}_p = \frac{e^2}{2 m_e \omega_L^2} \nabla \langle \vec{E}_0^2 \rangle. \tag{2.10}$$

As previously mentioned, once the electrons are ionized from the atomic potential, they can absorb energy from the laser pulse. Several absorption mechanisms are possible and the specifics of the energy conversion depend on target and laser parameters. Since this is a highly nonlinear process, small variations in any parameter can have a large influence on the absorption, with in practice typically several parameters changing at once. The region in which the laser can transfer energy to the electrons is restricted to the underdense plasma up to the skin depth (see Eq. (2.4)). The here discussed absorption processes only include a selection. More detailed information can be found in the literature [12, 36]. We will now discuss the interaction of the laser pulse with a target for which $n_e \gg n_c$.

The initial absorption of laser energy in the plasma starts with *inverse Bremsstrahlung*, for which the plasma density needs to be not yet too much decreased and therefore collisions in the plasma are still likely. When the electron gets accelerated by the laser field and collides with an ion, it can transfer its energy to the ion. This leads to an energy transfer from the laser to the ions. For an obliquely incident, p-polarized laser pulse, the electron oscillations induced by the laser lead to density fluctuations in the density gradient. At $n_e = n_c$, the electron oscillations are in resonance with the laser frequency and drive a plasma wave, coupling the laser energy into the plasma. Therefore, this is called *resonance absorption*. The resonant wave will subsequently transfer energy

into the cold plasma.

For *vacuum heating* or *Brunel heating* the density gradient between vacuum and plasma needs to be very steep. Electrons at the target surface get pulled out by the laser and accelerated into the vacuum. During the next cycle of the laser, they reenter the plasma. Since at the surface it holds that $n_e > n_c$, the laser cannot enter the target and the electrons are accelerated into the target with a net energy gain, depositing their energy.

Once the laser intensity is high enough so that $a_0 \geq 1$, the $\vec{v} \times \vec{B}$ term of the Lorentz force (c.f. Eq. (2.6)) is not negligible anymore, resulting in the so-called $j \times B$ *heating*. For normal incidence laser pulses with linear polarization it leads to a longitudinal movement of electrons along the laser propagation axis, if the density gradient is steep. Since the laser cannot penetrate into the target, the electrons are left with a net energy gain, transferring their energy to the plasma. This process is suppressed for circularly polarized light.

From these explanations it becomes apparent that the energy distribution of the electrons gaining energy from the laser-plasma interaction is crucial for the further understanding of the acceleration mechanism and attempts have been made to describe their distribution by assigning a hot electron temperature. Since the $j \times B$ heating is usually the dominating heating mechanism, Wilks *et al.* derived an electron temperature from the ponderomotive force, which can be rewritten using the normalized vector potential a_0 of the laser field as

$$T_{\mathrm{e,h}} = m_e c^2 \left(\sqrt{1 + \kappa a_0^2} - 1 \right), \tag{2.11}$$

with $\kappa = 0.5$ for linearly polarized light and $\kappa = 1$ for circular polarization [36, 37]. Circular polarization thus yields a higher effective hot-electron temperature for the same intensity and wavelength. It was further shown that the electron distribution has a hotter tail with temperatures above the ponderomotive scaling from the acceleration of electrons from regions below the critical density [38, 39].

When these electrons are decelerated in the Coulomb field of a nucleus in the target, γ rays are emitted via bremsstrahlung. The spectral distribution of these γ rays is directly related to the energy distribution of the hot electrons. A typical way to measure the bremsstrahlung spectrum is via nuclear activation measurements. In $(\gamma, x\mathrm{n})$ reactions, the γ rays excite high-Z target nuclei in which then deexcite via neutron evaporation, turning the initially stable target radioactive. The number of neutrons x that are emitted per nucleus increases with the maximum energy of the bremsstrahlung [40]. Via γ spectroscopy the activation of the detector can be measured. Such measurements have

provided clear evidence of a two-slope behavior of the bremsstrahlung spectrum, for example reported by Stoyer *et al.* [41], a consequence of the separate behavior of a hot and a cold electron distribution.

To gain a better understanding of the processes in the plasma, time resolved probing is be desirable. This is, however, difficult to achieve since any given light source can only penetrate through a medium that is underdense relative to its one wavelength (see Eq. (2.3)). In order to probe the full evolution, starting from a solid target, light sources like free-electron lasers, emitting light in the X ray regime are needed. Since free-electron lasers are large setups themselves, often times simulations are used to get a deeper understanding [36]. For plasmas that exhibit local thermal equilibria, fluid models are often times employed. On the contrary for plasmas, that are strongly fluctuating and not in equilibrium, so-called Particle-In-Cell (PIC) codes are used. Here space is discretized by a grid, that the particles are placed upon. To facilitate the handling of the large amount of particles, they are summarized by so-called macro particles. A simulation then consists of four steps. First the position and velocities of the macro particles are used to calculate mass and current densities for each cell. Then the Maxwell equations are solved to determine the magnetic and electric field strength in every cell. In a next step, the fields are translated into forces acting on every macro particle. Finally, the particles are pushed to their new position and velocities in the next time step, before the process is repeated. PIC simulations are commonly used to model the processes described in the next section.

2.2. Laser-based acceleration of heavy ions

With currently achievable maximum laser intensities of $10^{23}\,\mathrm{W/cm^2}$ [3], direct acceleration of protons or ions is not achievable. This can be easily derived when considering the a_0 necessary for the much heavier protons compared to the electrons ($m_p/m_e \approx 1836$). Solving Eq. (2.5) for the intensity, using $\lambda_L = 0.8\,\mu\mathrm{m}$, this yields $I_L \approx 6 \cdot 10^{24}\,\mathrm{W/cm^2}$.

In today's experiments, the ions are rather accelerated indirectly, with the laser transferring its energy to the target electrons, which then create large charge separation fields which then in turn accelerate the ions. The maximum ion energy will depend on how efficiently the laser energy is converted to the electrons. As outlined in the previous section, this process will vary depending on the laser parameters, such as the temporal evolution of the laser pulse, the so-called temporal contrast, pulse length and energy, as well as target properties, such as thickness and electron density, variable, e.g., by

choice of material. Often times a mixture of different regimes is observed in experiments. The two acceleration regimes relevant for the scope of this thesis are Target Normal Sheath Acceleration (TNSA) and Radiation Pressure Acceleration (RPA), which will be introduced in the following. Their main difference can be summarized in their incoherent / coherent response of plasma electrons to the laser pulse. A more detailed review can be found in Ref. [12, 13].

2.2.1. Target Normal Sheath Acceleration

Target normal sheath acceleration (TNSA) relies on the incoherent heating of plasma electrons by the laser pulse and is the most studied and so far most robust regime for laser-based ion acceleration. It requires high laser peak intensities $\sim 10^{18-20}\,\mathrm{W\,cm^{-2}}$ and good temporal contrast ($\sim 10^{-10}$) with target thicknesses in the order of the laser wavelength or much thicker, up so several micrometers. The first experimental observations of TNSA were reported by Snavely *et al.* [10], Clark *et al.* [11] as well as Maksimchuk *et al.* [42], with first theoretical explanations provided by Wilks *et al.* [39].

As previously laid out, light preceding the main pulse ionizes the target, accelerating electrons from the front side, depositing their energy within the target. If they have sufficient energy, they travel trough the target bulk, exiting the target on the rear side into vacuum. With more and more electrons escaping the target, a large quasi-static field is created, with the Coulomb force attracting the electrons back into the target. While the most energetic electrons are able to overcome this force and leave into vacuum, the lower energetic electrons reenter the target and start to circulate (see e.g. Ref. [43]). The electrons start to effectively accumulate at the target rear, creating a sheath extending into the vacuum over a distance of

$$\lambda_D = \sqrt{\frac{\varepsilon_0 k_b T_{\mathrm{e,h}}}{n_e e^2}}, \tag{2.12}$$

also called Debye sheath, creating a quasi-static field with strengths of TV/m. It is oriented normal to the target surface, hence the name of target normal acceleration.

This field can further ionize atoms from the bulk and accelerate them. In contrast to conventional accelerators, multiple species with multiple charge states are accelerated, exhibiting an exponentially decaying energy spectrum with a characteristic cutoff energy. This implies that ions with the lowest mass-to-charge ratio, i.e. protons which are always present in the form of surface contaminants, are most efficiently accelerated. Ways to suppress the acceleration of protons and consequently enhance the acceleration of heavier

ions will be discussed in Chap. 4.

While it is well known that the maximum ion energy $\varepsilon_{\mathrm{i,max}}$ scales with T_e, the prediction of the exact coefficient between both values differs between models. This is because the interaction depends on quantities which can either be measured only with a limited precision or are hard to be accessed at all. The analytical model by Mora assumes an isothermal, collisionless expansion of a quasi-neutral plasma as a fluid [44]. It was later on found by Fuchs *et al.* by applying an empirical value of $t = 1.3 \cdot \tau_L$ for the plasma expansion time, with τ_L being the laser pulse length, that the model by Mora fits their experimental data [45]. The model developed by Schreiber *et al.* uses a non-relativistic, quasi-static model, providing an analytical solution in 1D [46]. It only uses the target thickness, the laser pulse energy E_L and pulse length τ_L as input parameters.

2.2.2. Radiation Pressure Acceleration

In contrast to TNSA, radiation pressure acceleration (RPA) relies on the coherent response of the target to the laser field. This mechanism depends on the transfer of momentum from photons to electrons, an idea first proposed by Veksler *et al.* [9]. The acceleration of plasma electrons, leaving the heavier ions behind, creates a charge separation, building up strong electrostatic fields that subsequently lead to acceleration of the ions. RPA requires very high temporal contrast of the laser pulse ($<10^{-12}$), laser intensities exceeding $10^{23}\,\mathrm{W/cm^2}$ (the laser intensity where it becomes dominant compared to TNSA), with target thicknesses below the laser wavelength down to a few tens of nanometers, producing beams with a quasi-monoenergetic spectrum and small divergence, with close-to-solid target density ($\approx 10^{21}\,\mathrm{cm^{-3}}$) [47, 48]. The two most discussed regimes are Hole Boring (HB) and Light Sail (LS) mode, which will be presented in the following, leaving out closely related schemes like ion acceleration via relativistic transparency [49, 50], collisionless shock acceleration [51], break out afterburner [52] or hybrid acceleration schemes [53].

The *hole boring* mode occurs for targets thick enough, so that the laser pulse cannot interact with the target rear side, i.e. $l_s < d$ with d being the target thickness. The radiation pressure of the laser pulse pushes the surface of an overdense plasma inward, thereby steepening the density profile. The parabolic deformation of the plasma surface enables a deep penetration of the laser into the target. Hence the name 'hole boring'. A compressed layer of electrons is pushed into the foil and by this accelerating highly collimated ions up to high energies. This can be sustained until either the laser pulse ends or the hole boring reaches the target rear side.

For thinner targets the laser pulse breaks through, accelerating the entire target volume in the so called *light sail* regime. As long as the target stays above the critical density, i.e. $n_e > n_c$, the laser will push against it and be reflected. Due to the momentum transfer, the reflected light is redshifted. In this regime, the ions closely follow the electrons, rapidly reaching relativistic energies. The light sail mode therefore delivers the highest ion energies for the thinnest targets with the lowest possible plasma density and the highest laser intensity, offering superior scaling of maximum ion energy compared to TNSA and HB.

2.3. Interaction of accelerated, charged particles with matter

To properly interpret the experimental results with accelerated charged particle, understanding their interaction with matter is crucial. Furthermore, it explains the underlying physics of radiation detectors. When energetic ions travel through matter, they will undergo elastic and inelastic collisions with the target material. Inelastic collisions as well as radiation losses are responsible for the loss of energy of the incident particle. Since radiation losses are not important for the energy ranges covered in this work, they will not be further discussed.

When energetic ions travel through matter, they interact with both the atomic nuclei and the electron cloud of the target atoms. The stopping power S of a material gives information about the differential energy loss $\mathrm{d}E$ over a distance $\mathrm{d}x$

$$S = -\frac{\mathrm{d}E}{\mathrm{d}x} = -\left(\left(\frac{\mathrm{d}E}{\mathrm{d}x}\right)_{\mathrm{el}} + \left(\frac{\mathrm{d}E}{\mathrm{d}x}\right)_{\mathrm{nucl.}}\right), \tag{2.13}$$

including both, electric (relevant for $E > 100\,\mathrm{keV/u}$) and nuclear stopping (dominant only for $E < 1\,\mathrm{keV/u}$). First, the electronic stopping will be introduced followed by a discussion of one potential consequence of nuclear stopping, which is nuclear fission. This chapter will be closed with an introduction to the fission-fusion reaction scheme.

2.3.1. Electronic stopping

The electronic stopping power arises from inelastic interaction of the incident particle with the bound electrons of the target atoms. A quantitative description including quantum mechanical and relativistic effects is given by the Bethe-Bloch formula, derived

from first-order perturbation theory [54]. The Particle Data Group, an international collaboration, present the Bethe-Bloch equation in their Book on Review of Particle Physics in the following form [55]

$$\left\langle -\frac{\mathrm{d}E}{\mathrm{d}x} \right\rangle = Kz^2 \frac{Z}{A} \frac{1}{\beta^2} \left[\frac{1}{2} \ln \frac{2m_e c^2 \beta^2 \gamma^2 W_{\max}}{I^2} - \beta^2 - \frac{\delta(\beta\gamma)}{2}. \right] \tag{2.14}$$

K summarizes the constants via $K = 4\pi N_A r_e^2 m_e c^2$, with the classical electron radius r_e and Avogadro's number N_A. $W_{\max}$ is the maximum energy transfer to an electron in a single collision for a point-like particle with mass $M \gg m_e$ defined via $W_{\max} = \frac{2m_e c^2 \beta^2 \gamma^2}{1+2\gamma m_e/M+(m_e/M)^2}$. Other constants are the charge of the incident particle z, the charge the medium the particle impinges on Z, the atomic mass of the medium A and the mean ionization potential of the medium I. δ is a density correction for the transversal extension of the electrical field, relevant for relativistic corrections. This formula is valid for particles with masses larger than the muon mass $M > m_\mu$ and velocities in the range of $0.05 < \beta\gamma < 500$. If the projectile is too slow, charge exchange or electron capture become important, reducing the stopping power by screening the nuclear charge and thus reducing its effective charge. The corrections for low energetic projectiles is covered by the LSS theory, established by Lindhard, Scharff and Schiøtt [56].

The Bethe-Bloch formula is based on the assumptions that the projectile is sufficiently fast such that first-order perturbation treatment is valid, so that the interaction of projectile and target electrons can be treated as binary collisions. For the very high particle densities, this may not be the case. To account for this, according to Ichimaru [57], the Bethe-Bloch formula can be decomposed into a first part relying on binary collisions and a second part accounting for long-range collective contributions:

$$\left\langle -\frac{\mathrm{d}E}{\mathrm{d}x} \right\rangle = Kz^2 \frac{Z}{A} \frac{1}{\beta^2} \left[\ln \left(m_e v^2 / e^2 k_D \right) + \ln(k_D v/\omega_p) \right], \tag{2.15}$$

using the Debye wavenumber $k_D = 1/\lambda_D$, analogous to Eq. (2.12). While for the stopping of intense ion bunches in a plasma enhanced stopping due to collective effects is discussed (compare Ref. [58]), Habs *et al.* discuss the possibility of reduced stopping power for cases where the plasma wavelength is much smaller than the ion bunch length, i.e. for stopping in solids [16]. Both effects have so far not been observed experimentally.

The logarithmic term in both equations reflects the fact that the stopping power increases as the projectile velocity decreases. It reaches a maximum when the velocity of the projectile is comparable to the velocity of the bound electrons, where Coulomb

interaction between both is maximized. As a consequence, most of the projectile's energy is deposited in a short range, also called Bragg peak.

A widely used software package to simulate the energy loss is the Stopping Range of Ions in Matter (SRIM), developed by James F. Ziegler and Jochen P. Biersack in 1985 for ions with energies between 10 eV to 2 GeV. While SRIM allows a quick calculation of stopping and range tables, another subpackage allows to simulate the TRansport of Ions in Matter (TRIM). The program is based on a binary collision approximation, using a Monte-Carlo method [59].

2.3.2. Nuclear fission

The total mass of a nucleus M_{nucl} is different of the mass of all its constituents when separated from each other:

$$M_{\text{nucl}} = ZM_p + (A - Z)M_n - \Delta, \tag{2.16}$$

where M_p is the mass of a proton, Z is the number of protons, A is the total number of nucleons, M_n is the mass of a neutron and Δ denotes the mass defect. This mass defect Δ can be used to describe the binding energy B of the nucleus

$$B = c^2\Delta, \tag{2.17}$$

following Einstein's mass-energy relation $E = mc^2$. The total binding energy can be interpreted as the work necessary to dissolve the nucleus into its constituents. For elements heavier than iron ($A \approx 56$) the binding energy decreases with increasing number of nucleons. This is a consequence of the repelling electrostatic force between the protons. For short distances it is weak compared to the nuclear binding forces. However, for high Z it becomes more important and decreases the binding force [60].

Large parts of nuclear physics arise from the fact that this bound ensemble of nucleons forming the nucleus is subject to instabilities. Blatt and Weisskopf distinguish two forms of instabilities [60]:

1. *dynamic* instability, which leads to the spontaneous break up of nuclei, as it is the case, e.g., for alpha decays and fission

2. *beta* instability, where the charge in the nucleus is spontaneously changed by one unit, accompanied by the emission or absorption of an electron, e.g. for beta-decay or electron capture

The liquid drop model offers a macroscopic picture of the nucleus, treating it as a drop of incompressible nuclear fluid. In this analogy, the individual nuclei interact strongly with their nearest neighbor, creating surface tension similar to a liquid drop. This further takes into account, that the binding energy for nucleons on the surface have a lower binding energy since they have fewer immediate neighbors. Counteracting is the Coulomb repulsion between the positively charged protons. External influences can distort the liquid drop. For it to remain stable against small distortions, the decrease in the Coulomb energy E_C must be smaller than the increase in surface energy E_S. From this, Bohr and Wheeler [61] defined the fissility parameter x according to

$$x = \frac{E_C}{2E_S}. \tag{2.18}$$

For $x < 1$ the drop will be stable against small distortions, while for $x > 1$ spontaneous division of the drop is possible, as there is no potential barrier inhibiting it. Therefore, the closer x comes to unity, the lower is the fission barrier. Further analysis by Green [62] allowed to deduce from this $x \propto Z^2/A$, a relation often times used when describing fission. The liquid drop model is a macroscopic model that is good in describing general trends and accounts for the existence of fission and fusion, as will be discussed later on, giving insights into nuclear stability. However, it cannot explain fine details of nuclear structure such as magic numbers, for which the nuclear shell model is needed.

If energy is transferred to the nucleus by an external source, fission is one of the deexcitation channels that can be triggered. This led Bohr and Wheeler to introduce the theory of induced fission. Using the liquid drop model, an external source acting on a nucleus can be described as initiating a deformation of the drop which then starts to vibrate. For this, it is convenient to describe the shape of the drop using an expansion in Legendre polynomials

$$R(\Theta) = (R_0/\lambda)\left[1 + \sum_{n=1} \alpha_n P_n(\cos\Theta)\right], \tag{2.19}$$

where λ is a scale factor to ensure that the value remains constant at the volume for a sphere of radius R_0. The two leading terms α_2 and α_4 are almost an order of magnitude larger than higher terms and therefore describe the two most relevant vibrational modes. The energy of the external source defines the amount of deformation of the drop. For small deformations, the surface tension is strong enough to counteract fission of the drop up to the saddle point, which marks the turning point and defines the fission barrier.

Once the nucleus overcomes the saddle point, fission will occur. The drop elongates further until it splits at the so-called scission point.

Neutron evaporation is the most important other competing process [61]. The balance between the two depends on several factors, including the fission barrier height, neutron binding energy, excitation energy, angular momentum, and the level density parameter of both [63].

One way to induce fission is via neutrons. Since neutrons are electrically uncharged, they are not repelled by the Coulomb barrier. Therefore, for some nuclei neutron-induced fission is possible by thermal neutrons as well as by fast ones. The first experiment was conducted by Hahn and Strassmann, bombarding uranium with slow neutrons, yielding barium [64, 65]. Their experimental findings were interpreted by Meitner and Frisch, introducing the term of nuclear fission [66, 67].

The first successful experiment using γ rays to induce fission was conducted in 1940 [68, 69], a process also termed photo-fission. The maximum of the photo-fission cross section is related to the excitation of the Giant Dipole Resonance (GDR) in the nucleus [70]. Its excitation energy E_{GDR} is given via $E_{\mathrm{GDR}} \approx 79 \cdot A^{-1/3}$ [71].

For protons, deuterons and heavier ions to form a compound nucleus with a target, additional energy is necessary to overcome the Coulomb barrier. The height of this barrier is empirically described by the Bass barrier using the nuclear charges of the projectile and the target Z_1 and Z_2, the nuclear radii of both, summarized via $R_{12} = R_1 + R_2 = r_0 \left(A_1^{1/3} + A_2^{1/3}\right)$, with the total number of nucleons of the projectile and the target A_1 and A_2 [72].

While the mass distribution of fission fragments from actinides exhibits a double-humped distribution of light and heavy fragments, the fragments from lighter nuclei with $Z \leq 84$ fission symmetrically at all excitation energies. The width of the distribution increases with the excitation energy. Once the fragments are separated, they are further accelerated as a result of the large Coulomb repulsion [63].

Besides compound nucleus fission, which proceeds through full equilibration of the system, fission-like processes can also occur in more peripheral nuclear collisions, commonly referred to as quasi-fission. In such grazing interactions the projectile and target nuclei only partially overlap, leading to nucleon and angular momentum exchange without the formation of a fully equilibrated compound nucleus. If sufficient excitation energy is deposited, the system can split into two heavy fragments resembling fission, but with broader, often asymmetric fragment mass distributions, strong angular anisotropies, and neutron emission patterns distinct from compound nucleus fission. Quasi-fission becomes

increasingly important for very heavy systems, where the large Coulomb repulsion disfavors fusion and instead drives re-separation near the Bass barrier, making it a key limitation in the synthesis of super-heavy elements [73–75].

2.3.3. Fission-fusion reaction scheme

The rapid neutron capture process (r-process) is known to be responsible for the cosmic nucleosynthesis of heavy elements beyond iron like gold, uranium and thorium. While the waiting points at N=50 and N=82 are well investigated [24–27], up to date there are no experimental data for the waiting point at N=126, which is of special interest since it poses a bottleneck for the creation of actinides and beyond. The fission-fusion reaction scheme proposed by Habs *et al.* [16] relies on the acceleration of ultra-high density ion bunches of fissile isotopes via HB RPA from a first target (so-called production target). Fission of beam and target nuclei in a second target (reaction target) will then open up the possibility of fusion of neutron-rich light fission fragments, hereby generating extremely neutron-rich ion species, enabling the investigation of nuclear properties around the waiting point at N=126.

The schematic setup of the fission-fusion reaction scheme is depicted in Fig. 2.2, adapted from the original proposal by Habs et al. [16]. Ions are accelerated by a high intensity laser pulse from a first production target, consisting of a fissile material (here for practical simplicity chosen as ^{232}Th), sandwiched with a deuterated plastic layer. ^{232}Th is chosen because of its long half-life and stability in vacuum conditions necessary for laser-based acceleration, i.e. at 10^{-7} to 10^{-5} mbar. The spectrum of accelerated ions therefore consists of thorium and carbon ions as well as of deuterons and protons. They then impinge on the reaction target, which is placed at a distance of 0.1 to 1 mm and is made out of a layer of polyethylene followed by a layer of the same fissile species, here ^{232}Th.

The thorium ions, accelerated to and above their fission barrier at about 7 MeV/u, will undergo fission when impinging on the CH_2 layer of the reaction target, while, in addition, the light ions accelerated from the production target to energies above 7 MeV/u, will penetrate through the CH_2 layer, inducing fission of thorium in the following layer of the reaction target. The fission of ^{232}Th proceeds asymmetric [63], with the heavy fragments centered around $A_H = 139.5$ and the light fragments around $A_L = 91$ with $Z_L \approx 37.5$. The fission-fusion reaction scheme then relies on the fusion of two light, neutron-rich fission products which in turn requires the nearly solid-state-like density of the incident ion bunch enabled by the acceleration via the high-intensity laser pulse.

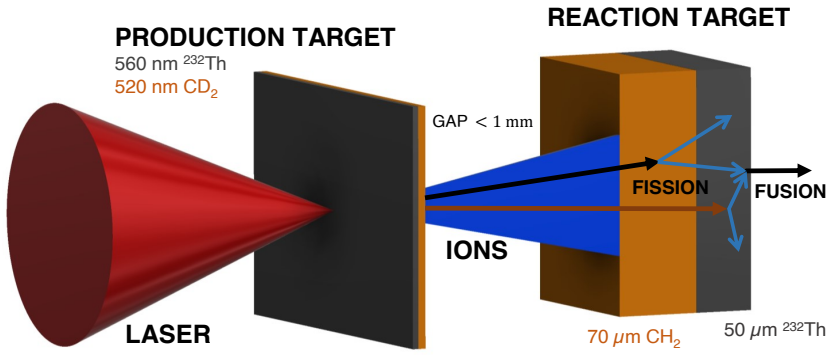

Figure 2.2.: For the fission-fusion reaction scheme, a high-intensity laser beam is focused on a first production target, which consists of a layer of ^{232}Th and deuterated carbon. By the interaction of the laser pulse with the target, thorium ions as well as carbon ions and deuterons are accelerated onto a second target, the so-called reaction target. This target is made out of a layer of polyethylene and ^{232}Th. In this target, fission of the thorium ions can occur. Fusion of two light thorium fission products creates a neutron rich nucleus and therefore to the realization of the fission-fusion reaction scheme. Image taken from Ref. [76].

Hereby a compound nucleus close to the waiting point at N=126 is created, i.e. with a central value of $A_F \approx 182$ and $Z_F \approx 75$. According to PACE4 [77, 78] calculations, which is part of the LISE++ framework [79], the best energy range for fusion reactions resulting in neutron-rich products is around 2.8 MeV/u. Hence, the thickness of each layer in the reaction target is chosen such that the fission fragments are decelerated to an energy range of 2 to 3 MeV/u, in order to maximize the fusion yield. Assuming normal stopping according to the Bethe-Bloch equation (c.f. Eq. (2.14)), the authors calculate 1-2 fusion products being possible per laser shot. This value can be further enhanced to up to $4 \cdot 10^4$ products per shot, if collective effects alter the stopping power in the production target by an assumed factor of 100. Such collective modification of the electronic stopping behavior can be expected from the interaction of the ultra-dense accelerated ion bunch when interacting with the atomic electrons of the absorbing target layer. As counteracting plasma instabilities (e.g. Rayleigh-Taylor, Weibel [35]) may interfere in this phase, experimental verification and quantification of such collective effects is of high interest and subject of ongoing experimental studies [80].

After extraction of the fusion products from the target and separation from other species, this will allow for an investigation of the nuclear properties close to the waiting point at N=126.

In the next chapter, the experimental infrastructure used in the course of this thesis is presented.

3. Experimental infrastructure and diagnostics

This chapter introduces the experimental infrastructure used in this thesis as well as the specifics of the used diagnostics. The experiments were conducted at the Centre for Advanced Laser Applications (CALA) in Garching using the ATLAS-3000, a laser with ultrahigh intensity, introduced in the beginning of this chapter. The laser pulse was then directed into the vacuum chamber of the High Field (HF) cave. After introducing the general setup in the HF cave the Thomson parabola spectrometer (TPS) and the charged particle detectors employed in this thesis will be presented.

3.1. ATLAS-3000 laser at the Centre for Advanced Laser Applications (CALA)

Research at CALA, a research facility based in Garching near Munich, is centered around the development and use of laser-driven particle and X-ray sources and houses several lasers. The working horse is the ATLAS-3000, a laser system based on Chirped Pulse Amplification (CPA) [1], where the original pulse is stretched in time, amplified and finally compressed again. The ATLAS-3000 system is based on Titanium doped Sapphire (Ti:Sa) as a gain medium. The pulse originates from a commercial oscillator starting in air, is stretched in a grating stretcher, and then amplified in a series of home built and commercial amplifiers. After the final energy gain in the two main amplifiers, the beam transitions into vacuum and is magnified to about 28 cm diameter, before being compressed in time by a grating-based compressor. After compression, the beam can be either delivered to a diagnostic bench or towards the experimental areas.

The laser energy is mostly adjusted by changing the number of pump lasers used in the main amplification stage, can be varied from a few Joules up to 90 J before compression (equivalent to several hundred Terawatt up to more than two Petawatt after compression) and operates at 1 Hz repetition rate. For diagnostic purposes a reflective attenuator reduces the beam energy by five orders of magnitude. In combination with four additional

filters it allows to image the laser pulse with cameras, without damaging the sensors, capturing a large dynamic range. The term *full power shot* in this thesis refers to shots with the attenuator moved out of the beam path. Other laser parameters like the pulse length, typically around 28 fs, and the temporal contrast, i.e. the temporal evolution of the laser pulse, slightly vary from day-to-day and are measured with a suite of diagnostics on the diagnostic bench prior to every experiment. Detailed information about the laser system can be found in reference [81].

After characterization of the laser pulse, it can be directed to the desired experiment by switching a mirror and hereby changing the laser path from the diagnostic table to the Laser Beamline Delivery (LBD). The LBD consists of a set of mirrors, directing the beam into one of the four active experimental areas, so-called caves. The four caves house experimental setups for the investigation of laser-electron acceleration at the Electron and Thomson Test Facility (ETTF), photon-photon scattering at the Laser-based Universal eXperimentation beamline (LUX) as well as ion acceleration at the Laser-driven Ion Acceleration(LION) and High Field Physics (HF) experimental areas. The destination of the laser pulse can easily be changed on a day-to-day basis. The infrastructure at CALA, including more thorough details about the LBD and safety precautions are described in reference [82].

For the experiments conducted in the scope of this thesis, the laser pulse was guided towards the HF cave. One of the mirrors on this path is a deformable mirror, which is used to optimize the pulse's wavefront and hence improve the focus quality, i.e. the reachable peak intensity. It works in a closed feedback loop with a wavefront sensor detailed in Sec. 3.2. More information about the system can be found in reference [83]. The control system at CALA is based on Tango Controls, an open source software developed by a consortium of research institutes. It is used to control and monitor devices such as motors as well as to log experimental data during experiments [84].

3.2. Experimental setup in the High Fields (HF) cave

The setup in the HF cave is intended for preparatory studies en-route to the realization of the fission-fusion reaction scheme. While the aim of this thesis includes a better understanding of the acceleration of heavy ions using high-intensity lasers, other projects include the study of fission, namely of uranium, by light and heavy particles accelerated by the laser and the investigation of collective effects. The setup used in the scope of this thesis is depicted in Fig. 3.1.

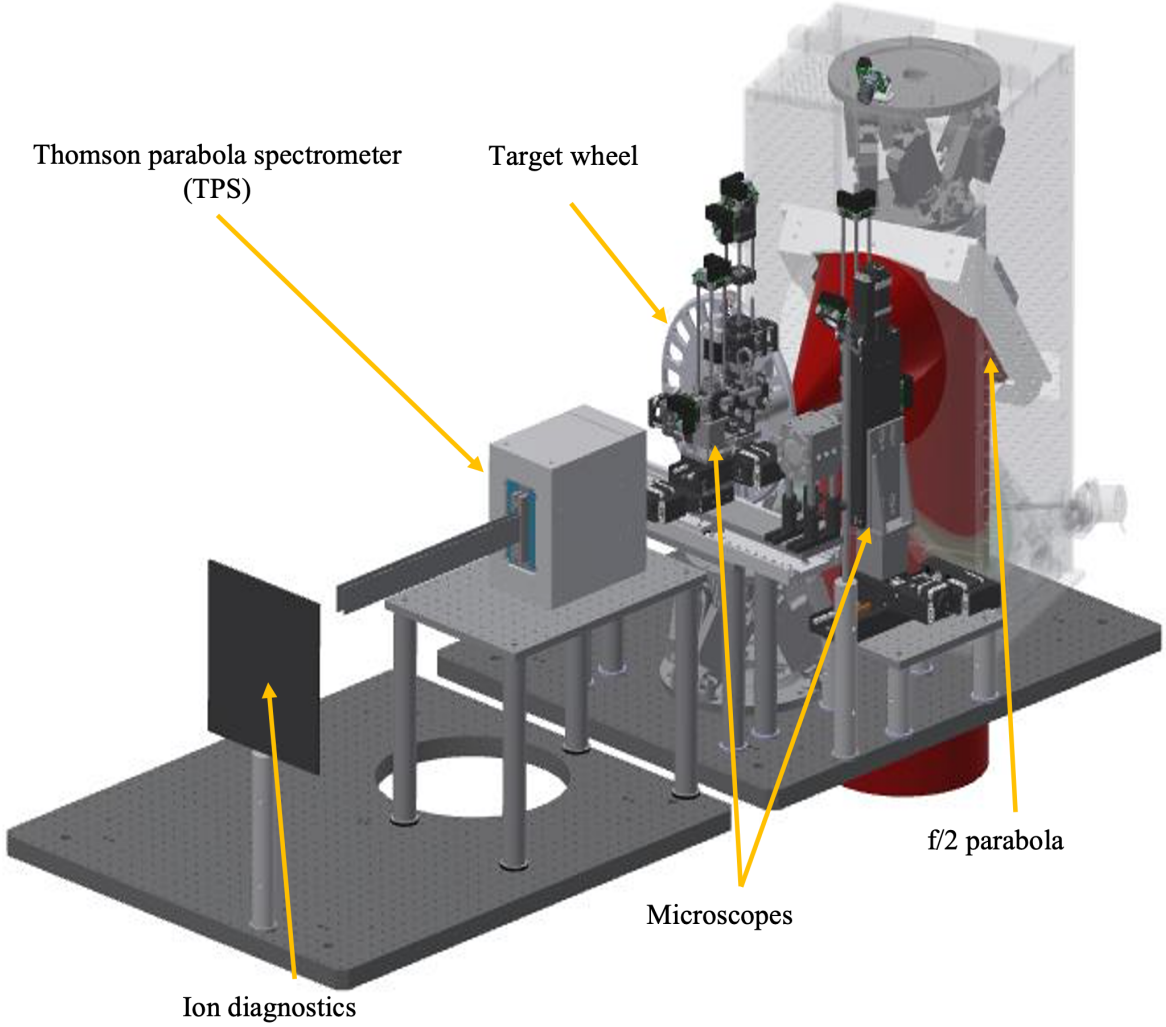

Figure 3.1.: In the HF setup, the incoming laser beam is focused by an f/2 OAP onto a target, mounted within a target wheel which is positioned on top of a hexapod. The incident angle for the laser pulse on the target is 21° to mitigate the risk of back reflection into the laser chain. Two microscopes on either side of the target wheel are installed to enable the automated positioning of the target within in the laser focus and in order to assess and improve the attenuated laser focus. They are removed prior to a full power laser shot. A TPS in combination with ion diagnostics is used to analyze the accelerated ions.

The main setup is inside the HF vacuum chamber, which is connected to the LBD. A mirror below the chamber guides the beam onto a f/2 copper Off-Axis Parabola (OAP) mounted on a remote controlled hexapod, focusing the beam from 28 cm in diameter down to 2 µm Full-Width at Half-Maximum (FWHM). The transmission efficiency through the LBD is measured in regular time intervals. This is necessary, since a blackening of the beamline mirrors due to the high laser fluence on the optics can cause a reduction of the energy in the cave over the course of several weeks in-between regular cleaning intervals. Typical transmission values for the HF cave range from $(68.4 \pm 2.0)\,\%$ to $(70.0 \pm 2.0)\,\%$ of energy measured at the location of the second crystal of the laser main amplifier to the focus position in the HF target chamber.

The laser beam can then be inspected using the downstream microscope. The laser far field can be analyzed by two cameras with a high and a low magnification, respectively. The microscope is also used to image the laser near-field as well as the wavefront. The latter is done via a custom Shack-Hartman sensor, which is used to optimize the deformable mirror in the LBD, mentioned in Sec. 3.1 [83]. The microscope also features a fiber for the target heating setup, detailed in Sec. 4.2.

As a consequence, the microscope determines the focus position of the laser pulse within the vacuum chamber, the so-called Target Chamber Center (TCC). Therefore, the microscope defines the final position of the targets. The incidence angle of the laser on the target was chosen to be 21° in order to mitigate the risk of back reflection into the laser chain. Downstream of the target on the axis of the laser, a scatter screen is positioned, to quantify the amount of light transmitted through the targets during the laser-target interaction [85].

3.2.1. Target fabrication and characterization

The targets are thin, self-supporting foils with thicknesses ranging from 100 to 600 nm. They are attached to a metallic target holder, containing 40 individual targets holes with a diameter of 1.5 mm. These holders are then mounted onto a plastic target wheel via small magnets. The target wheel can be rotated and has a capacity of up to 19 target holders. The wheel itself is mounted on a remote controlled hexapod which enables a precise positioning (<16 µm in longitudinal direction, which is roughly the Rayleigh range of our setup) of the targets in the laser focus. Prior to each experiment, the hexapod and target wheel position for each target is determined and saved, so that it can be easily retrieved right before a full power shot. In order to facilitate the automated positioning of the targets, the upstream microscope is installed. Ensuring a good overlap of both

microscopes in regular intervals is crucial for a good automated target positioning. Details of the positioning system can be found in Ref. [86], including a detailed description of both microscopes.

The targets are produced in a commercial vacuum coater (SYRUSpro by Leybold Optics [87]). Solid gold is evaporated using an electron gun onto a substrate, covered by a parting agent. During the evaporation, the thickness of the foil is monitored via an oscillating quartz crystal. Once the desired thickness is reached, the substrate is carefully placed in distilled water, hereby dissolving the parting agent, in a way that the gold foil is floating on top of the water. It is then placed on top of a target holder and taken out of the water for drying, attaching to the holder via adhesion. During the course of this thesis, two different parting agents were used: trimethylglycine ($C_5H_{11}NO_2$) referred to as betain and sodium chloride (NaCl). A comment on the effect of this change on the gold acceleration can be found in Chap. 5. The second type of target material used in this thesis are plastic foils made from polyvinyl formal, so-called Formvar. They are produced via spin coating and do not require a parting agent for production.

While the gold that is used to produce the free-standing foils is chemically very pure (typical values for purity of gold are 99.9 % [88]), it is possible that impurities are introduced during the target fabrication process. A common technique to investigate the composition of a material and a way to detect such impurities is using X-ray Fluorescence Analysis (XFA). In 1913, Bohr introduced his model on the constitution of atoms, derived from the observations made by Rutherford of the scattering of α particles in a thin gold foil. In Bohr's model, the atom is made of a positively charged nucleus, making up most of the atom's mass, surrounded by a system of electrons. He further concluded that the electrons are on discrete energy levels, so-called shells, and unified his theory with previous observations about the absorption and emission of light by individual nuclei [89]. The different shells are enumerated by letters in alphabetic order, starting with the letter "K". Electrons on the shells closer to the nucleus experience a higher binding energy than those on the outer shells. If a sample is irradiated with X-rays of sufficient energy, they can be absorbed via the photoelectric effect by an electron on an inner shell, as indicated in the schematic in Fig. 3.2. The electron is subsequently ejected, leaving a vacancy which will be filled by an electron from an outer shell. The difference in the binding energy in this transition can be released via an X-ray photon with a characteristic energy (fluorescence) or by expelling another electron from the atom (Auger electron). For atoms heavier than sodium (Z>11), X-ray emission is dominant over the emission of an Auger electron.

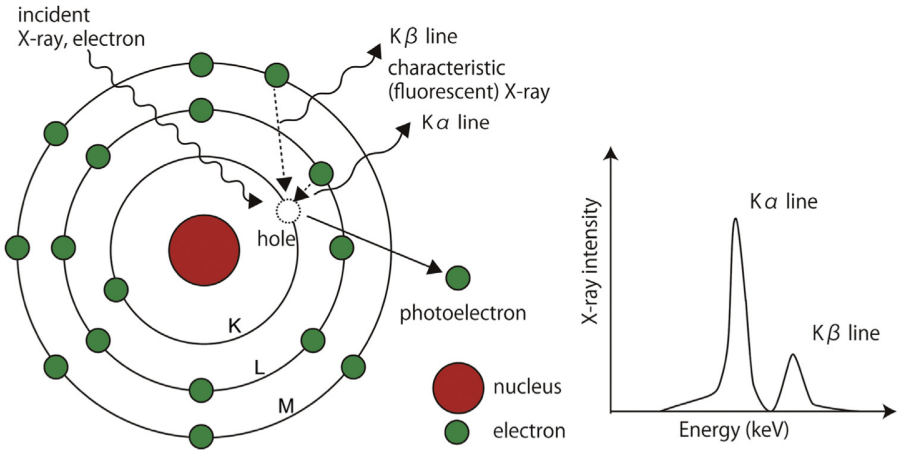

Figure 3.2.: The atom consists of a positively charged nucleus with electron orbiting around it on discrete energy levels. X-rays with sufficient energies can ionize electrons from an inner shell. The created vacancy is filled by an electron from an outer shell. The difference in binding energy between the energy levels can be emitted via an X-ray photon with a characteristic energy. By analyzing the emitted X-ray spectrum, elements can be identified. Image taken from Ref. [90].

The recorded energy spectra of the characteristic X-rays can then be compared to the energies listed in databases [91] to identify elements in a sample. By comparing the intensity of the emitted lines, a quantitative analysis of the abundance of elements is possible. For the analysis of the gold foils employed throughout this thesis a compact, portable device was used, as depicted in Fig. 3.3, providing immediate feedback on the sample composition.

3.2.2. Heavy-Ion Thomson parabola spectrometer

A TPS is a mass spectrometer invented by J. J. Thomson in 1911 [93], allowing for simultaneous detection of energy, momentum and mass-to-charge ratio. This makes it a suitable and commonly used device for the analysis of ion spectra accelerated by lasers. It consists of a pinhole, a parallel or anti-parallel magnetic and electric field and a detector, as indicated in Fig. 3.4, with the magnetic field lines depicted as black arrows and the electric field lines as white arrows.

Particles are deflected based on the Lorentz force (c.f. Eq. (2.6)). In the small angle

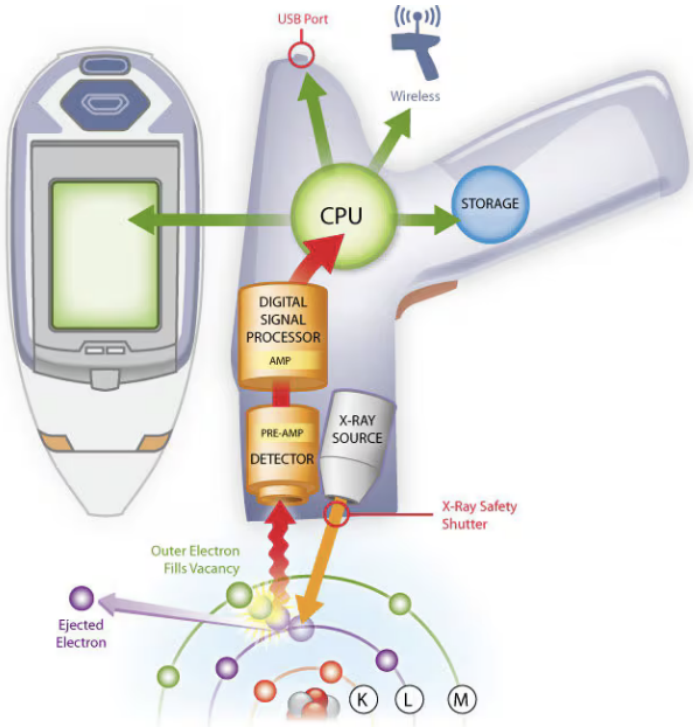

Figure 3.3.: Portable X-ray fluorescence analyzer were developed to provide fast and easy information about the composition of samples, e.g. for mining and exploration. These compact setups house the X-ray source as well as the detector, with the incident and fluorescent radiation entering and exiting the sample from the same side under different angles. The signal from the detector is further amplified by a digital signal processor with a CPU analyzing the signal. The analyzed data is then displayed on the device, can be transmitted wireless, via an USB port or stored in the internal storage. Image taken from Ref. [92].

approximation, the particle's deflection is described by the parabolic equation

$$x_{\mathrm{mag}} = \frac{m}{q} \frac{l_E E \left(d_E + \frac{l_E}{2}\right)^2}{l_B^2 B^2 \left(d_B + \frac{l_B}{2}\right)^2} \cdot y_{\mathrm{el}}^2, \tag{3.1}$$

with the deflection due to the magnetic force x_{mag} and the electric force y_{el}, the particle's mass m and charge q, as well as the electric and magnetic field strength, B and E, respectively. The drift length in the electric field l_E and in the magnetic field l_B as well as the drift length from the end of the electric and magnetic field to the detector, d_E and d_B, respectively, are as well indicated in Fig. 3.4. If the deflections by the magnetic

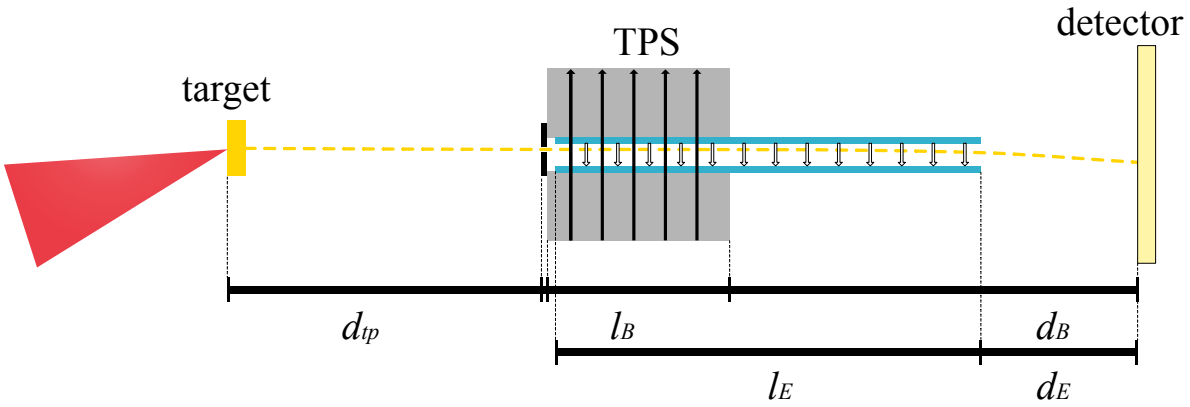

Figure 3.4.: By the interaction of the laser pulse (red) with the target (left), ions are accelerated (yellow dotted line). After a distance d_{tp} they enter the Thomson parabola spectrometer through a pinhole (gap in black rectangles) consisting of a parallel magnetic and electric field, depicted by the black and white arrows, respectively, where they are deflected by the Lorentz force over a distance l_B and l_E, respectively. The ions then travel over a drift length d_B and d_E before reaching the detector.

and electric field are decoupled, Eq. (3.1) can be rewritten as

$$x_{\mathrm{mag}} = \frac{qeBl_B\left(d_B + \frac{l_B}{2}\right)}{\sqrt{2mE_{\mathrm{kin}}}} \tag{3.2}$$

$$y_{\mathrm{el}} = \frac{qeEl_E\left(d_E + \frac{l_E}{2}\right)}{2E_{\mathrm{kin}}}, \tag{3.3}$$

including the particle's kinetic energy E_{kin}. This means, that particles are deflected onto parabolic traces depending on their mass-to-charge ratio with their position on the parabola depending on their kinetic energy. Faster particles are deflected less and in the limit of infinitely energetic particles all traces meet at the origin (where also neutral particles hit), the so-called zero point [94,95]. This decoupling is not valid for the heavy-ion TPS in use for our experiments, as will be discussed at the end of this section.

Resolving individual charge states is challenging for heavy ions in the mass range of $A \approx 200$ due to the small differences in their mass-to-charge ratio compared to lighter ions. For a given ion species, the resolution can be improved by increasing the field strengths or the drift lengths or by decreasing the pinhole size. Each of these parameters has its limitations. Because of the strong Electromagnetic Pulse (EMP) during the laser-target interaction it is beneficial to use permanent magnets, which have a maximum achievable field strength of about 1.4 T for neodymium-based materials. The electric field

strength is limited by potential breakdown. Increasing the drift lengths is constrained by the available space in the experimental vacuum chamber and the pinhole size needs to be large enough to ensure a sufficient signal-to-noise ratio in the detector, as will be discussed in Sec. 3.3. Therefore, in a separate study, the heavy-ion TPS was designed [96], well summarized in Ref. [15].

The magnetic field is formed by permanent magnets with a designed average field strength of $B = 0.85\,\mathrm{T}$ over a length of $l_B = 168\,\mathrm{mm}$ and a gap of 25 mm. Custom ceramic blocks are used to hold the electrodes inside the magnetic yoke. The electric field starts 3.2 cm after the magnetic field. The electrodes consist of a copper plate, embedded into a printed circuit board structure. Vacuum-compatible Kapton-isolated cables are connected for high-voltage supply. The gap between the electrodes amounts to 1.5 cm. The resulting electric field is variable and was operated up to a maximum of $E = 30\,\mathrm{kV/cm}$ over $l_E = 580\,\mathrm{mm}$. The outer shape of the top edge of the electrode was adapted such that the trajectories of Au^{35+} (and gold ions with higher charge) do not crash into the electrodes. For the same reason the position of the pinhole was shifted relative to the centre of the gap by 2.5 mm. The drift length could be varied slightly depending on the used charged particle detector, but if not indicated otherwise is assumed to be $d_B = 61.5\,\mathrm{cm}$ and $d_E = 17.1\,\mathrm{cm}$, respectively. In combination with a pinhole of 500 µm in diameter the TPS captures a solid angle of $\Omega = 1.3 \cdot 10^{-3}\,\mathrm{msr}$.

Once the field strengths and drift lengths are designed, the resolution of the TPS depends on the pinhole diameter. The ion beam spot size at the location of the detector s can be calculated via

$$s = 2 \cdot \left[r_p + \frac{r_p}{d_{tp}} (l_E + d_E) \right]. \tag{3.4}$$

The energy resolution is then given by the energy range covered by the beam spot on the detector divided by its center energy [97]

$$\frac{\Delta E_{\mathrm{kin}}}{E_{\mathrm{kin}}} = \frac{2s}{x_{\mathrm{mag}} \left(1 - \left(\frac{s}{2x_{\mathrm{mag}}} \right)^2 \right)^2} \approx \frac{2s}{y}. \tag{3.5}$$

Figure 3.5 shows the energy resolution for four different pinhole diameters available during this thesis.

In a similar way the energy limit up to which two charge states can be distinguished,

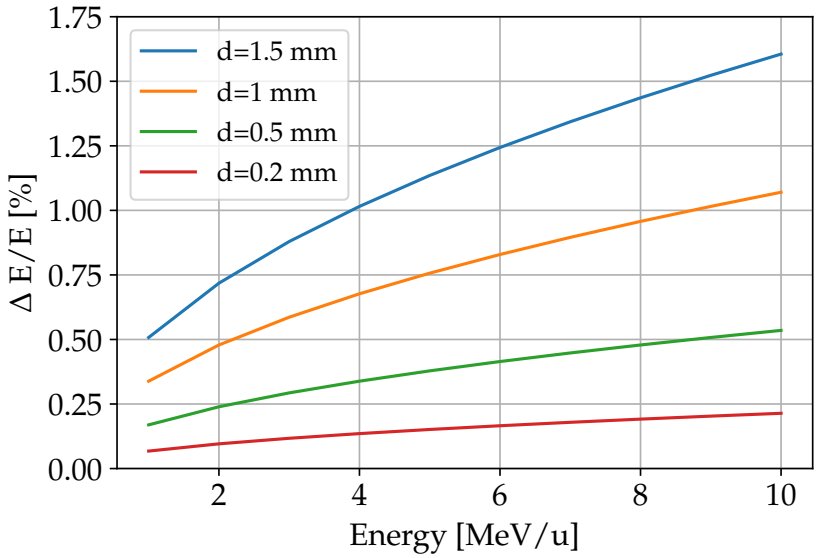

Figure 3.5.: The calculated energy resolution of the TPS in the HF setup for Au^{35+} for four different pinhole diameters.

i.e. the "merging" energy E_m can be calculated via

$$E_m = \frac{q_i E l_E \left(d_E + \frac{l_E}{2}\right)}{s R_Q}, \tag{3.6}$$

where $R_Q = \frac{q_1+q_2}{q_1-q_2}$, with $q_1 > q_2$ for two particles of the same species and q_i being the charge state in questions. The corresponding energy limits for a few charge states in our setup are displayed in Tab. 3.1.

Table 3.1.: Energy limit up to which two charge states of the same species can be distinguished for a pinhole diameter of d_p =0.5 mm and a distance of d_B = 61.5 cm. For higher energies, the traces start overlapping.

	E_m [MeV/u]
C^{5+} into C^{6+}	24.925
C^{6+} into C^{5+}	20.771
Au^{30+} into Au^{31+}	1.415
Au^{50+} into Au^{51+}	1.406

The analytical description discussed above assumes idealized constant fields. In the experiment, however, the particle's deflection is influenced by fringe fields. To quantify their effects, the commercial 3D electromagnetic simulation software CST Studio Suite [98]

is used. The exact heavy-ion TPS geometry is imported via a STEP file of the CAD model, enabling a realistic simulation of the fringe fields, which are then exported as field maps.

Due to the geometry of the heavy-ion TPS with very long electrodes, the drift length in the electric field depends on the ion's energy, as illustrated in Fig. 3.6. Ions of the same species with lower kinetic energies will leave the electric field earlier than those having higher kinetic energies. Therefore, the deflection by the electric and magnetic field are not decoupled, as assumed for Eq. (3.2) and (3.3).

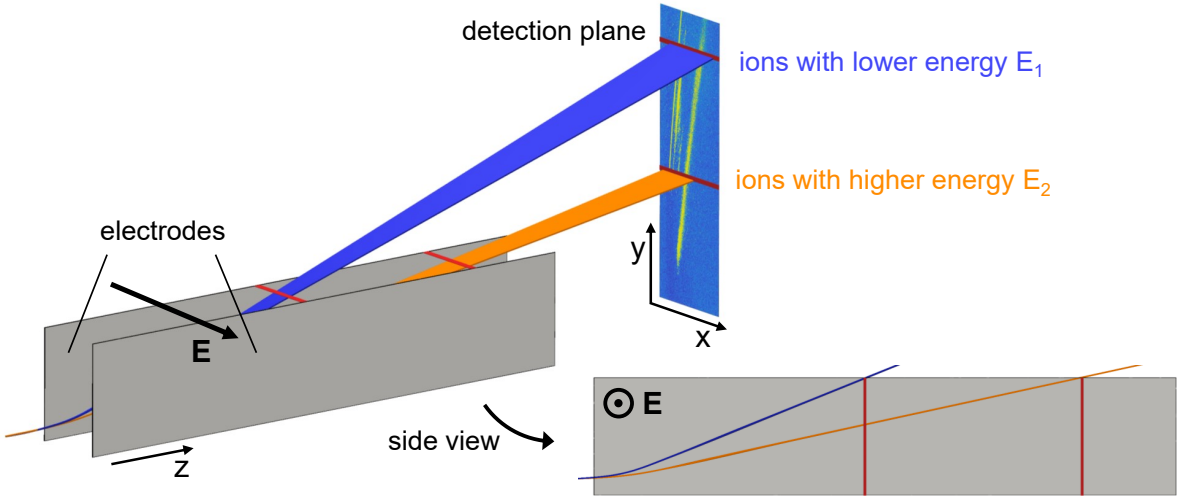

Figure 3.6.: For a fixed mass-to-charge ratio, particles with a lower kinetic energy will be deflected more by the magnetic field than particles with a higher kinetic energy. Due to the long electrodes of the heavy-ion TPS this means that particles with a lower kinetic energy will leave the electric field earlier than particles with a higher kinetic energy. The deflection by the magnetic and electric field are therefore not decoupled. Figure taken from Ref. [15].

Instead, the particle deflection is simulated using the particle tracking code from the physicsbox package [99], by loading the magnetic and electric fields simulated by CST Studio Suite [98]. The simulation also includes the relevant distances, e.g. the drift length towards the detector. The particles, i.e. the relevant species with their charge state and energy ranges are initialized and then their motion through the fields is tracked based on a Runge-Kutta method using the python ODE solver "dopri5" [100]. The energy array was chosen to follow a power law in order to generate evenly spaced distances in the direction of the energy. This way a mesh can be created, that in one dimension is intersected by iso-energy lines and in the other by iso-mass-to-charge ratios. By overlaying this mesh with the acquired data and analyzing the intensity of the signal in each mesh grid, the

spectra of the accelerated ions are generated, as will be shown in Chap. 6. The next section will cover the different detectors used in this thesis.

3.3. Relevant charged particle detectors

The choice of the detector for an experiment needs to be tailored to the experimental conditions as well as to the desired observables and the needed precision. The high repetition rate of ATLAS-3000 makes the use of online detectors desirable, providing instantaneous feedback without interruption for venting cycles or similar. On the other hand, the interaction of the laser pulse with the target creates a very strong EMP, posing a challenge for any electronics built into online detectors, making their use not straight forward. Therefore, offline detectors are still commonly used diagnostic tools in laser-plasma experiments.

This section introduces the particle detectors employed throughout this thesis. Columbia Resin #39 (CR-39) is an offline nuclear track detector, with a tedious and time consuming analysis procedure. Additionally, it needs to be refreshed after each shot, necessitating frequent venting cycles. Nevertheless, because of its outstanding parameters, highlighted in the following, it remains a detector of choice for a lot of experiments.

To take advantage of the high repetition rate available by today's high-power laser systems, the laser-plasma community puts a lot of effort in the establishment of online detectors. While many of such detector systems already exist for experiments accelerating protons and lighter ions like carbon and oxygen ions, Multi-Channel Plate (MCP) detectors in combination with phosphor plates and a camera are so far the only online detection available for heavy ions like gold [101]. However, using them includes an elaborate setup with strong constraints on the vacuum quality due to the high voltage that is applied. Additionally, with increasing size of the active area, they become very expensive and their response does not increase linearly with the number of impinging particles, making an absolute calibration very difficult.

Furthermore, protons and light ions can be detected by irradiating a Complementary Metal-Oxide Semiconductor (CMOS) detector like the RadEye pixel detector [82, 102]. However, in preliminary studies using 1 MeV/u gold ions from a Tandem accelerator, the CMOS detector showed quick degradation due to radiation damage. This is probably due to the higher relative stopping power of gold ions compared to protons. Therefore, in the course of this thesis the use of two other online detectors was tested. One employs an inorganic scintillator in combination with a scientific CMOS (sCMOS) camera. The

second one uses an organic scintillator in combination with a large area CMOS detector.

3.3.1. Columbia-Resin #39

Solid-State Nuclear Track Detectors (SSNTD) are a well established method for the detection of charged particles [103]. If the energy of the ions passing through the material is above a material dependent threshold value they induce damage, e.g., by breaking of covalent bonds, leaving a latent track of about 10 nm in diameter. The produced damage is proportional to the stopping power of the ions in the medium, described by the relativistic Bethe-Bloch formula (see Eq. (2.14)).

By wet etching, the tracks created in the SSNTD can be enlarged so that they become visible under an optical microscope, a process well illustrated in Ref. [104], maintaining the proportionality of the pit size to the induced damage. SSNTD can consist of various materials, differing mainly in their detection threshold for the lightest resolvable particle. A commonly used SSNTD is polyallyldiglycol carbonate ($C_{12}H_{18}O_7$), also referred to as Columbia Resin #39 (CR-39). It can be used for the detection of protons with energies down to 1 MeV with a detection efficiency of 100 %, while staying transparent for electrons and gamma rays. Having been used for a long time [105], they are still a common detector with continued relevance [106].

The CR-39 slabs used throughout this thesis were manufactured by Track Analysis Systems Ltd. [107] with 1 mm thickness and an active area of $10 \times 20\,\mathrm{cm}^2$. After irradiation they were etched for 40 minutes in 6-molar NaOH at a controlled temperature of 80 °C. The thus enlarged pits were then inspected with an autofocus Zeiss Axitron II microscope at 20x magnification connected with an IDS UI-6280SE-M-GL R3 camera.

The pits are detected by the pattern recognition software Samaica [108], that fits ellipses to them. For a good suppression of the background a careful adjustment of brightness and contrast settings of the pattern recognition is necessary. The aim is to keep the brightness as low as possible, while still resolving even small pits. The software then saves the metadata of the fits, like their position, enclosed area, central brightness and ellipticity, labeled as the ratio of the minor to major semi-axis. Because of the proportionality of the damage to the deposited energy per path length $\mathrm{d}E/\mathrm{d}x$, these values correspond to physical properties of the impinging ion beam, like the angle of incidence [109] as well as ion energy and ion species [106], a consequence of Eq. (2.14). Due to their smaller mass, protons in general produce smaller pits and can therefore only be detected when their Bragg peak is close to the surface of the CR-39 track detector. For our etching conditions, this results in a maximum depth of the Bragg peak of $\approx 150\,\mu\mathrm{m}$.

For pits on the CR-39 track detector front side this corresponds to energies below 3 MeV. It is also possible to detect the pits from protons exiting the material, i.e. pits on the detector backside. Considering the discussed depth of the Bragg peak, this corresponds to protons in the range of 8 to 9 MeV.

After successful scanning, the signal is further processed to reduce the background. While signals from noise or surface damage artefacts can have random fit parameters, those for pits created by the same species are very similar in their features. Therefore, the signal is filtered in three sequential iterations using correlation plots, namely the ratio of the minor to major semi-axis versus the central brightness of the pits, the area enclosed by the fitted elipse versus the ratio of the minor to major semi-axis and the central brightness versus the enclosed area. An example of such correlation plots is displayed in Fig. 3.7, taken from Ref. [15]. In every step, the data is gated by selecting the signal region by hand. After every step, the rejected background is checked for real ion signals, which were falsely attributed to the noise region, in which case the filtering needs to be repeated. If the gating delivers satisfying results, only the accepted data is transferred to the next gating step.

For the first step, the ratio of the minor to major semi-axis is plotted versus the central brightness in Fig. 3.7 (a), with the selected ion signal marked in black and the blue signal belonging to background. Pits originating from ions are round with only small deviations due to their angle of incidence. Therefore, the ratio of the minor to major semi-axis for pits from ions is close to unity. Furthermore, with our etching conditions, the pits created by ions appear as black dots under the microscope, which results in a low central brightness, in contrast to most of the noise signals captured by the Samaica fitting routine.

In the second step, the enclosed area is evaluated versus the ratio of the minor to major semi-axis. The enclosed area varies depending on the species. Therefore, in Fig. 3.7 (b) gold ions with the largest area can be identified in orange, oxygen ions are plotted in violet and carbon ions in yellow. The data from pits in black were attributed to noise.

In the last step, the central brightness was plotted versus the enclosed area. In Fig. 3.7 (c) this is displayed for gold ions. Since the gating conditions in the two previous steps were already successful, the signal from noise in this gating step plotted in orange is low compared to the ion signal plotted in green.

The influence of the gating on the signal is displayed in Fig. 3.8, for a shot on a 400 nm thick, heated gold target detected by a CR-39 track detector positioned behind the TPS in the HF experimental setup. Figure 3.8 (a) shows the signal before applying gating

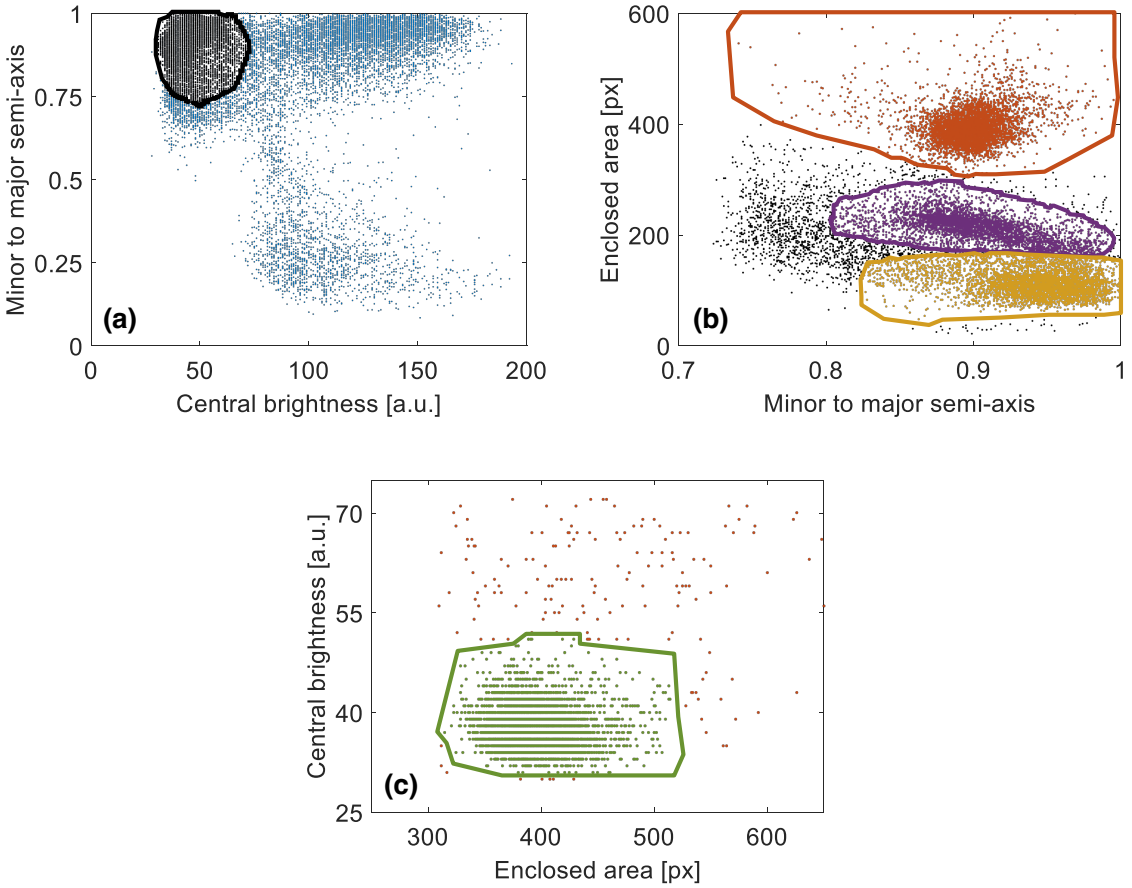

Figure 3.7.: The signal from the CR-39 track detectors can be gated on different fit parameters. To suppress background signals, the ion signal is filtered from three correlation plots. In (a), the ratio of minor to major semi-axis is plotted versus the central brightness. The chosen gate including the selected ion signal is marked in black against the background noise in blue. In the next step in (b), the enclosed areas of the selected signals from the first gate are plotted versus the ratio of the minor to major semi-axis. Here the gate for gold ions and the corresponding signals are marked in orange, violet refers to oxygen ions and yellow to carbon ions, while black pits belong to noise. In the last step in (c), the central brightness is plotted for signals included in the golden gate from the previous plot versus the enclosed area. The set gate and the hence selected pits are marked in green while background signals are displayed in orange. Figure adapted from Ref. [31].

conditions. The ions are deflected by the Lorentz force based on the magnetic field along the abscissa and along the ordinate based on the electric field. The values of the abscissa and the ordinate were adjusted such that the origin of both axis aligns with the zero point, i.e. the position of neutral and hence undeflected particles. The color of the individual pits is based on the area enclosed by the elliptic fit to the corresponding fit. Figure 3.8 (b) then displays the same data after applying gating conditions to suppress background signals. Especially the contribution from noise with small pit areas is significantly reduced while the ion signal trace is unaltered. Further details of the data captured by the CR-39 track detector will be covered by Chap. 4-6.

The next section presents two options for online detection of heavy ions.

3.3.2. Scintillating screens

Scintillating screens rely on luminescence, the spontaneous emission of visible or near ultra-violet light from a material excited by, e.g., γ rays or accelerated ions. They are divided into inorganic scintillators based on crystals and organic scintillators based on plastics or liquids. Scintillators are characterized by their rise and fall time (decay time), their conversion efficiency (light yield) and their emission wavelength. Furthermore, a linear response of emitted photons to the exciting radiation is important. In general, inorganic scintillators have the best light output and linearity, but are slow in their decay time in contrast to organic scintillators, which have a lower light yield but a faster response.

Scintillating screens, imaged with CMOS detectors or cameras or Charged Coupled Devices (CCDs), are an established method for the detection of accelerated electrons with absolute calibration for particle numbers being available [110, 111]. While for laser-accelerated protons first being mainly employed for the analysis of the spatial profile [112, 113], they have also been used in combination with a TPS [114]. In the course of this thesis, this was translated to experiments with laser-accelerated heavy ions.

For the use of online detection of heavy ions at CALA, both organic and inorganic scintillators were used. Due to their optical properties, different imaging techniques had to be employed which will be introduced in the following.

Lanex scintillating screens

For our experiments we used two Lanex screens, Cawo OG 16 [115] and DRZ high [116], inorganic scintillating screens with Gd_2O_2S: Tb as the scintillating medium placed on a

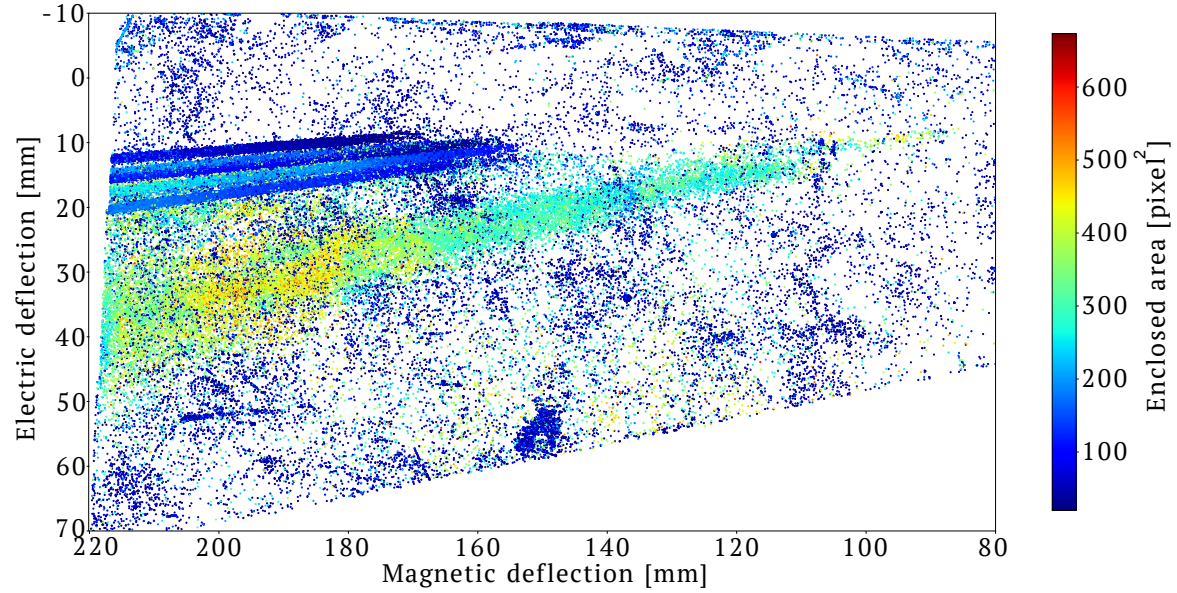

(a) Before gating

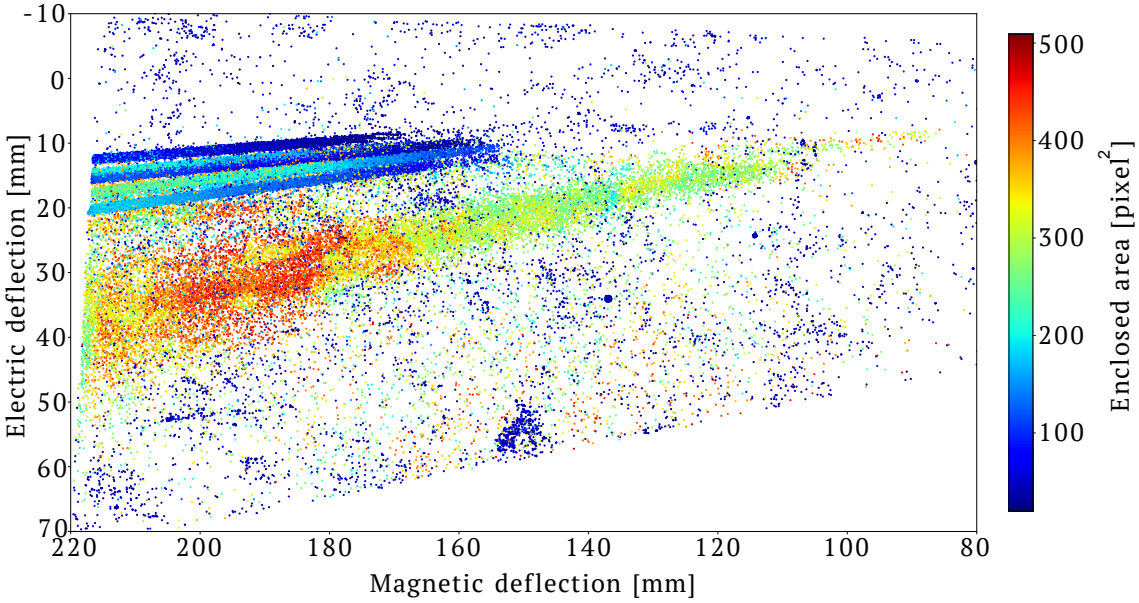

(b) After gating

Figure 3.8.: The plots show the signal from a scanned CR-39 track detector before gating in panel (a) and after gating in panel (b). The Lorentz force deflects the ions based on their mass-to-charge ratio and their kinetic energy along the abscissa based on the magnetic field and along the ordinate based on the electric field. The values of the abscissa and the ordinate were adjusted to that the origin of both axis aligns with the zero point, i.e. the position of neutral and hence undeflected particles. The color of the individual pits is based on the area enclosed by the elliptic fit to the corresponding fit.

plastic support layer protected by a Polyethylene terephthalate (PET) layer. For the DRZ high screen the thickness of the protective layer is specified to be 6 µm, for the Cawo screen this information is not available.

The screens feature a long luminescence lifetime time of 1 ms [117], which is orders of magnitude longer than the laser pulse or the bunch length of the accelerated ions. Furthermore, they have a sharp emission peak at 546 nm [110], which is in-between the laser fundamental and second harmonic emission bandwidth centered around 800 nm and 400 nm, respectively.

In the past, Lanex screens have been mainly used as a diagnostic tool for electron acceleration [110,111,118], showing that the DRZ high screen has a higher light output when irradiated with $(10.6 \pm 3.63) \cdot 10^9$ photons/sr/pC compared to $(3.7 \pm 0.7) \cdot 10^9$ photons/sr/pC for the Cawo screen [118]. While this calibration cannot be directly translated to protons and ions, showing a $> 60\,\%$ higher light yield per deposited amount of energy for protons compared to electrons, the ratio between different screens stays comparable [117].

Since the Lanex screens are not transparent, the imaging needs to be set up on the front side facing the protective layer. For protons and electrons, the screens can also be irradiated from the backside through the support layer, allowing for a compact setup without interfering with the particle beam. Due to the higher stopping power of gold ions, this was not possible for our experiment, since the heavier ions would have been stopped in the support layer without creating signal in the active layer.

Therefore, a mirror guided the emitted light out of the chamber to a back-illuminated scientific CMOS (sCMOS) camera KURO-1200B [119], as depicted in Fig. 3.9 equipped with a Tamron zoom objective SP 24-70mm F/2.8 Di VC USD [120]. The KURO-1200B sensor features 1200 x 1200 pixels with $11 \times 11\,\mu m^2$ size and a pixel fill factor of 100 %. Its quantum efficiency has a peak for a wavelength between 500 to 600 nm, reaching more than 90 % detection efficiency. It was operated in its default setting with air cooling. Additional cooling by water is possible. The exposure time was set to 200 ms. In order to protect the sensitive camera from EMP, it was placed in a custom copper housing, with electrostatic isolation from the chamber and grounding. The setup was made light tight as indicated in Fig. 3.9 by the black line in order not to decrease the signal-to-noise ratio in the sCMOS camera with laser light or light emitted during the laser-target interaction.

EJ-200 sctintillator

Another setup (employed for the experiment described in Sec. 5.1) features the use of an EJ-200 organic scintillator, with a fast rise time of 0.9 ns and 2.1 ns decay time, emitting

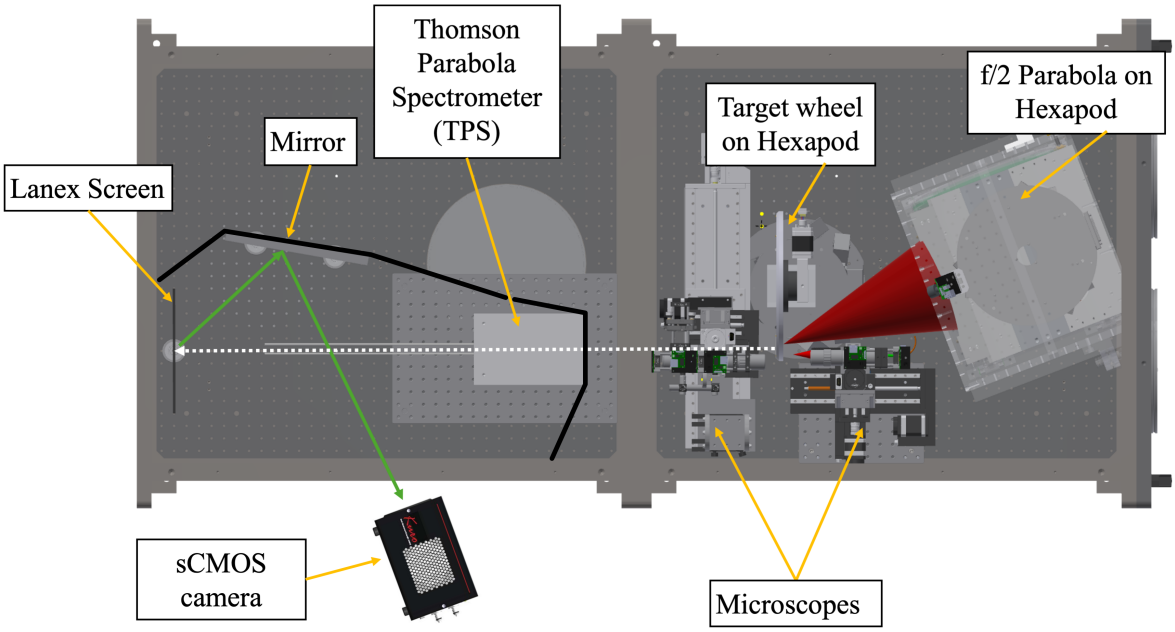

Figure 3.9.: In order to use a Lanex screen for the detection of heavy ions (accelerated from the target, indicated by the white dotted line), a mirror guides the emitted light (indicated by green arrows) out of the vacuum chamber to the sCMOS camera. To suppress the influence of stray light coming from the laser or the laser-target interaction, the area indicated by the black line is made light tight.

light at 425 nm being 1.1 mm thick [121]. For organic scintillators, the light output is often quantified in percent of the light output of anthracene ($\approx 2 \cdot 10^4$ photons/MeV). For the EJ-200 the light output is quantified to be 64 % of the value for anthracene.

Since the EJ-200 scintillator is transparent, light can be collected from the back side. For our experiments we used a PS-1412 CMOS detector from ISDI Ltd with a size of $14 \times 12\,\mathrm{cm}^2$ and a quadratical pixel size of $50 \times 50\,\mu\mathrm{m}^2$. It is placed on a ceramic substrate, with a 2 mm thick Fiber Optical Plate (FOP) on top which is radiation hard and non-browning, therefore ensuring a protection of the pn-junction while maintaining good optical quality. The detector has a quantum efficiency of 51 % at a wavelength of 550 nm [122]. The EJ-200 scintillator was placed directly to the PS-1412 detector and fixed with Kapton tape on the edges. The light emitted by the scintillator is then guided by the FOP, which may introduce a slight reduction of resolution and efficiency.

For the CMOS detector the incoming photons generate electron-hole pairs in a pn-junction, changing the potential difference in the space charge region (depletion zone) of the pn-junction. This signal is then amplified by a preamplifier and digitized by an Analogue-to-Digital Converter (ADC). The read-out values are digital signals, measured in Analogue-to-Digital Units (ADU), which for a good detector should be proportional to the number of incident particles. For pixelated CMOS, each pixel consists of a photodiode and transistors that manage the read-out and reset after irradiation [123, 124].

In addition, thermal excitation can promote electrons across the band gap, creating a reverse bias current I_R, without ionization events, also referred to as dark current, reducing the dynamic range of the detector. It depends on the band-gap energy E_g and the temperature T [123]

$$I_R \propto T^2 \exp\left(-\frac{E_g}{2k_B T}\right). \tag{3.7}$$

Cooling the detector can therefore reduce the dark current. On the other hand, if, e.g., long operation times increase the heat load, this can create higher dark current. Radiation damage caused by incident particles can create intermediate energy levels in the band gap, therefore increasing the probability for thermal excitation and consequently increasing the dark current [123]. Long time intervals before the readout can further increase the dark current.

Careful analysis is needed in order to retrieve a spectrum from this setup. The response of the scintillator to the incident particles, depending on their energy and their absolute number per energy interval, needs to be known. The scintillator then converts this energy to photons with an narrow energy bandwidth. In a last step the quantum efficiency

of the detector to the photon's wavelength needs to be known to fully deconvolve the signal and retrieve absolute particle numbers from the ADU values. Such a calibration is currently not available for the setup used in this thesis.

4. Impact of target heating on heavy-ion acceleration

For the laser-based acceleration of heavy ions, we focus a laser pulse with ultra-high intensity on gold foils with thicknesses ranging from 100 to 600 nm. The surface of these foil is covered by contaminants from the surrounding air, typically consisting of hydrocarbons, oxygen and nitrogen. While this contamination layer significantly influences the acceleration dynamics of heavy ions due to their beneficial mass-to-charge ratio, the thickness of this layer was measured to amount to only a few nanometers [125].

In several experiments, however, the acceleration of protons and light ions could be successfully suppressed through the use of target cleaning techniques in an attempt to enhance the acceleration of heavier ions [126–128]. In earlier work by our group, radiative heating was employed as a target cleaning method during two experimental campaigns, conducted at different facilities.

The first experiment was conducted at the Texas Petawatt laser (TPW) [129] with a pulse energy of about 119 J within pulse durations around 140 fs at a central wavelength of 1057 nm. During this campaign [15], the gold cutoff energy was significantly increased for heated targets compared to shots on unheated targets. Additionally, less protons and carbon ions were accelerated. For protons, the cutoff energies were significantly reduced while for carbon ions, mainly the number of low energetic ions was decreased with a slight increase in their cutoff energies. However, the gold ion charge-state distribution was not affected by the heating.

For the second campaign, the PHELIX laser at GSI [130] was used, delivering pulses with energies ranging between 170 to 200 J within pulse durations of 500 fs at a central wavelength of 1054 nm. Similarly to the previous experiment, the target heating significantly reduced the number of accelerated protons [15, 31]. For two shots on heated foils, no proton signal at all was detected. The cutoff energy for carbon and oxygen ions was slightly enhanced for heated shots compared to unheated shots. In contrast to the beamtime at the TPW, no impact on the cutoff energy of the gold ions was observed. On the contrary, the shot with the highest cutoff energy was achieved on an unheated gold foil.

After employing the long and intermediate pulse lengths at the PHELIX laser and TPW, respectively, the present experiments at the ATLAS-3000 system are expected to add further insights on the effect of heating by using much shorter pulse lengths than during the previous campaigns. For this, the target cleaning setup used at the TPW and the PHELIX laser was further improved and adapted for the HF cave [131, 132]. It consists of a continuous wave (cw) laser and a Near Infrared (NIR) spectrometer, which is used to determine the target's temperature by fitting Planck's law to the emitted infrared spectrum. Therefore, in this chapter, first the physical foundation of black body radiation and temperature determination via Planck's law will be laid out. Following, the heating setup in the HF cave will be introduced before explaining the routine for calibration and temperature retrieval. A dedicated study will investigate the details of the target heating before the impact of target heating on the laser-based acceleration of gold ions at the ATLAS-3000 system will be presented.

4.1. Black body radiation and Planck's law

Planck's radiation law describes the spectral density of electromagnetic radiation dissipated by a black body in thermal equilibrium at temperature T as a function of the wavelength λ or the frequency ν. Published in 1900 [133, 134], it unified previous radiation laws, including Rayleigh-Jeans' law or Wien's displacement law. For this Planck introduced the quantization of energy, which laid the foundation of what was to become quantum physics. The spectral radiance of a black body is expressed via

$$S_{\lambda,\mathrm{BB}}(\lambda, T) = \frac{2hc^2}{\lambda^5} \cdot \frac{1}{\exp\left(\frac{hc}{\lambda k_B T}\right) - 1}, \tag{4.1}$$

including the Planck constant h, the speed of light c, and the Boltzmann constant k_B. Figure 4.1 shows the emission spectra for a black body at different temperatures, with special emphasis given to the wavelength range covered by the spectrometer in the HF setup, indicated by the red shaded area (see Sec. 4.2).

The here discussed black body is an idealized object which absorbs and emits radiation at all wavelengths. In contrast, real objects — often referred to as gray bodies — emit less radiation than a black body at the same temperature. The emission spectrum of such a real object $S_{\lambda,\mathrm{real}}(\lambda, T)$, deviates from that of a black body, quantified by the

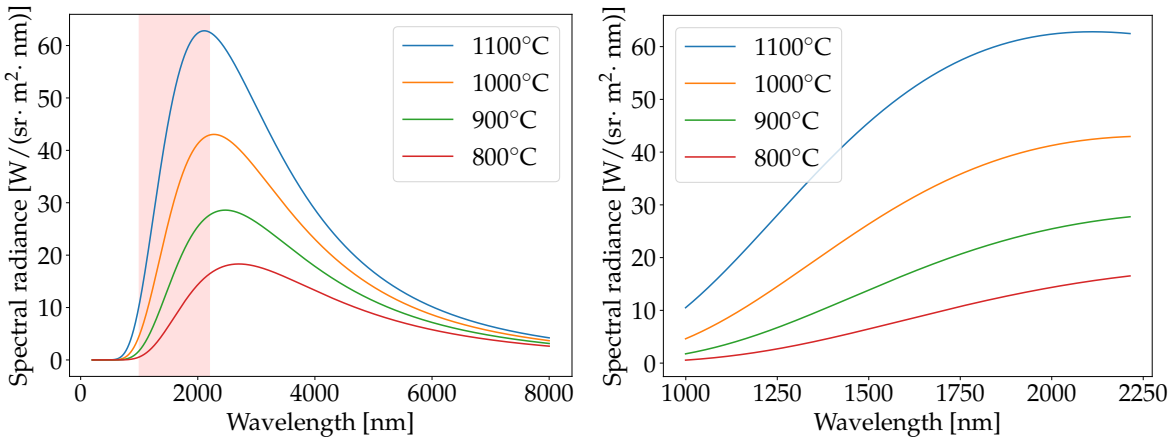

(a) Black body emission spectrum

(b) Emission spectrum in the range of the spectrometer in use for the present study

Figure 4.1.: Panel (a) shows the thermal emission spectra of a black body according to Planck's law for different temperatures. The red shaded area indicates the wavelength range covered by the spectrometer used in the course of this thesis, shown in greater detail in panel (b).

emissivity ε

$$\varepsilon = \frac{S_{\lambda,\mathrm{real}}(\lambda, T)}{S_{\lambda,\mathrm{BB}}(\lambda, T)}, \tag{4.2}$$

which depends on the object's chemical composition and surface topography [135]. It therefore needs to be reevaluated for a given object. Typically, the emissivity for gold is low, with values as low as 0.062 going up to 0.633 [136]. It needs to be considered and if necessary measured when performing a non-contact temperature measurement [137].

4.2. Heating setup

The target heating setup in the HF cave consists of two main components: the heating laser and the target inspection by the microscope, including a fiber leading to the spectrometer, as shown in the schematic layout of Fig. 4.2. The heating laser Opus 532 is a cw laser from Novanta (originally Laser Quantum) [138] emitting at 532 nm. It features an adjustable output power up to 3 W and can be remote controlled. The heating laser is positioned on top of the vacuum chamber in air with two bandpass filters centered around 532 nm with a FWHM of 4 nm positioned right in front of it. They are installed to protect the laser from any light emitted during the interaction of the ATLAS-3000 pulse with the target, so-called back reflections, which can propagate towards the laser

and damage it [15]. An adjustable beam expander allows to change the spot size on the target. Its setting was optimized for the best thermal output of the heated target [132]. The beam is then focused by a lens and via steering mirrors onto the target's front side, hereby transitioning from air into the vacuum chamber through a glass window.

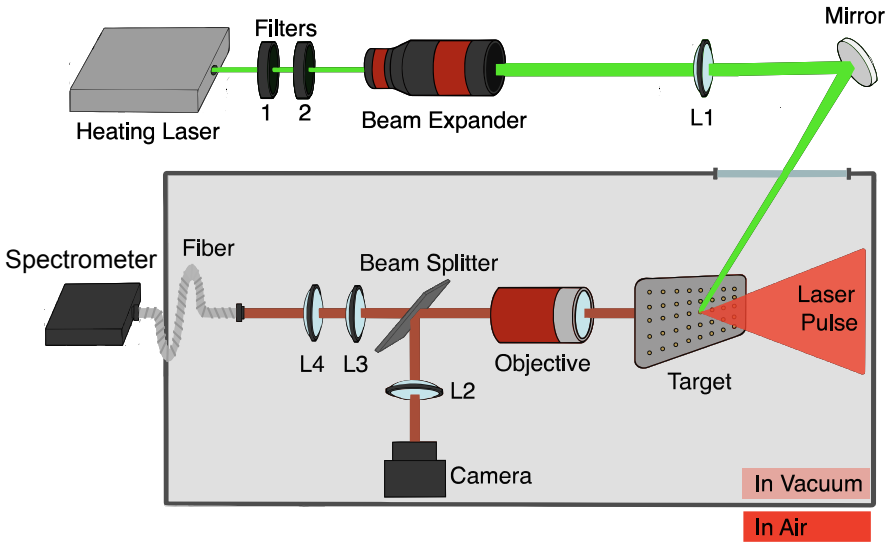

Figure 4.2.: Layout of the target heating and cleaning system at the HF beamline: A cw emitting heating laser is positioned on top of the vacuum chamber. Two bandpass filters directly in front of the laser head protect it from light emitted during the interaction of the ATLAS-3000 pulse with the target. A beam expander is used to adjust the spot size on the target. The beam is then focused by a lens and guided onto the target front side by mirrors, hereby transitioning from air into the vacuum chamber. Simultaneously, the target can be inspected from its backside by a microscope. Two cameras with a three times and 20-times magnification are used to inspect the ATLAS-3000 pulse far field and the targets. In addition, the microscope is also used to couple the near infrared (NIR) spectrum emitted by a heated target into a fiber which guides the radiation to a NIR spectrometer, again positioned in air (Figure adapted from [132]).

Simoultaneously to the heating, the target can be inspected from the backside using the downstream microscope, already mentioned in Sec. 3.2. Light is collimated by an objective with a 20-times magnification (Mitutoyo MY20X-824B [139]). A dichroic beam splitter reflects light in the visible range towards two cameras with three times and 20-times magnification, respectively, which are used to inspect the ATLAS-3000 pulse farfield and the target. Light in the infrared regime is transmitted through the

beamsplitter and via two lenses coupled into a fiber. This leads to the near infrared (NIR) spectrometer, again situated outside of the vacuum chamber in air. The used spectrometer is an NIRQuest512-2.2 from Ocean Insight [140], covering a wavelength range from 900 to 2200 nm over 512 pixels, which results in a binning of 2.54 nm/pixel. The optical resolution is ≈ 5 nm with a 25 µm slit (FWHM).

The integration using the beamsplitter in the microscope allows to measure the thermal spectrum emitted by the heated target while at the same time visually inspecting the target. Thanks to this, any damage of the foil due to overheating can be detected. This is especially important, since the melting temperature of gold at 1064 °C [141] can easily be attained using the heating laser. Damage of the foil below this temperature due to local hotspots is possible as well.

4.3. Calibration and temperature retrieval

By the interaction of electromagnetic waves with matter, the initial properties of the wave can be changed. For example, the spectrum of reflected or transmitted light will be different than the spectrum of the radiating source. Therefore, every optical component between the heated target and the spectrometer will alter the detected spectrum. In order to retrieve the original spectrum, the setup needs to be calibrated, a process that needs to be repeated after every change to the optical path of the light between the heated target and the spectrometer.

For this, a light source with a known spectrum is placed at the usual target position and referred to as *reference spectrum*. From the now measured spectrum by the spectrometer, the so-called *calibration vector* can be deduced via

$$\text{Calibration Vector} = \frac{\text{Reference Spectrum}}{\text{Measured Spectrum}}. \tag{4.3}$$

With this, the influence of optical components in the optical path for future measurements can be corrected via

$$\text{Calibrated Spectrum} = \frac{\text{Measured Spectrum}}{\text{Calibration Vector}}. \tag{4.4}$$

It is important that the spectrometer settings used for the calibration vector acquisition are kept constant for all future measurements.

Figure 4.3 shows a measured spectrum for a 400 nm gold foil, heated with a heating laser output power of 1200 mW plotted in blue. This spectrum, corrected by the calibration

vector, is shown in orange, now showing a similar behaviour like the spectra plotted in Fig. 4.1. Both spectra feature peaks at 1064 nm, 1596 nm and 2128 nm. They originate from the heating laser coupling into the fiber, which could not be improved due to geometrical restrictions. They can, therefore, not be compensated by the calibration vector, but are numerically excluded from the routine determining the target temperature.

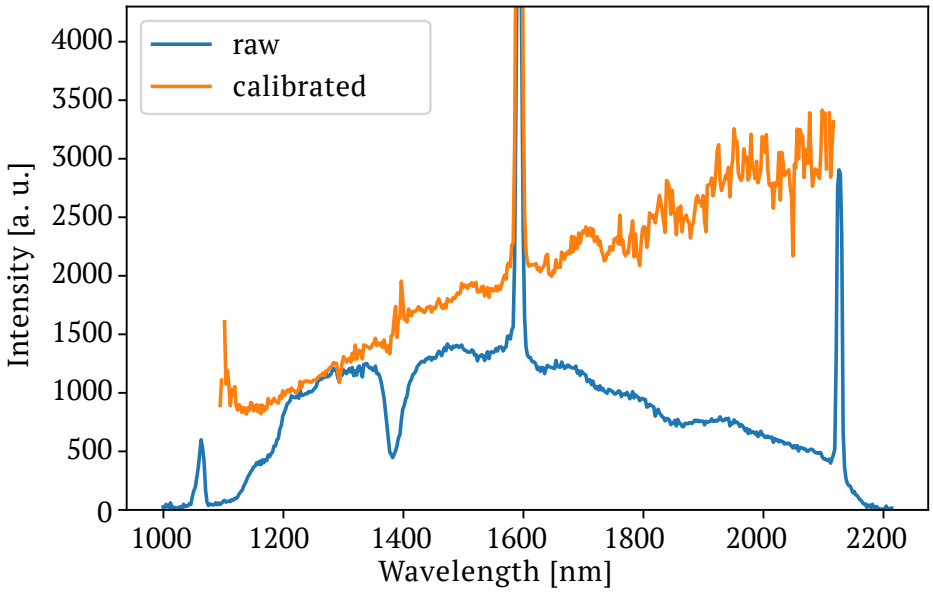

Figure 4.3.: The spectrum emitted by the heated target is different to the one measured by the spectrometer because of the optical components in the beam path. To compensate for this, a calibration vector is calculated. This plot shows the difference of the spectrum with (orange) and without (blue) correction with the calibration vector.

In a last step, Eq. (4.1) is fitted to the spectral data via

$$S_{\mathrm{fit},\lambda}(a, T, b) = \mathbf{a} \cdot S_{\lambda,\mathrm{BB}}(\lambda, \mathbf{T}) + \mathbf{b}, \tag{4.5}$$

where $\mathbf{a}$ is a scaling factor, accounting for the emissivity of gold and the unknown absolute solid angle of the detection system and $\mathbf{b}$ is a constant offset. From this, the temperature $\mathbf{T}$ of the target can be determined. This is exemplary shown in Fig. 4.4 for the target discussed below, resulting in a temperature of 1029.85 °C.

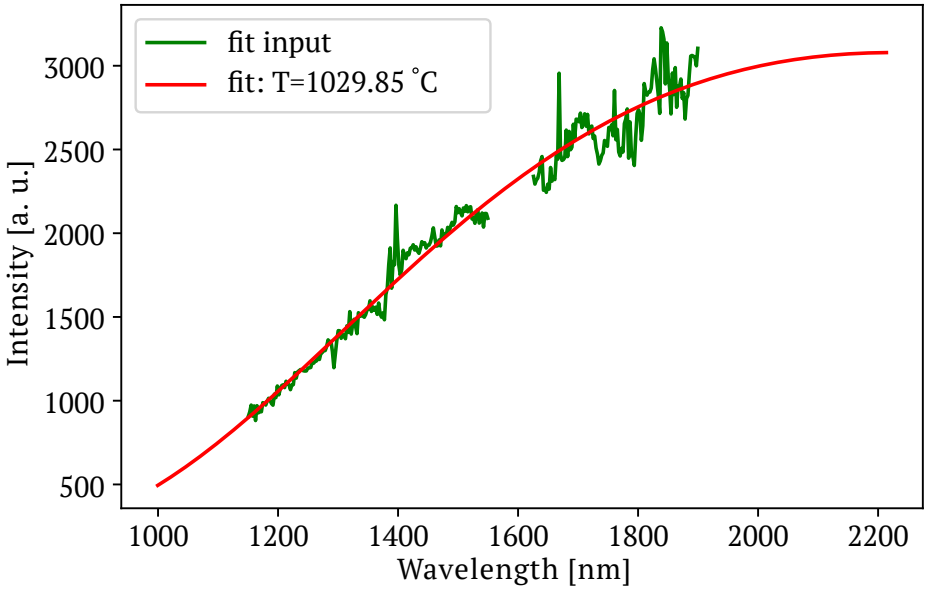

Figure 4.4.: The calibrated spectrum shown in green is fitted by Planck's radiation law, as shown in Eq. (4.5), resulting in a temperature of 1029.85 °C.

4.4. Results of the experimental campaign

The experimental campaign investigating the effect of heating on the acceleration of gold ions at CALA was twofold. The setup measuring the target temperature is part of the downstream microscope, which needs to be removed during shots with the ATLAS-3000. Therefore, the correlation between heating laser output power and target temperature as well as the repeatability had to be investigated in a dedicated study, which will be presented first. In a second step, the influence of target heating on the gold ion acceleration by ATLAS-3000 was investigated.

4.4.1. Determination of target temperature

All experiments were conducted in vacuum, in contrast to a first master thesis investigating heating in a separate laboratory setup outside the chamber in air [131]. For the heating study, the temperature for different output powers for three target thicknesses, 200 nm, 400 nm and 500 nm, was investigated, as shown in Fig. 4.5. For each target thickness, the measurement was repeated for several targets. The trends of temperature changes with heating laser output power are similar for every thickness and shifted to higher output power for thicker targets. The temperature rises steeply until the foils start to break, indicated by the dashed vertical lines in Fig. 4.5. After this, the temperature stagnates.

For targets with the same thickness, the breaking occurs at a characteristic temperature, summarized in Tab. 4.1. With these values it is possible to determine a safe heating laser output power used as a set point during experiments using the ATLAS-3000 laser pulse. It is chosen as a trade-off between a sufficiently high target temperature and any damages caused to the foil.

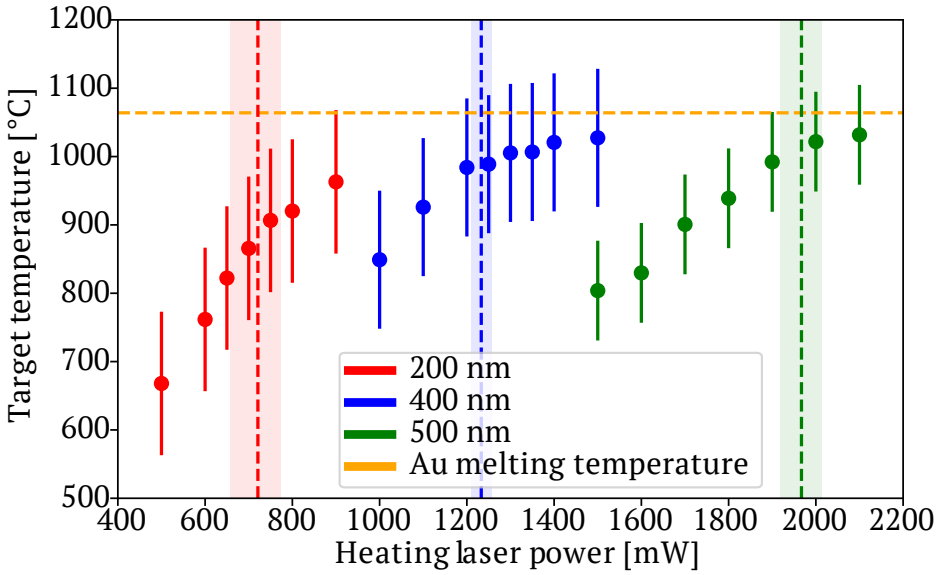

Figure 4.5.: The target temperatures for three target thicknesses at different heating laser output powers were determined. For each thickness, multiple targets were heated in order to investigate the repeatability. The dashed vertical lines for each thickness indicate the average output power where the targets started breaking, with the shaded area indicating the standard deviation. The dashed horizontal line indicates the melting temperature of gold at 1064 °C. Plot adapted from Ref. [132].

Table 4.1.: Mean values of the heating laser output power $\bar{P}_{\mathrm{break}}$ and related standard deviations $\sigma_{\mathrm{P,break}}$ for each target thickness, where cracks in the foil start to form, for target thicknesses of 200 nm, 400 nm and 500 nm.

Target Thickness [nm]	$\bar{P}_{\mathrm{break}}$ [mW]	$\sigma_{\mathrm{P,break}}$ [mW]
200	721	53
400	1233	24
500	1967	48

4.4.2. Influence of target heating on the acceleration of gold ions

For the evaluation of the effect that the heating of targets has on the efficiency of the acceleration of gold ions, two diagnostic tools are discussed: the Lanex screens in combination with an sCMOS camera, which will be covered in detail in Chap. 5, and CR-39 track detectors. The setup using the Lanex is mostly sensitive to carbon ions and protons, while the CR-39 track detectors cover the detection of light and gold ions.

Figures 4.6 and 4.7 each show Lanex images of two consecutive shots on gold targets, with the first shot being on an unheated and the second one on a heated target. For Fig. 4.6, the ATLAS-3000 pulse was shot on a 300 nm thick gold foil. The first shot, shown in Fig. 4.6(a), is on an unheated foil and only a faint trace, overlapping with the one simulated for C^{6+} is visible, with the most energetic ions being at ≈ 210 mm in the direction of the magnetic deflection, corresponding to a maximum energy of 2.6 MeV/u. For the next shot, a target hole on the same holder was heated with 550 mW for 25 to 30 s, displayed in Fig. 4.6(b). The ion trace overlapping with the simulated trace of C^{6+} is much stronger, a result of more particles being accelerated, and reaches higher cutoff energies of up to 4.5 MeV/u.

Figure 4.7 displays a very similar behavior for shots on 400 nm thick gold targets. For the shot on an unheated foil in Fig. 4.7(a), a faint proton signal with a cutoff energy at 3.4 MeV as well as a light ion signal overlapping with the trace of C^{6+} reaching a cutoff energy of 2.6 MeV/u is visible. For the next shot, the target was heated with 600 mW. Again, an intense trace from ions overlapping with the simulated traces of C^{6+} and C^{5+} is visible, reaching up to 3 MeV/u, while no trace from protons is visible.

For the shots on CR-39, 400 nm thick gold targets were used. For the shots on heated foils, the output power of the heating laser was set to 1100 mW, which for this experiment can be correlated to a target temperature of 970 °C. The raw data from the first shot after gating on a heated target is shown in Fig. 4.8, with a superposition of the contributions from light and heavy ions. For the light particles, individual traces are visible, which can be attributed to C^{5+} and C^{4+} as well as O^{7+} and O^{6+}. For both C^{6+} and O^{8+} it holds that m/q=2, so these particles experience an identical deflection onto the same trace and cannot be distinguished by the spectrometer.

On the front side of the CR-39, the position of protons within the energy range that is detectable, i.e. below 3 MeV, is outside the active area of the detector in this setup and are therefore not indicated here. Figure 4.9 shows the CR-39 track detector raw data after applying gating conditions to suppress the background as described in Sec. 3.3.1 from additional shots #2-5 (also with thicknesses of 300 nm). Data from shots #2 and

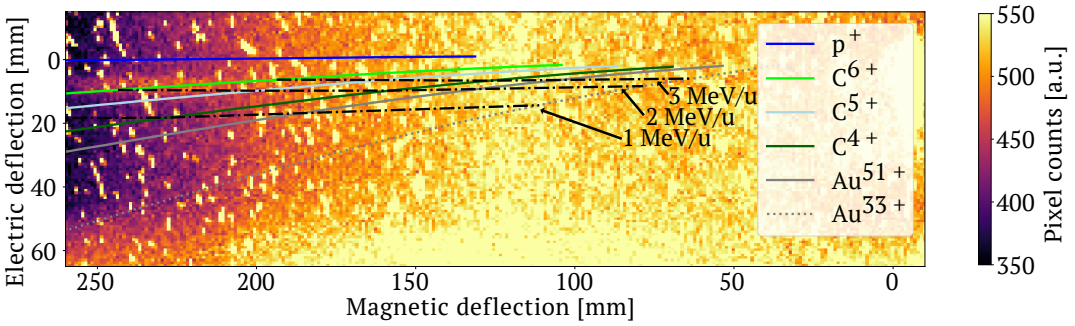

(a) Shot #22 on unheated gold foil

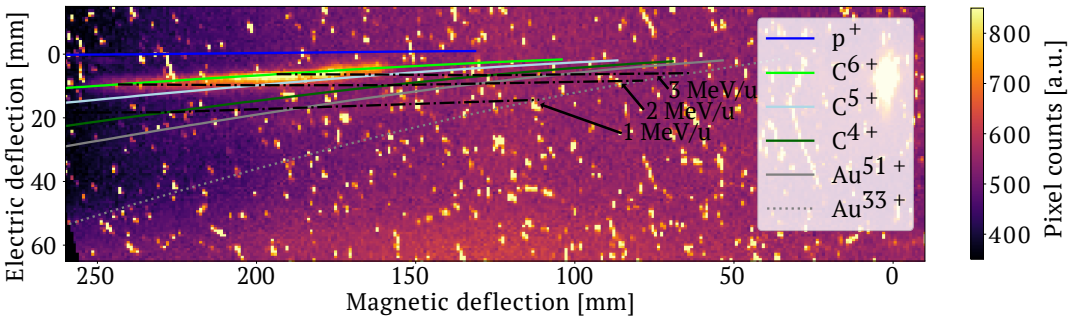

(b) Shot #23 on heated gold foil

Figure 4.6.: Images in false color of laser-accelerated ions detected behind a TPS using a Lanex scintillation screen in combination with an sCMOS camera. For the shot on a 300 nm thick, unheated gold foil shown in panel (a), a faint carbon trace (C^{6+}) is visible, reaching energies of up to about 2.6 MeV/u. For the next shot on a 300 nm thick gold foil, heated with 550 mW, the carbon signature is much stronger, reaching up to 4.5 MeV/u. Note the different color scales.

#3 stem from heated targets, whereas shots #4 and #5 were directed onto unheated targets.

The shots on the CR-39 track detectors agree with the differential response of the acceleration of ions to heating already shown by the Lanex screen images. No significant signal of gold ions is visible for unheated shots and less light ions are accelerated. The highest energy for a light ion accelerated from a shot onto an unheated target was reached for shot #5 for O^{6+} ions with up to 1.5 MeV/u. For shots on heated foils, gold ions are accelerated with cutoff energies reaching up to 2.5 MeV/u, and O^{6+} ions reaching up to 2.4 MeV/u, while 3.25 MeV/u are reached for C^{6+} ions, with a more detailed analysis of the spectra following in Chap. 6. In addition to the front side, also the back side of the CR-39 plates were scanned. While no pits were detected for the heated shots, for

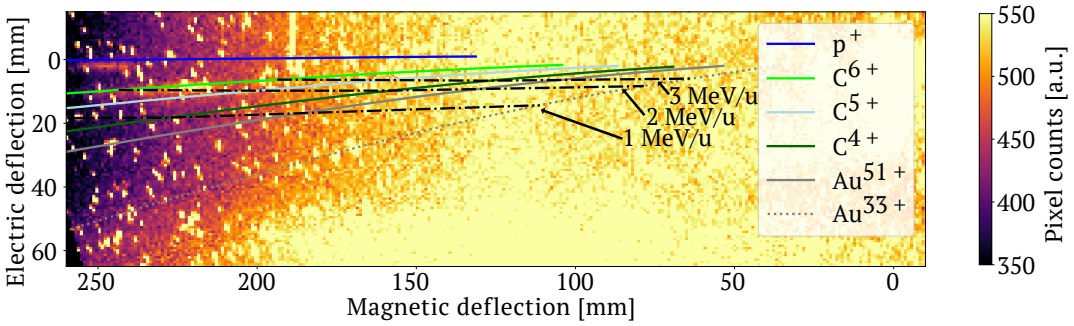

(a) Shot #86 on a unheated 400 nm gold foil

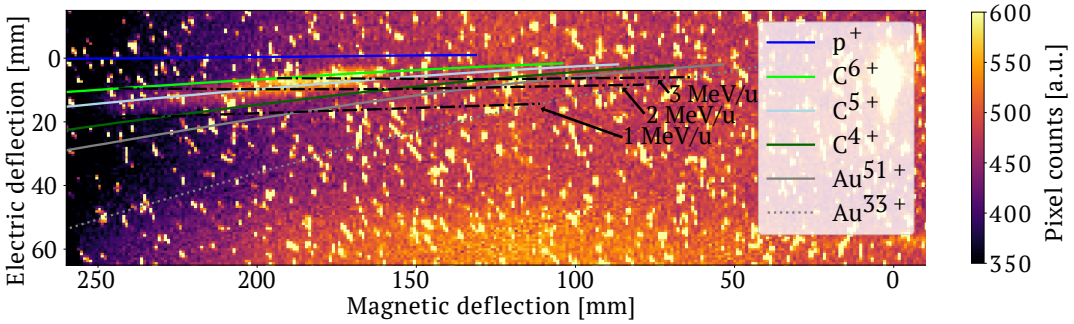

(b) Shot #87 on a heated 400 nm gold foil

Figure 4.7.: Top: Image of Lanex screen for a laser shot on a 400 nm thick, unheated gold foil. A faint proton and carbon trace are visible, with carbon ions reaching energies of up to 2.6 MeV/u. Bottom: Laser shot on a 400 nm thick gold foil, heated with 600 mW. No proton signal is visible and the carbon signature (C^{6+}, C^{5+}) is much stronger, reaching up to 3 MeV/u.

the unheated shots signals associated with the location of protons in the range of 8 to 9 MeV was observed. This indicates that protons with energies of at least 8 to 9 MeV were accelerated, while for heated targets, proton energies remained below these values. Protons were either quantitatively evaporated from the gold foil surface or their energies stayed well below the cutoff energy reached with unheated targets.

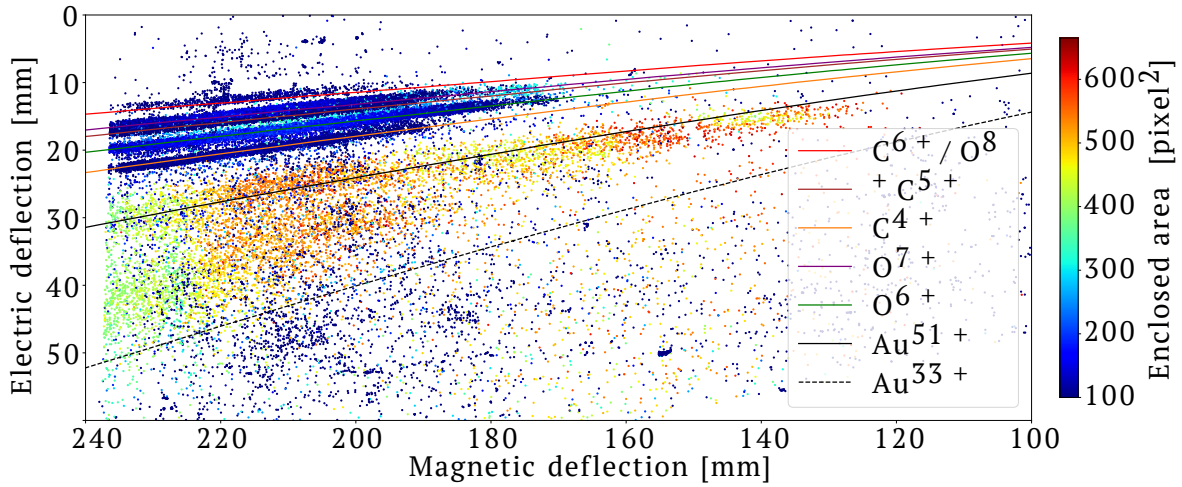

Figure 4.8.: Shot #1 on a heated target. CR-39 track detector raw data after gating on the conditions as described in Sec. 3.3.1 to suppress background signals.

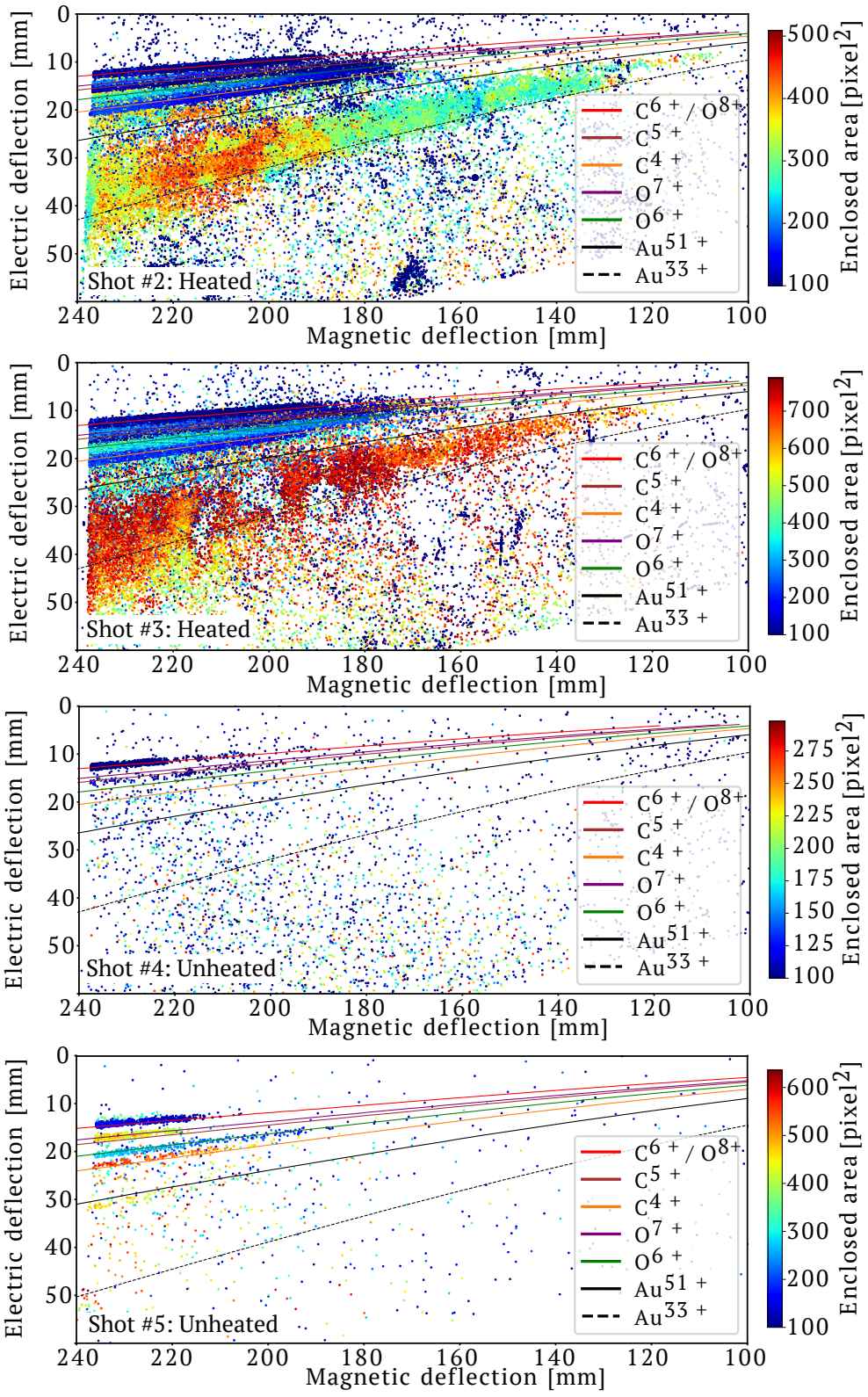

Figure 4.9.: CR-39 track detector raw data after gating on ion signal as described in Sec. 3.3.1 to suppress background signals for two heated and two unheated shots on 400 nm thick gold foils. For the heated shots, the output power of the heating laser was set to 1100 mW, corresponding to 970 °C.

5. Online detection of heavy ions accelerated by lasers

Over the past years the repetition rate of laser-ion acceleration experiments has significantly increased from a few shots per day to repetition rates reaching up to 1 Hz. To take advantage of this high repetition rate, a fast feedback about the ion performance is desirable, in order to adjust the current experimental configuration, aiming at further improving the performance. For this, online detection is necessary, replacing slow offline detectors like CR-39 nuclear track detectors or image plates.

Requirements for online detectors include resistance to EMP, the possibility to detect the ions in vacuum and their radiation hardness, which needs to be demonstrated especially for heavy ions. Options for such detectors include scintillators to measure the lateral ion bunch profile [112], or advanced integration to retrieve the proton spectrum [142]. Time-of-flight detection using diamond detectors currently gives the best energy resolution [143], while scintillators offer a cheaper alternative and can be implemented with less degradation of the ion beam quality [**?**]. Lanex scintillating screens in combination with degraders have been used to assess cutoff energies [53], with calibrations to retrieve absolute particle numbers being available [117]. For dosimetry, ionization chambers are commonly used, while high dose rates can lead to saturation [144]. An alternative is using integrating current transformers [145]. Other options include direct detection via CMOS detectors, often in combination with magnetic spectrometers [82] or ionoacustic detection methods [146].

However, a lot of these techniques focus on the detection of protons. For analyzing the energy spectra of multiple ion species with various charge states produced by laser-plasma accelerators, detection using a Thomson Parabola Spectrometer (TPS) remains the preferred method. This approach requires high sensitivity to low ion counts in order to accurately capture the high-energy cutoff of the spectra. At the same time, it must withstand significantly higher particle fluxes (which are often two to three orders of magnitude greater) at lower energies.

Microchannel Plate Detectors (MCPs) are a commonly used diagnostic tools in combination with a TPS for online diagnostic [147]. However, MCPs have strict requirements

on vacuum quality ($\lesssim 10^{-5}$ to 10^{-6} mbar), the high voltage (in the kV-range) that is applied makes them susceptible to EMP and their cost quickly increases with the size of their active area. In addition, they lack a proportional response to the number of ions [148]. Therefore, in the scope of this thesis, two methods for online detection of heavy-ions in combination with a TPS were investigated. The first option includes an EJ-200 scintillator directly attached to a large area CMOS detector and will be presented first. Following, the experimental data using a Lanex screen in combination with an sCMOS camera positioned outside the vacuum chamber will be presented.

5.1. Detection using a CMOS detector

For these experiments, a pixelated CMOS detector in combination with a scintillator, as described in Sec. 3.3.2, was used. The setup was placed at a distance of $d_B = 61.5$ cm to the end of the TPS magnet inside a light-tight housing, made from black, anodized aluminum foil of 50 µm thickness. This was ensuring that no stray light from the laser and the laser-target interaction contaminated the acquired image. The pinhole of the TPS was placed on a motorized stage, therefore allowing a swift change between pinholes with a diameter of 500 µm and a diameter of 1 mm, respectively. This way, if the signal-to-noise ratio was sufficient, the smaller pinhole could be employed, increasing the resolution. Due to connection issues, the TPS electrodes could not be used to their full potential for this experiment, only allowing for an electric field of 27 kV/cm (instead of 30 kV/cm).

To reduce the accumulated dark current, the detector was triggered via a double pulse. The exposure time was set to 20 ms, with a first trigger arriving −200 ms before the main laser pulse and a second trigger at −10 ms by using a Stanford delay generator (DG645) triggered by the central trigger of our laser facility. This way, every pixel gets read out and reset right before exposure to the accelerated ions and the influence of long waiting times between laser shots and the thus varying amount of dark current is reduced. Without this measure, a successful background subtraction cannot be realized and the ion signal is not resolved.

Since the detector is operated in vacuum, cooling via convection is suppressed compared to operation at air. When operated over longer periods of time, the detector heats up, leading to an increased dark current (see Eq. (3.7)). Therefore, in regular intervals new background images were acquired throughout the experiment.

Compared to the CR-39 track detector, the CMOS detector offers a smaller active area, not allowing to capture the proton and gold ion high energy cutoff position simultaneously.

It was therefore positioned in a way that protons with a minimum energy of 7 MeV and Au^{55+} ions with a maximum energy of 1.8 MeV/u could be detected.

In a first run, 500 nm thick formvar targets were used in combination with a 500 µm diameter pinhole in front of the TPS. From these targets predominantly protons are accelerated, with some contribution of carbon ions. The acquired images were background subtracted and overlayed with particle traces calculated via particle tracking, taking into account the reduced electric field of the electrodes for this experiment. An exemplary image is shown in Fig. 5.1. The image is cropped in the electric deflection dimension, while showing the full range in the magnetic deflection dimension.

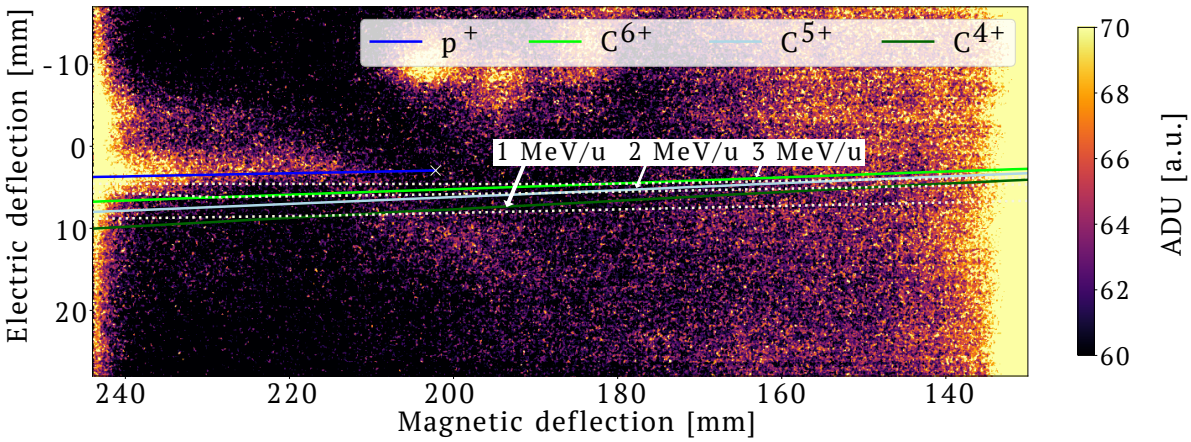

Figure 5.1.: CMOS image of shot #1 on a 500 µm thick formvar target. Only a faint signal from the accelerated protons is visible, indicated by the blue curve calculated via particle tracking.

The image shows only one trace at a low signal-to-noise level, which is attributed to protons, with no signal from carbon ions. However, the width of the proton trace already indicates that even for light ions the individual charge states will not be resolvable with this detector. The main source of scattering is the scintillator. Using a thinner scintillator as well as improving the optical coupling to the Fiber Optical Plate (FOP) can be successful steps to improve the spatial resolution for future experiments. The image also shows on-shot background on the edges in the magnetic deflection dimension, coming from increased leakage current, as well as some additional noise.

As previously laid out, an absolute calibration of particle number to ADU is not yet available for this setup. For this, the deposited energy $\mathrm{d}E/\mathrm{d}x$ for for all species for a given incident energy would need to be translated to the number of emitted photons by the scintillator and then be convoluted with the quantum efficiency of the detector for the wavelength the scintillator is emitting at. As a consequence, the detection threshold,

i.e. the minimum number of particles necessary to produce a distinguishable signal, is not known. During our experimental campaign, no additional detector (e.g. slotted CR-39 track detector) was available, not allowing for a cross calibration. Therefore, no estimation is available of how well the visible proton cutoff energy represents the real cutoff of the energy spectrum. Further, no spectrum can be extracted from these images. From the resolution available, the highest proton energy was reached for shot #1 with up to 9 MeV, which is lower than what was realized in previous campaigns at the HF setup, where protons with more than 21 MeV were detected.

In a next step, the ATLAS-3000 pulse was shot on 500 nm thick gold targets, heated with 1200 mW for more than 10 s. Note that for this experiment, the relationship between heating laser output power and target temperature plotted in Fig. 4.5 is not valid, as the diameter of the heating laser on the target was changed and no measurement of the target temperature was done for this configuration. Due to the low signal-to-noise ratio, the TPS pinhole diameter was increased to 1 mm. An exemplary image is shown in Fig. 5.2. One broad trace region is visible. Due to the large scattering introduced by the scintillator, it is not possible to distinguish signals produced from gold ions from potential contributions of carbon ions up to a magnetic deflection of ≈ 210 mm.

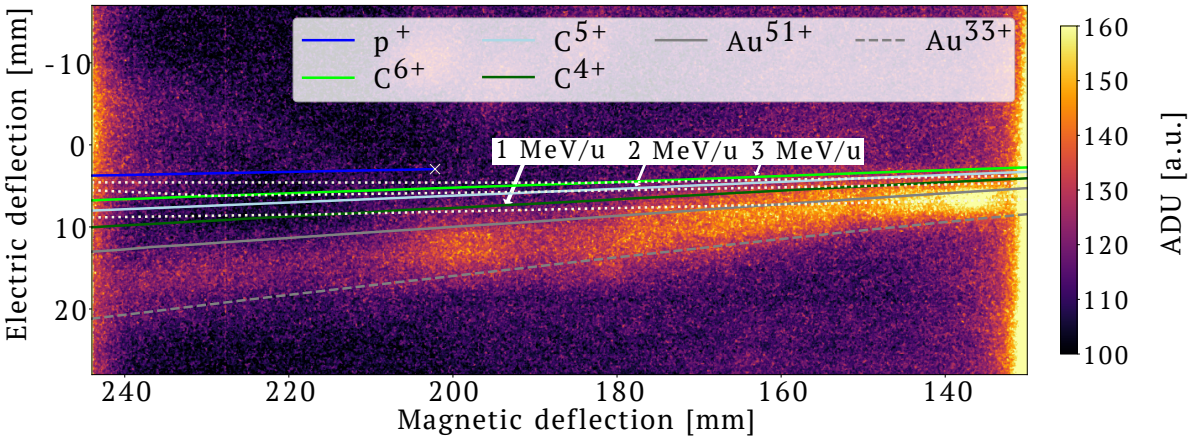

Figure 5.2.: CMOS image from shot #5 on a 500 nm gold target heated with 1200 mW.

Further shots on heated gold targets are displayed in Fig. 5.3 and 5.4. When comparing shots #5 - #7 to shots #8 - #10, the most striking difference is the higher background level for shots #8 - #10. Interestingly, this coincides with a different target configuration during the experiment. For the production of the gold targets, the parting agent was changed from trimethylglycine ($C_5H_{11}NO_2$) to sodium chloride (NaCl). For this beamtime the targets processed with trimethylglycine were mounted in a so-called

sandwich configuration, where an empty target holder is attached to the main holder that carries the gold foil, with the gold foil in-between the holders. This way, after the first full-power shot on this holder, neighboring target holes were significantly less damaged, since a peeling off of the foil from its support was reduced. For target foils produced with NaCl as a parting agent, this construction was not necessary. It is surprising that the otherwise beneficial sandwich target configuration seems to lead to an increase in X-ray radiation, resulting in an increased on-shot background level on the CMOS detector. A possible explanation could be that the additional target holder on the backside of the foil acts as a converter where electrons, accelerated during the laser-target interaction, get converted into X-rays. However, the present data set is very scarce, not allowing for a decisive conclusion.

Due to the low signal-to-noise ratio and on-shot background features, with the present dataset it is difficult to draw any conclusion from the images. For shots #5, #7 and #9, a weak proton signal might be present, which for these shots would correlate with a reduced acceleration of gold ions. Any more detailed analysis is not possible, since no decisive distinction between gold ions and light ions like carbon ions is possible. Very vaguely, the gold ion charge-state distribution seems to be in the same range as for the shots on CR-39, i.e. about Au^{33+} to Au^{51+}.

While the implementation of the detector needs further improvement, a coarse online detection of laser-accelerated gold ions was possible using an EJ-200 scintillator in combination with a large area CMOS detector.

5.2. Detection using a Lanex screen

In a different approach, a Lanex scintillating screen was used in combination with a sCMOS camera, positioned in air, as described in Sec. 3.3.2. For the shots on 31.05.2023, the Cawo Lanex [115] was used. During the other experiments, the DRZ high Lanex [116] was employed. The Lanex screens are available in various sizes. In our experiments they had an active area of $15 \times 25\,\mathrm{cm}^2$. Due to geometric restrictions of the vacuum chamber, the camera could not be positioned with a direct line of sight towards the scintillator. This was mitigated by imaging the Lanex screen via a planar mirror onto the sCMOS. Therefore, the image on the sCMOS sensor was skewed, as shown in Fig. 5.5.

To obtain an unskewed image, first a dewarping routine was established. For this, a quad paper with a grid pitch of 5 mm was placed at the position of the Lanex screen. From the skewed image, the positions of four corners forming a rectangle, also shown in Fig. 5.5

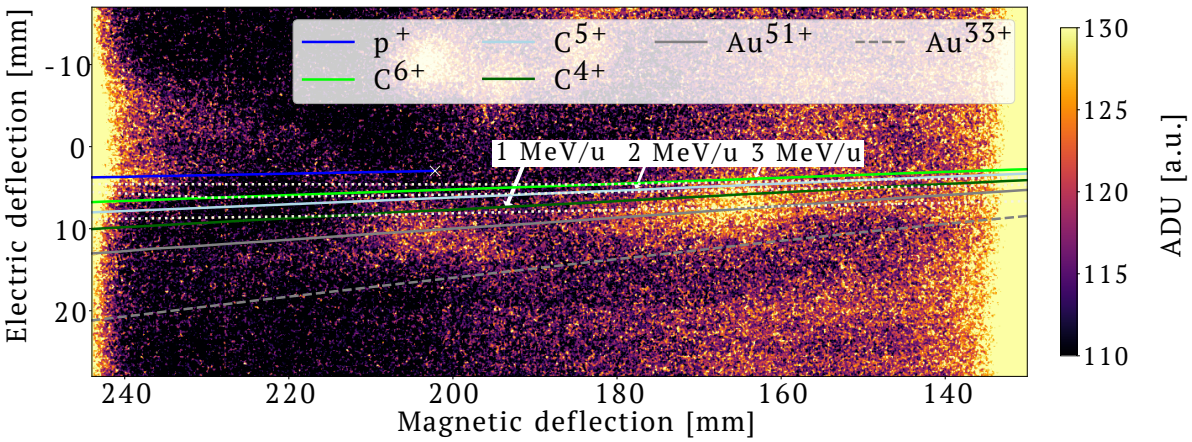

(a) Shot #6

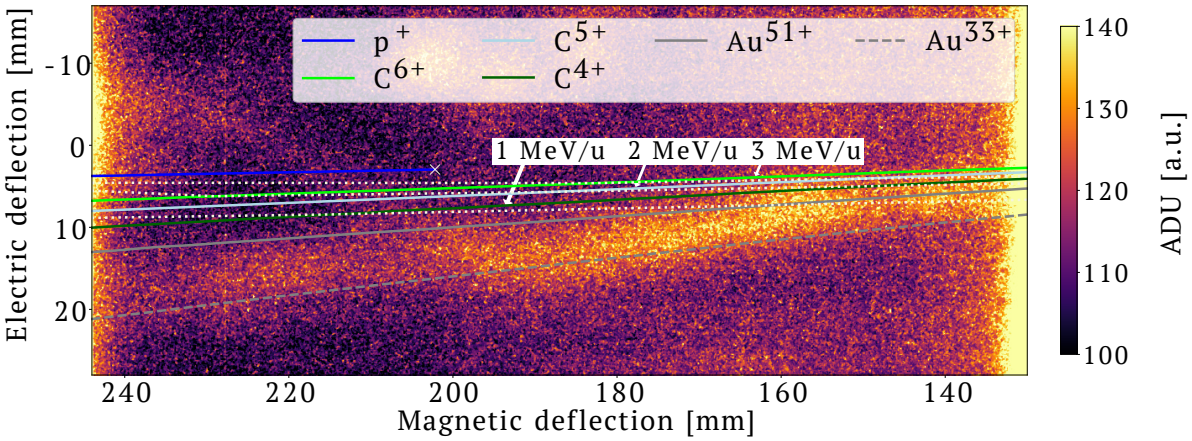

(b) Shot #7

Figure 5.3.: CMOS images of shots #6 and #7 on 500 nm gold targets heated with 1200 mW. The targets were produced with NaCl as parting agent and no sandwich structure was applied for their mounting.

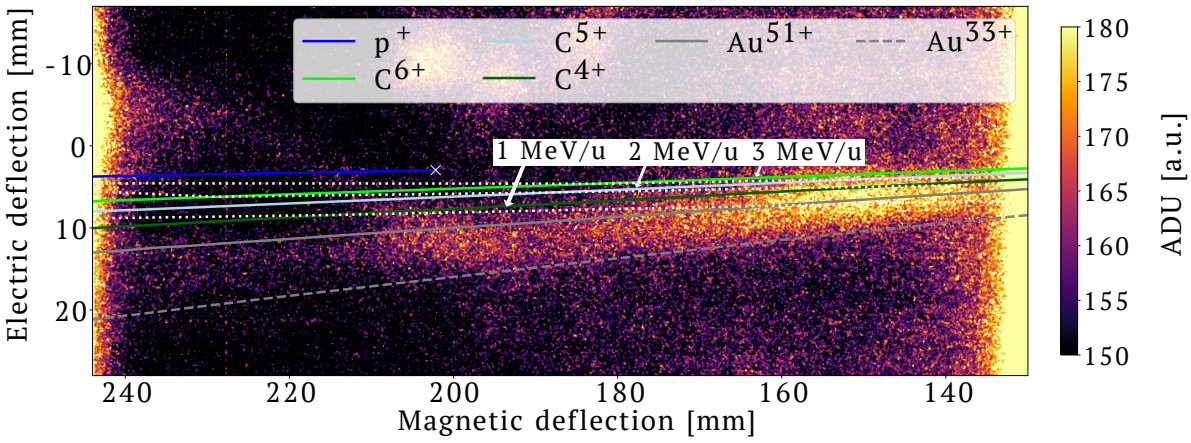

(a) Shot #8

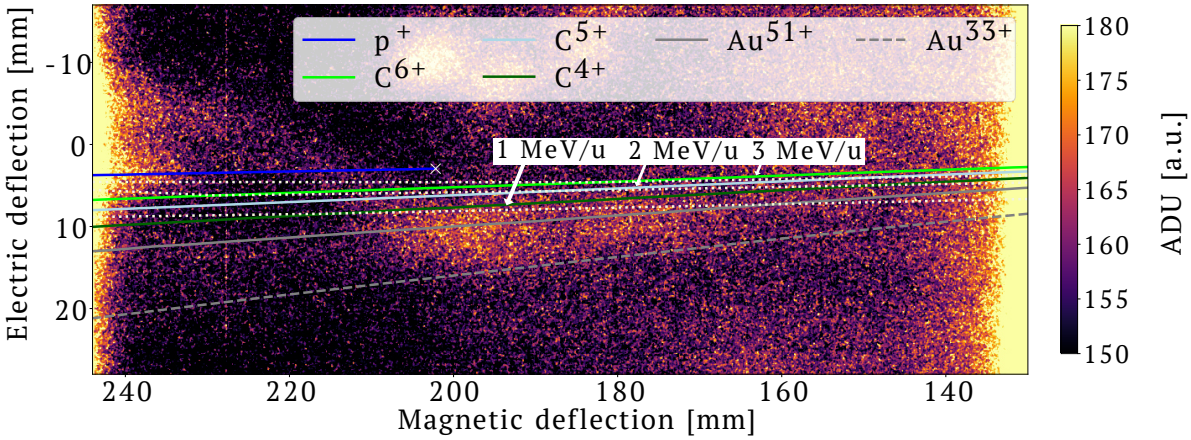

(b) Shot #9

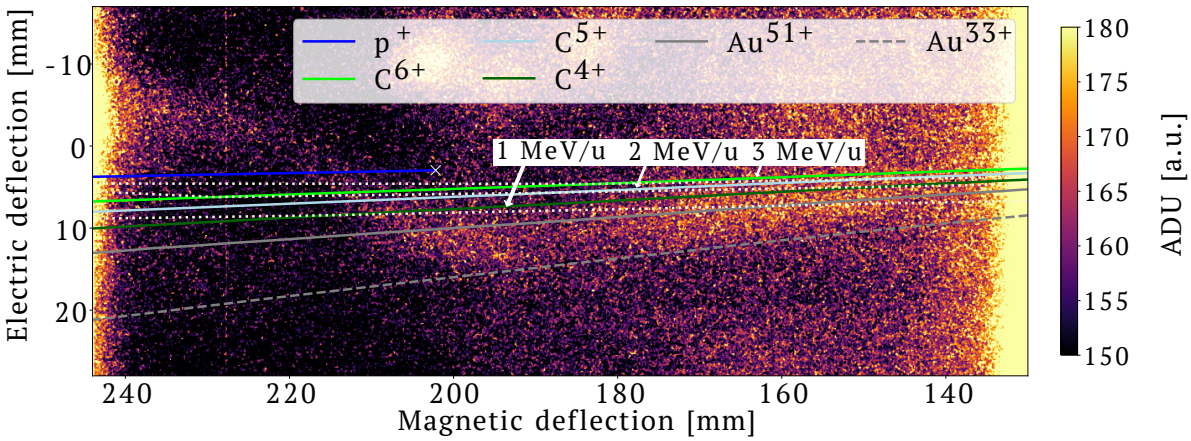

(c) Shot #10

Figure 5.4.: CMOS images of shots #8-#10 on 500 nm gold targets heated with 1200 mW. The targets were manufactured using trimethylglycine as parting agent and mounted in a sandwich configuration.

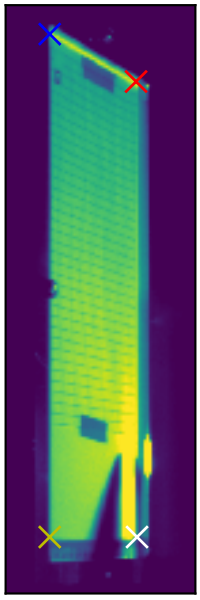

Figure 5.5.: Since the Lanex screen is imaged via a planar mirror under an angle onto the sCMOS camera, the image is skewed. For the dewarping routine, a quad paper with 5 mm grid size is positioned at the position of the Lanex screen. The four crosses define the corners of a rectangle on the real, unskewed object. They lay the basis for a Python routine to dewarp the image for further analysis.

were defined. With these, using the cv2 Python library, a matrix projecting these defined four corners onto a rectangle was calculated using the function *getPerspectiveTransform*. This matrix can then be applied onto the acquired images using the cv2 function *warpPerspective*. The result of this routine, i.e. the dewarped image, is shown in Fig. 5.6.

To further ensure that the routine worked correctly, an enlarged view of Fig. 5.6 is inspected, shown in Fig. 5.7(a). For this, the pixel values along the vertical and horizontal axis are projected, as plotted in Fig. 5.7(b). The black lines of the quad paper with a distance of 5 mm have lower pixel values than the white space in-between, resulting in dips in the projection. The location of the local minima is analyzed by a python routine and indicated by the dots in Fig. 5.7(b). The average distance between the dots being 5 pixels shows the successful dewarping routine and the conversion of 1 pixel being equal to 1 mm.

Every change of the relevant components, i.e. the position of the screen, the mirror and the camera, requires the acquisition of a new calibration image to correctly set the

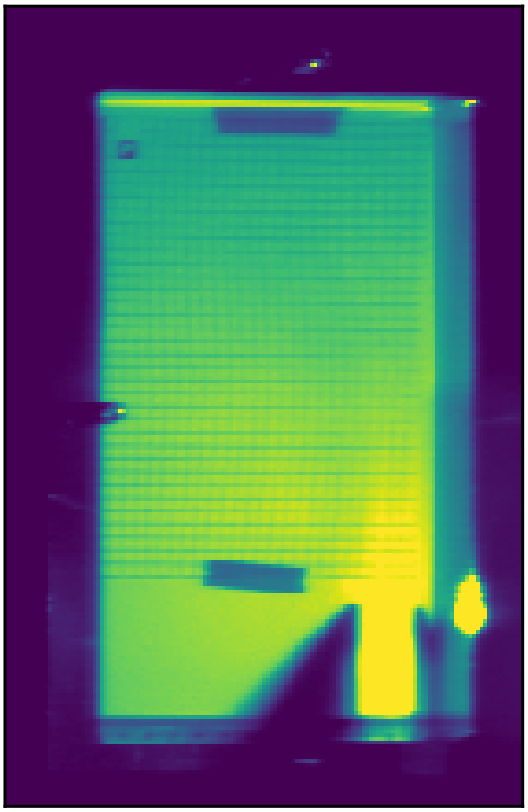

Figure 5.6.: Unskewed image of the quad paper, positioned at the location of the Lanex screen, after it was processed using the dewarping routine.

four corner points defining a rectangle for the dewarping routine.

For full-power laser shots without an interaction with the target, so-called *empty shots*, only a small point is detected on the Lanex screen, as shown in Fig. 5.8, stemming from direct light entering setup via the pinhole in front of the TPS. The image surrounding the Lanex screen is dark, proving the correct installation of the light shield. Two sources of noise become apparent from this image. For one, the image contains speckles of high intensity and varying shape. Since they are present over the whole area of the sCMOS chip, they most likely originate from X-rays directly hitting the chip. Their changing shapes come from different angles of incidence due to the various surfaces inducing scattering between the source and the chip. The second contribution of noise is a general glowing of the Lanex screen, imaged via the mirror onto the sCMOS camera. Attempts to suppress this background were not yet successful. Since the background level from the glowing of the Lanex screen varies in-between shots, the considered pixel values were manually adjusted for every image displayed in this thesis, in an attempt to maximize

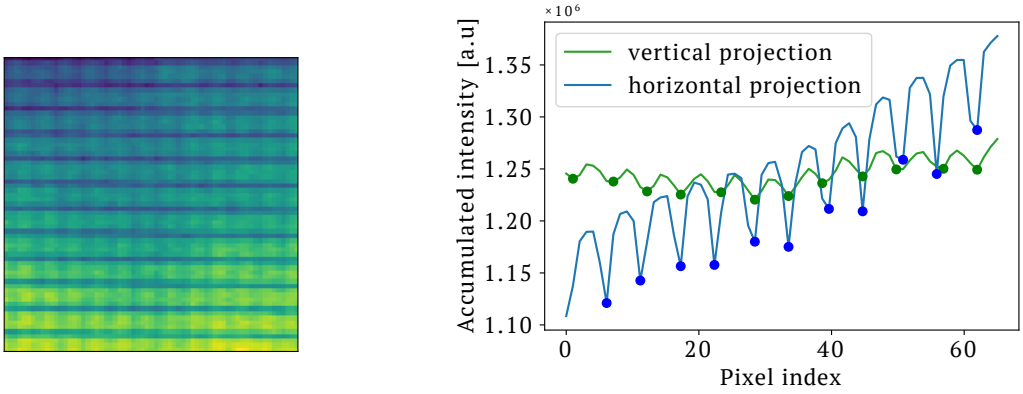

(a) Enlarged view of dewarped image

(b) Projection of pixel values

Figure 5.7.: Panel (a) shows an enlarged view of the quad paper, displayed in Fig. 5.6. To ensure the dewarping routine worked correctly, the projection of pixel values along the horizontal and vertical axis are shown in panel (b). The minima, resulting from the black lines with 5 mm-spacing result in the dips in the projection, indicated by the dots. The average distance between the minima is 5 pixels, showing a successful dewarping routine.

the contrast. A correlation between the background level and other parameters of the interaction was not yet found (compare Chap. 4.2 of Ref. [149]) and will need further investigation.

After successfully dewarping the images of the Lanex screen acquired by the sCMOS camera the traces on the Lanex screen were identified by overlapping them with traces simulated via particle tracking. To improve readability, again only two gold traces representing the upper and lower limit for the expected charge state regime is plotted in the following figures. In first experimental runs, the setup was used in combination with a 1.5 mm diameter pinhole in front of the TPS. First, the correct alignment of the simulated traces was verified from shots on 300 nm thick formvar foils, where protons and carbon ions get accelerated, depicted in Fig. 5.9, using the Cawo Lanex screen. During our experiments the high voltage power supplies of the TPS electrodes were monitored with a camera. If at all, only short and minimal breakdowns (below 1 kV) which recovered quickly, could be observed. The electric field of the TPS is therefore assumed to have stayed constant during our experiments, in contrast to previous experiments [15]. Therefore, no large shifts in the direction of the electric deflection are to be expected.

For the shot displayed in Fig. 5.9(a), only a proton trace is visible with a cutoff position around 150 mm in the direction of the magnetic deflection, corresponding to 19.1 MeV. This energy is close to the proton energy previously measured with a wide

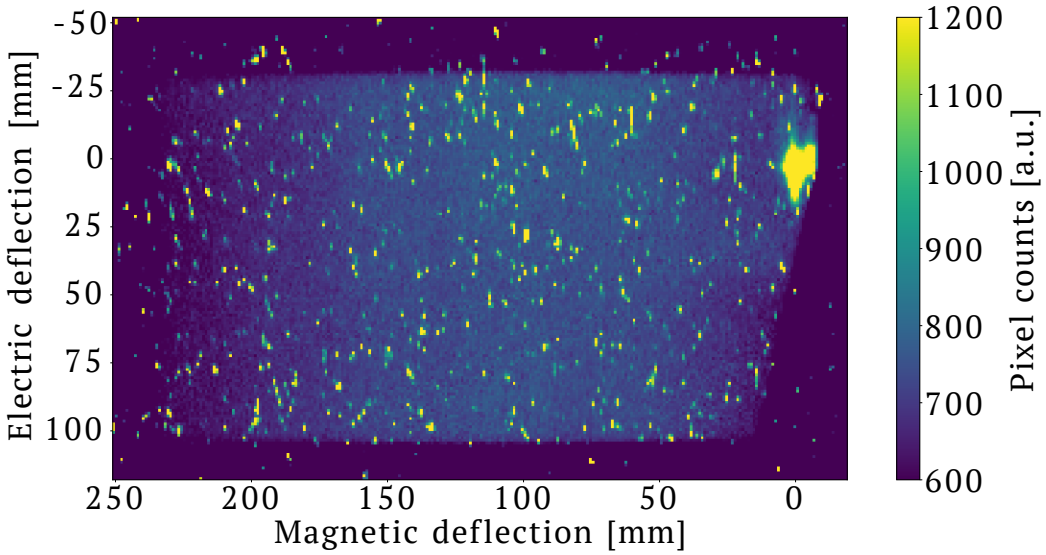

Figure 5.8.: For an *empty shot*, i.e. a laser shot without an interaction with a target, a bright spot is visible, coming from direct light entering the setup through the pinhole in front of the TPS. Bright speckles and a glowing of the screen contribute to the background of the image. Outside of the Lanex screen, the image is dark, proving the successful light shielding of the setup.

angle spectrometer in combination with a CMOS detector at HF, suggesting that the setup is sensitive enough to determine the cutoff energy. The trace is not fading in intensity towards the cutoff energy, as would be expected for a TNSA-like spectrum, an observation that as well was already made in previous measurements, without a clear explanation at hand. The second displayed shot in Fig. 5.9(b) shows a proton trace with less intensity and with a cutoff position around 200 mm in the direction of the magnetic deflection, corresponding to 11.4 MeV. Beneath it a second trace is visible, created by carbon ions. From the overlayed traces it corresponds to C^{5+}, with the cutoff at 220 mm in the direction of the magnetic deflection, corresponding to 1.6 MeV/u. In a next step, heated gold foils were irradiated with the ATLAS-3000 laser pulse, shown in Fig. 5.10.

Both shots do not exhibit a proton trace, but a carbon C^{6+} trace reaching up to higher energies compared to the shots on formvar. This is the result of heating the gold foil, as laid out in the previous chapter, significantly reducing the number of protons being present for acceleration. For Fig. 5.10(b), a clear cutoff of the carbon trace at 170 mm in the direction of the magnetic deflection, corresponding to 4 MeV/u, can be observed. For Fig. 5.10(a), determining a clear cutoff energy is harder, already indicating that the signal-to-noise ratio remains an issue using this detector. Determining the cutoff to be

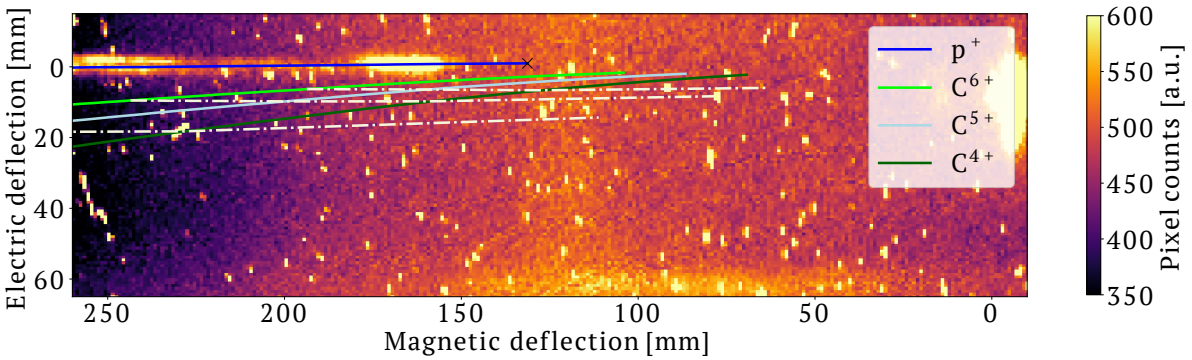

(a) Shot #16 from 31.05.2023 on a 300 nm thick formvar foil

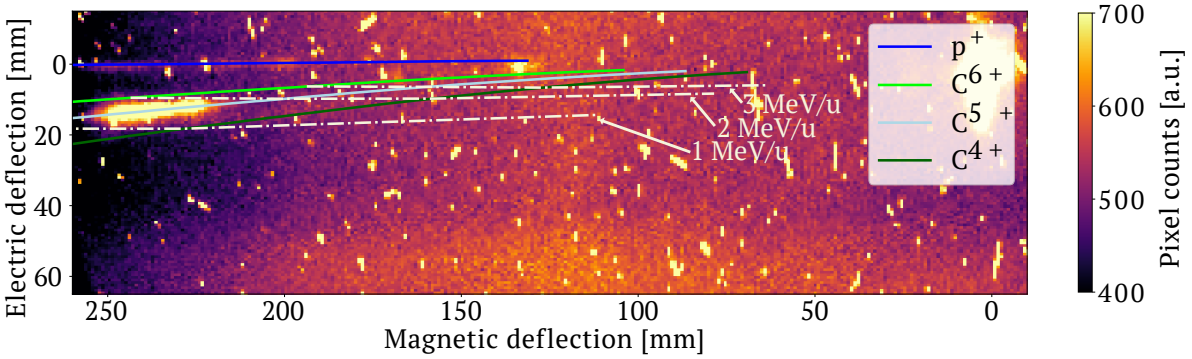

(b) Shot #26 from 31.05.2023 on a 300 nm thick formvar foil

Figure 5.9.: Images using the Cawo Lanex screen from shots on formvar targets (300 nm thick) are used to verify the correct alignment of the traces in the direction of the electric deflection. Measured with an entrance pinhole to the TPS of 1.5 mm.

at 200 mm corresponds to an energy of 2.8 MeV/u. For both shots a faint signal around the trace corresponding to Au^{40+} is visible, while also here a determination of the cutoff position is not possible due to the high background level. For Au^{40+}, ions at 150 mm in the direction of the magnetic deflection have an energy of 0.8 MeV/u.

In a next campaign, the pinhole size in front of the TPS was reduced to 1 mm, in order to increase the resolution of the setup. Reducing the pinhole diameter from 1.5 mm down to 1 mm reduces the number of particles passing into the setup by 44 %. By this the signal level at the proton cutoff position is reduced below the noise level of the detector. When the pinhole diameter was further reduced to 0.5 mm, no signal could be observed for all configurations using a Lanex screen as ion detector.

However, as discussed in Sec. 3.2.2, a larger pinhole diameter decreases the resolution. This especially gains importance when observing gold signals with higher charge states.

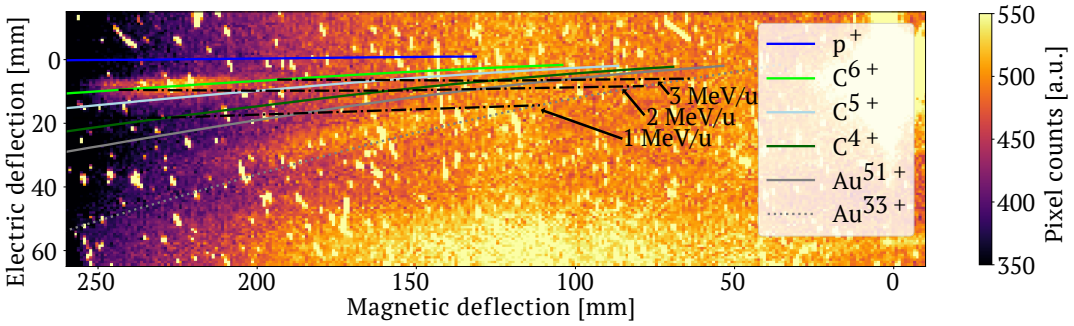

(a) Shot #45 from 31.05.2023 on 500 nm gold foil heated with 1500 mW

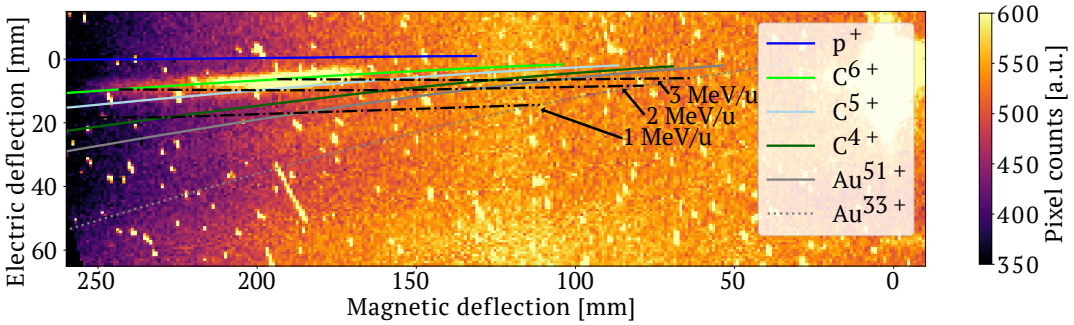

(b) Shot #47 from 31.05.2023 on 400 nm gold foil heated with 1100 mW

Figure 5.10.: Images of Cawo Lanex screen from shots on heated gold foils on 31.05.2023

Fig. 5.11(a) shows an image of the DRZ-high Lanex screen from a shot on a 500 nm thick gold foil heated with 1600 mW, which corresponds to a target temperature of about 820 °C. Fig. 5.11(b) shows a magnified view of the region indicated by the white rectangle in Fig. 5.11(a). Here, for clarity only the calculated traces of C^{4+} and Au^{55+} are shown, together with the calculated trace width derived from the TPS pinhole diameter and projected onto the location of the detector (see Eq. (3.4)), indicated as shaded areas around the sharp trace trajectory. From this plot it becomes apparent that for magnetic deflections of less than ≈ 170 mm the traces of C^{4+} and Au^{55+} ions overlap, so a clear distinction between the two species is not possible in this region.

Figures 5.12 and 5.13 show images of shots on heated gold foils. For Fig. 5.13(b), a gold ion signal with charge states around Au^{40+} is visible (indicated by the orange ellipsis), while for the other images, signal closer to Au^{55+} can be observed. For all shots the signal level is close to the noise level and an energy cutoff can therefore not be determined.

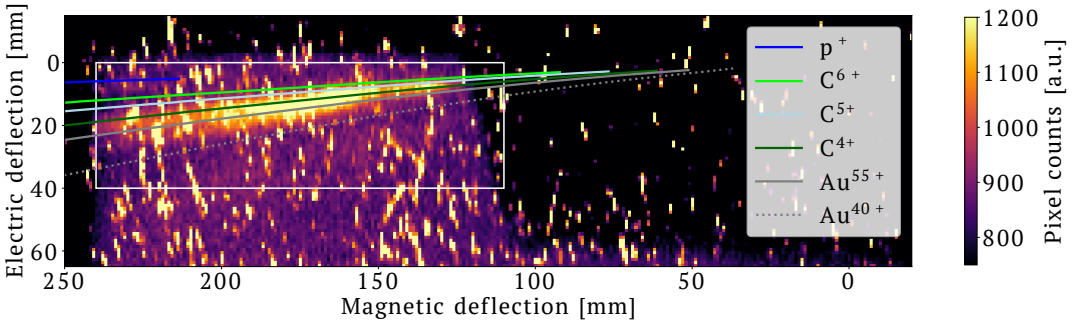

(a) Shot #23 from 19.12.2023 on 500 nm thick gold foil heated with 1600 mW, corresponding to about 820 °C

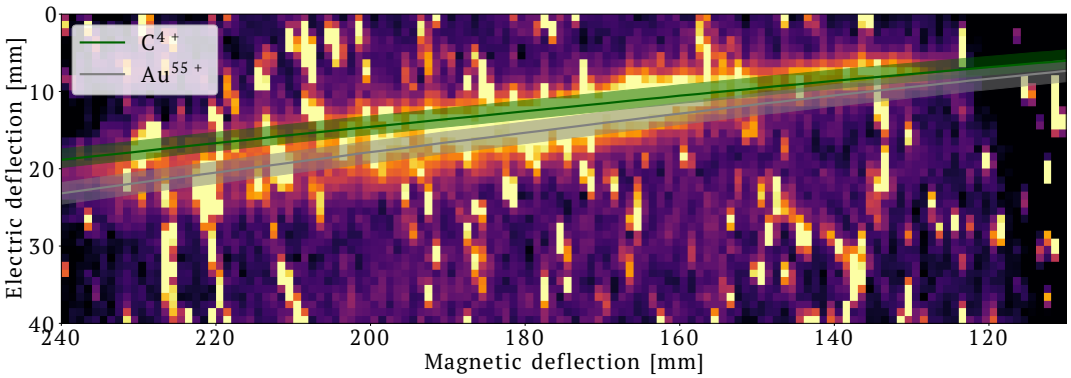

(b) Magnified view of the region indicated by the white rectangle in panel (a), including the projection size of the TPS pinhole at the location of the detector

Figure 5.11.: Panel (a) shows a 'DRZ-high' Lanex screen image from a shot on a 500 nm thick gold foil, heated with 1600 mW. Panel (b) shows a magnified view of the region indicated by the white rectangle in panel (a). The shaded area around the traces indicates the trace width derived from the projection size of the TPS pinhole at the location of the detector.

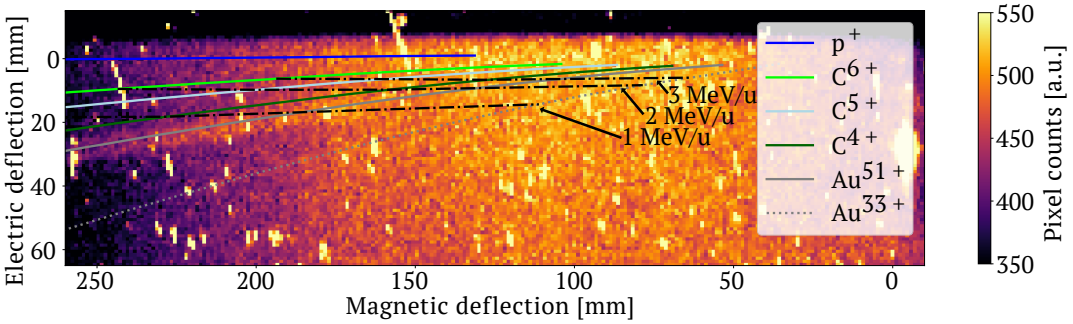

(a) Shot #63 from 17.08.2023 on a 400 nm gold foil heated with 1100 mW

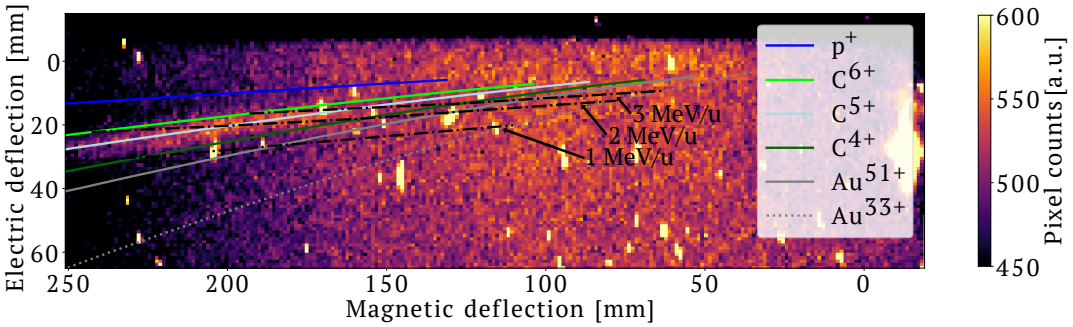

(b) Shot #71 from 17.08.2023 on a 500 nm gold foil heated with 1500 mW

Figure 5.12.: Images of DRZ high from shots on heated gold foils on 17.08.2023

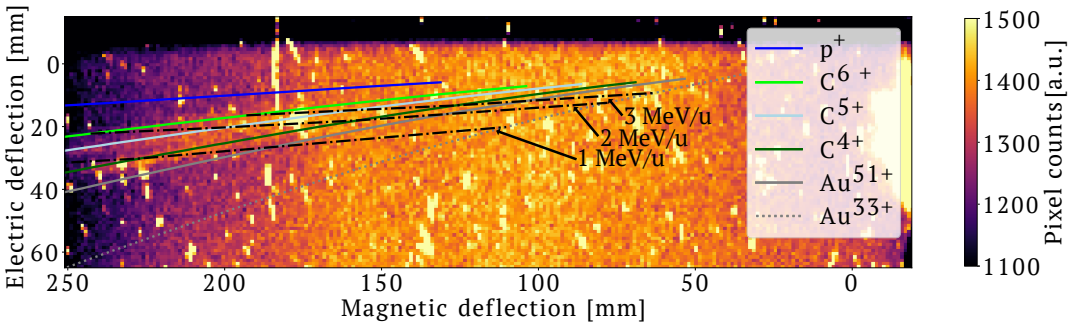

(a) Shot #47 on a 500 nm gold foil heated with 1600 mW

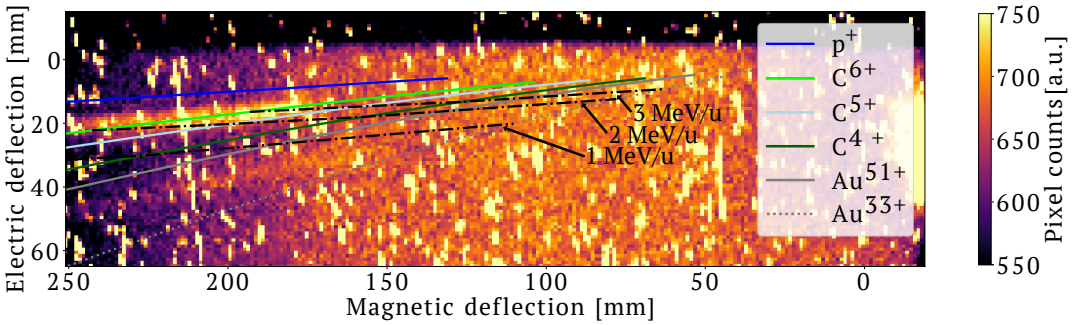

(b) Shot #104 on a 300 nm gold foil heated with 1250 mW

Figure 5.13.: Images of DRZ-high Lanex screens from shots on heated gold foils((a): 500 nm, (b): 300 nm) on 23.08.2023

6. Results of gold-ion acceleration at HF

During the previous experimental campaign at the PHELIX laser of GSI, for the first time gold ions were accelerated to energies exceeding 7 MeV/u [31]. Thanks to the improved heavy-ion TPS, the ion spectra were detected with unprecedented resolution, with single charge-state resolution up to an energy of 4 MeV/u. This high resolution enabled to precisely identify the highest charge state in the spectrum to be about Au^{72+} [31]. Together with the data reported in Ref. [150], this represents the highest charge state of gold measured in a laser-ion acceleration experiment.

The dominant ionization mechanism was expected to be field ionization. Figure 6.1 shows the ionization energy for the different charge states in the upper panel as well as the corresponding laser peak intensity in the lower panel. When comparing the peak intensity of the PHELIX laser with $2.9 \cdot 10^{20}\,\mathrm{W/cm^2}$ to the steps in the ionization potential, it becomes apparent that the observed charge state of Au^{72+} is well above the expected charge state of Au^{51+}.

Further work on simulations revealed that collisional ionization can be used to explain how these charge states can be reached [33, 151]. Au^{72+} can therefore be established as the highest charge state expected for gold accelerated in our experiments and, therefore, m/q=2.7 being the lowest reasonable mass-to-charge ratio.

The experimental results in this thesis were gathered over several experimental runs with slightly varying laser parameters, summarized in detail in Appendix A, albeit being in a comparable range. The laser parameters from an exemplary day (19.12.2023) where most of the data on CR-39 track detectors was acquired will be discussed here. The laser energy at the target position was (5.3 ± 0.4) J with a pulse length of 28 fs.

The dynamic range of the cameras in the microscope is 10-bit and therefore not sufficient to assess the laser focus fluence. Therefore, images of the focus are saved at different filter settings, with the strongest filter chosen such that no pixel in the camera with the high magnification is saturated. Following, a series of images is acquired with decreasing filter strength. As a consequence, in increasing number of pixels will saturate while light that was previously below the signal-to-noise threshold will be captured. By

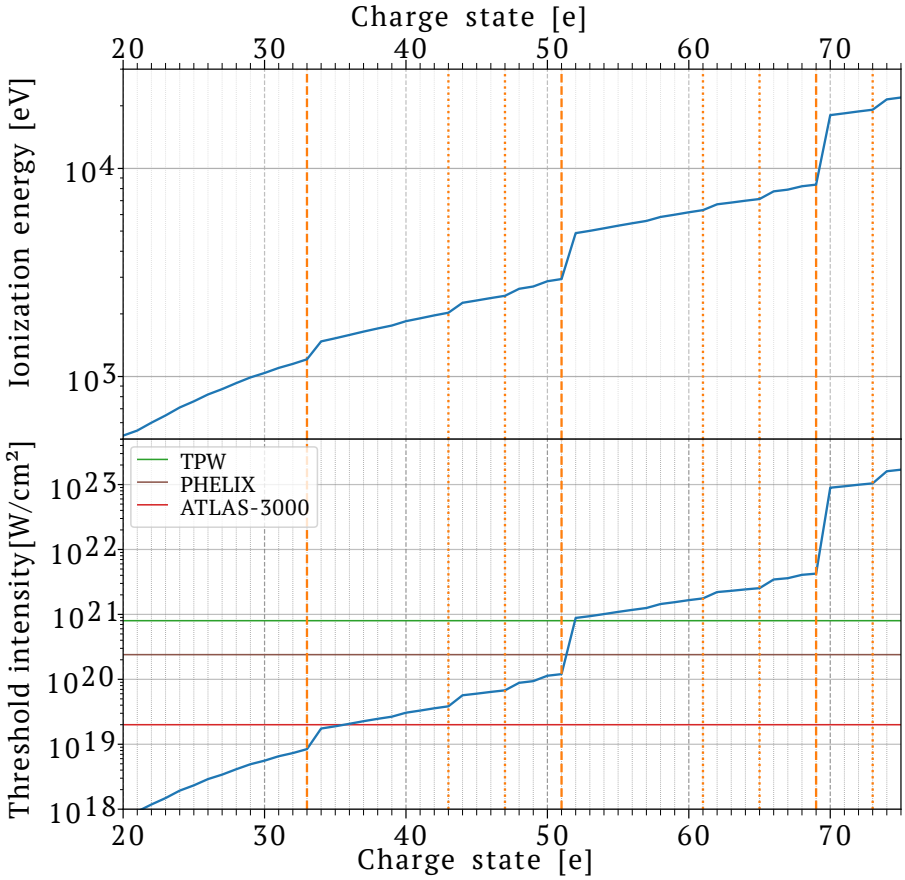

Figure 6.1.: The upper plot shows the ionization energy for individual gold charge states. The orange dashed, vertical lines indicate major steps in the ionization potential for Au^{33+}, Au^{51+} and Au^{69+} at the locations of closed atomic shells. The orange dotted lines indicate smaller steps in the ionization potential at Au^{43+}, Au^{47+}, Au^{61+}, Au^{65+} and Au^{73+}, related to electronic sub-shell closures. The ionization energy can be translated to a threshold intensity of the laser, shown in the lower plot, considering field ionization as the dominant mechanism. In addition, the laser intensity for the experiments at the PHELIX laser, the TPW and the ATLAS-3000 system are plotted.

stacking these images and replacing the saturated pixels with unsaturated pixels from images acquired with stronger filter settings, the focus can be reconstructed with a high dynamic range (HDR), extending the dynamic range by about two orders of magnitude. A High Dynamic Range (HDR) image of the focus is shown in Fig. 6.2 with a beam diameter of 11 µm at FWHM and a peak intensity of $2 \cdot 10^{19}\,\mathrm{W/cm^2}$. Details on the reconstruction of the laser focus using HDR imaging can be found in references [82] and [152]. However, it should be noted that further analysis of the focus will be necessary. For one, discrepancies exist in the HDR reconstruction between the code used in this thesis [153] and other codes available at CALA. Furthermore, these HDR images are acquired using an attenuated laser beam, i.e. with the attenuator moved into the beam path. A recent thesis conducted at the LION cave showed, that this introduces significant aberrations to the laser beam [154]. A similar study needs to be conducted in the vacuum chamber at HF to quantify the effect in these experiments.

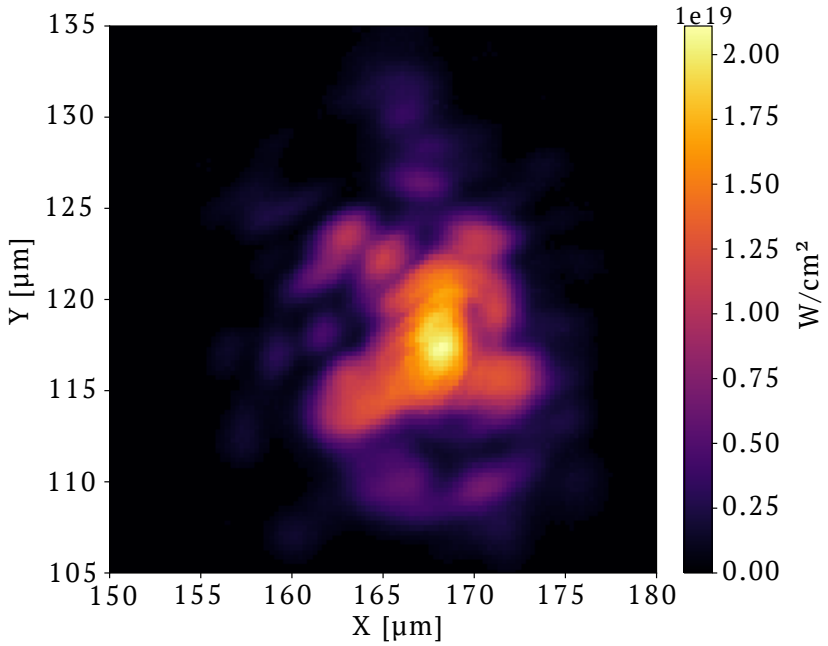

Figure 6.2.: The laser focus is captured by the camera with the high magnification setting in the microscope with different attenuation settings. These images are then stacked onto each other. By this, a high dynamic range of the laser intensity can be accessed, creating a so-called HDR image. With this, the laser peak intensity can be determined to be $2 \cdot 10^{19}\,\mathrm{W/cm^2}$ at the position of the focus, with a diameter of 11 µm FWHM.

The peak intensity for this day being at $2 \cdot 10^{19}\,\mathrm{W/cm^2}$ is significantly lower than for the previous campaigns with $2.9 \cdot 10^{20}\,\mathrm{W/cm^2}$ at the PHELIX laser and $8 \cdot 10^{20}\,\mathrm{W/cm^2}$ at

the TPW laser, as displayed in the lower panel of Fig. 6.1. The charge-state distribution reached during our experiments is shown in Fig. 6.3 for shots #1-4 on 400 nm thick gold foils, captured by CR-39 track detectors (shots #1-3 are heated, shot #4 is with an unheated target, resulting in a higher contribution by noise for signal levels below 0.3). Except for shot #1, all spectra show a peak in their distribution in the range of Au^{31+} to Au^{51+}. As expected, the charge-state range for the shots at the ATLAS-3000 system is lower compared to the previous experimental campaigns, as summarized in Tab. 6.1. This is mostly due to the lower peak intensity.

Table 6.1.: Comparison of the laser peak intensity for the different experimental campaigns and the resulting range of gold charge states. In brackets, the values from Braenzel *et al.* [155] at the Max-Born-Institut using a Ti:Sa laser are added for comparison. The similar laser peak intensity as for the ATLAS-3000 system results in a similar range of charge states, while the reached cutoff energy was lower than for our experiment, due to the lower pulse energy.

Laser system	I_0 [W/cm^2]	Charge state range	Cutoff energy [MeV/u]
TPW	$8 \cdot 10^{20}$	40-68	5
PHELIX laser	$2.9 \cdot 10^{20}$	40-72	7
ATLAS-3000 system	$2 \cdot 10^{19}$	30-51	2.5
MBI Ti:Sa laser	$8 \cdot 10^{19}$	(1-50)	1

In Fig. 6.4 the gold ion energy spectra for shots #1-4 are displayed. The cutoff energies reach up to 2.5 MeV/u. The cutoff energy being significantly lower for shot #4, which was on an unheated target, only reaching about 1 MeV at a significantly reduced particle intensity. This, again, is significantly lower compared to more than 7 MeV/u achieved at the PHELIX laser and 5 MeV/u reached at the TPW laser and is a consequence of the lower laser peak intensity and hence lower charge states. The distribution of charge states and cutoff energies are comparable to the results achieved with similar laser parameters [155]. In this work, using the Ti:Sa laser at the Max-Born-Institut (MBI), Braenzel *et al.* used 1.3 J, focused to $8 \cdot 10^{19}$ W/cm^2. They reached charge states of $\geq Au^{50+}$ with energies of ≥ 1 MeV/u.

The lower intensity also resulted in a reduced number of accelerated particles, only reaching up to about $1 \cdot 10^7$ ions/(MeV/u)/msr, as compared to up to $1 \cdot 10^8$ ions/(MeV/u)/msr accelerated at the PHELIX laser. Therefore, a larger TPS pinhole diameter of 500 µm was used for the shots on CR-39 track detectors in contrast to 100 µm diameter used during the campaign at the PHELIX laser. For the shots using a Lanex screen in combination with the sCMOS camera or for the shots on the EJ-200 scintillator with the CMOS

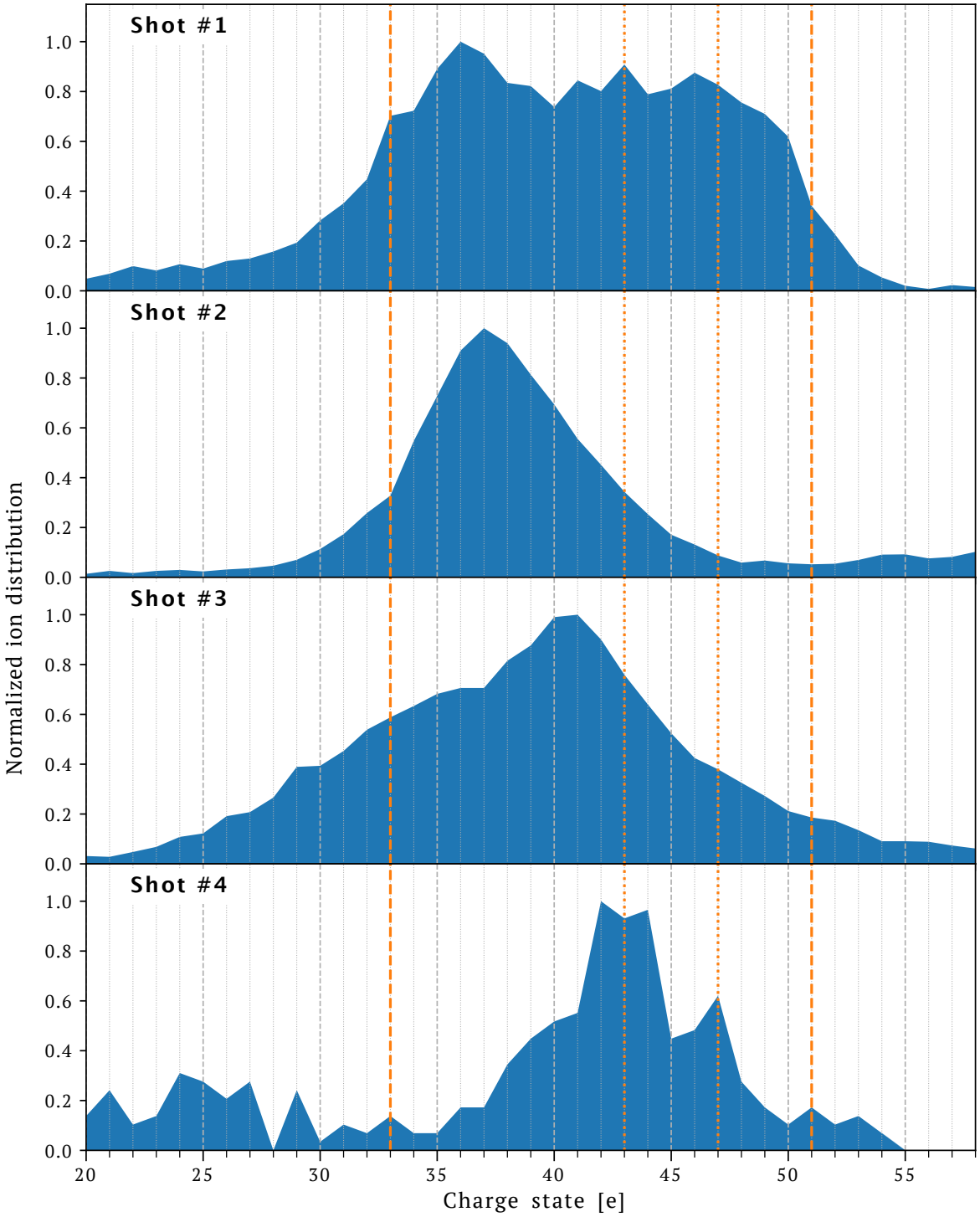

Figure 6.3.: The normalized charge-state distribution, analyzed for shots #1-4 captured by CR-39 track detectors. The dashed lines indicate major steps in the gold ionization potential, while the dotted lines are at smaller steps in the ionization potential.

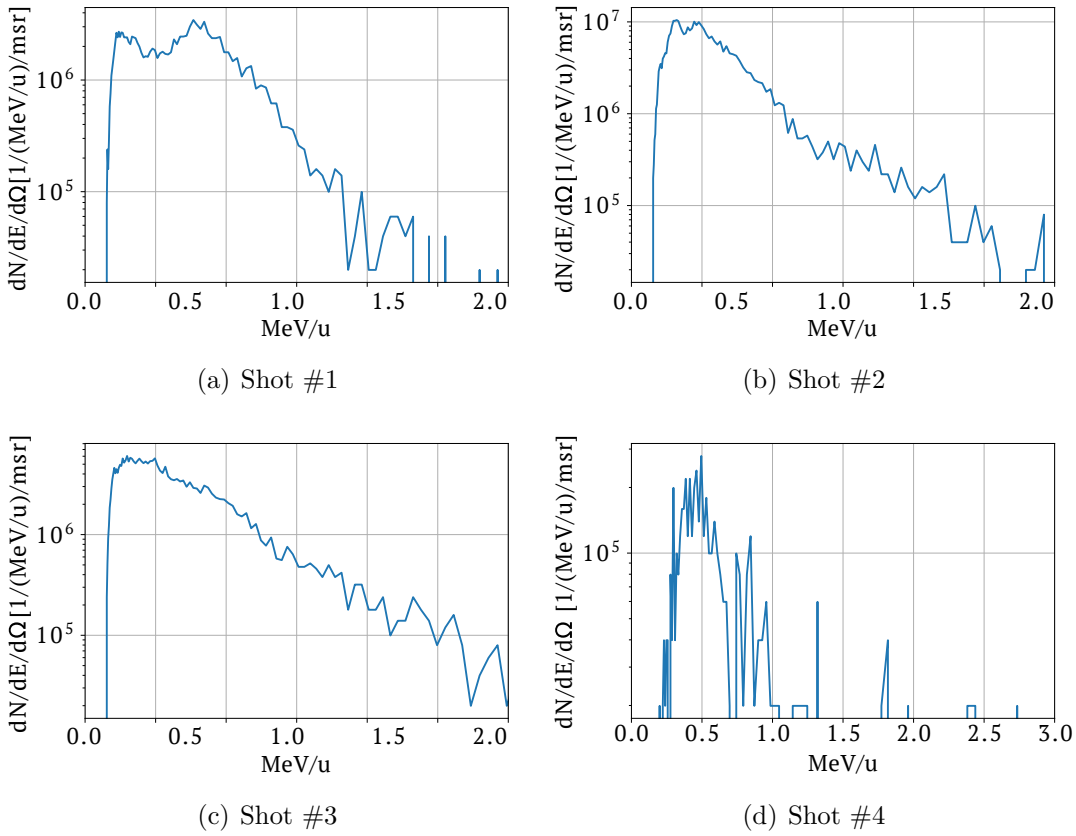

(a) Shot #1

(b) Shot #2

(c) Shot #3

(d) Shot #4

Figure 6.4.: Energy spectra of gold ions accelerated from 400 nm thick, heated targets from shots #1-4 on CR-39 track detectors. The cutoff energies are in the range of 2 to 2.5 MeV/u.

detector attached to it, even larger pinhole diameters of 1 mm and 1.5 mm had to be used. As previously discussed in Fig. 3.5, this decreases the resolution in our setup.

The resolution is further decreased due to the shorter drift length achievable in the HF cave, compared to the setup at the PHELIX laser, where the TPS was located in an extension of the target vacuum chamber. Installing a larger drift length in the HF target chamber would require a smaller angle of incidence of the laser on the target, which is currently restricted to 21° to minimize the risk of backreflexes into the ATLAS-3000, so that the ion beam could be directed into a second vacuum chamber, connected via a vacuum tube. Therefore, for this experimental campaign the single charge-state resolution for gold ions was only realized for low energies up to 0.15 MeV/u, displayed in Fig. 6.5.

These shots show the very good agreement of the prediction of the traces by the particle tracking code with the experimental data. Being able to use this method is a major improvement compared to the previously applied method [15]. This was

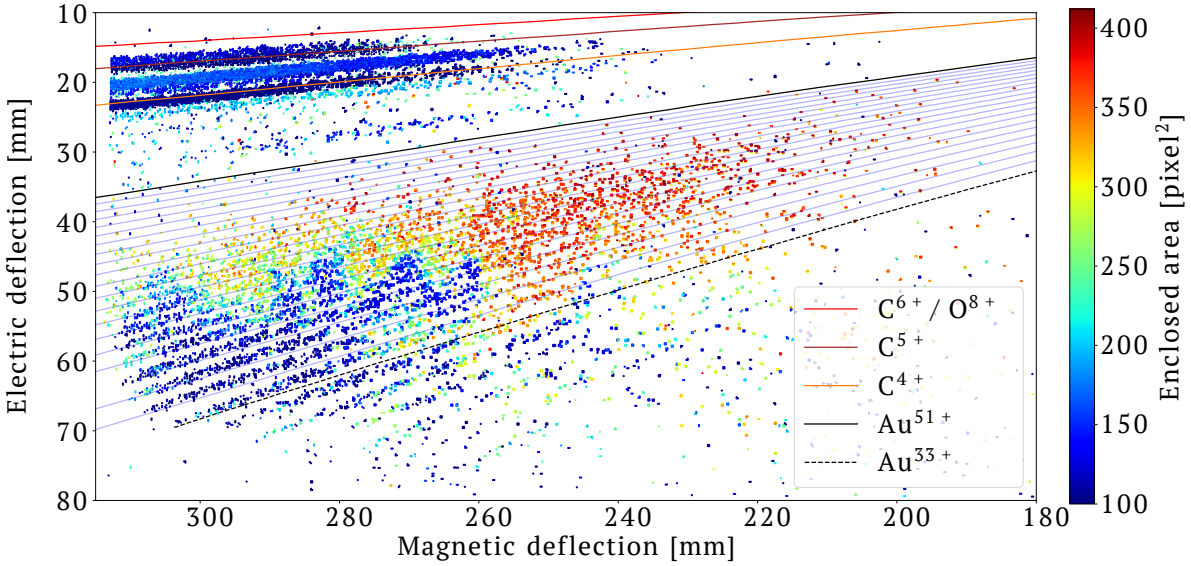

Figure 6.5.: Due to the larger pinhole diameter and the shorter drift length between TPS and CR-39 track detectors, single charge-state resolution was only achieved for gold energies up to 0.15 MeV/u. The image shows the very good agreement of the individual ion traces with the traces simulated via particle tracking and with this the robustness of the applied method.

possible because of the higher stability of the TPS' electric field for the experimental runs using the ATLAS-3000 system. This was realized by exchanging the electrode holder previously made of Polymethyl methacrylate (PMMA), with a dielectric strength of $\approx 20\,\mathrm{kV/mm}$ [156, 157] by alumina ceramics, with an electric strength specified to be $> 25\,\mathrm{kV/mm}$ [158]. In addition, the influence of the EMP is lower when using the ATLAS-3000 laser pulse compared to the PHELIX laser pulse due to the lower laser pulse energy.

As previously described in Sec. 3.3.1, one advantage of using CR-39 track detectors is the possibility to gate on different properties of the particle tracks when analyzing the slabs. It is, therefore, possible to gate only on pits up to a maximum size and hence filter the overall track ensemble for the light ions, as displayed in Fig. 6.6 for shot #2 on a 400 nm thick, heated gold target.

According to the Bethe-Bloch formula (see Eq. (2.14)), the stopping power of a material for a known ion with a specific charge state depends on its initial energy. The stopping power for an ion with a defined m/q-ratio and a lower kinetic energy is larger than for the same particle having higher kinetic energy. This results in a larger pit created by the ion experiencing the larger stopping power. This can be illustrated when looking at the

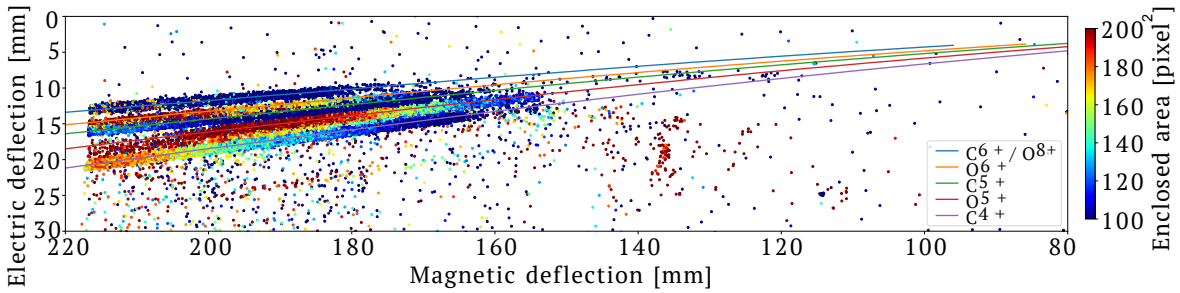

Figure 6.6.: Shot #2 on a 400 nm thick, heated gold target, gated on the light ion signal by selecting pits with areas between 100 to 200 pixel^2. Along the individual traces, the area of the individual pits is monotonically decreasing towards higher energies.

average pit area per energy bin for an ion with a defined m/q ratio and comparing it to the electronic stopping power calculated by SRIM [59] for the corresponding energy bin. This comparison is plotted in Fig. 6.7 for C^{4+} in shot #2. The average pit area per energy bin with an average width of 0.03 MeV/u (spacing is not equidistant but follows a power law, see Chap. 3) and the stopping power of the CR-39 track detectors are both decreasing monotonically with a comparable steepness, showing the strong dependence of the pit area on the stopping power of the material.

Similar to gating on the pits of light ions, the CR-39 track detector can be gated on signals generated by heavy ions, creating large pits, as shown in Fig. 6.8 for shot #3 on a 400 nm thick, heated gold target. Surprisingly, the data reveals large pits created by heavy ions beneath the signals of light ions, indicated by the calculated traces for C^{6+}, C^{5+} and C^{4+}. To ensure that these are not due a misassignment or some artifacts of the ellipse fitting algorithm of the Samaica software, Fig. 6.9 shows a microscope image of the CR-39 track detector of shot #3 at 20x magnification, showing large and small pits in an area of $70 \times 100\,\mu m^2$ size. The location of this image frame on the track detector surface is indicated by the black rectangle in the lower panel of Fig. 6.9. This proves that the heavy-ion signal is indeed registered in the region where only light ions were expected.

A histogram of the heavy-ion signal as a function of the mass-to-charge ratio is plotted in blue in Fig. 6.10. The blue curve reveals a double-peak distribution, with one peak being centered in the mass-to-charge region between $2 \leq m/q \leq 3$ and the other peak starting at $\approx m/q = 3.5$ and extending to higher values. Mass-to-charge ratios smaller than 2.7, corresponding to charge states higher than Au^{72+}, can be excluded for our experiments.

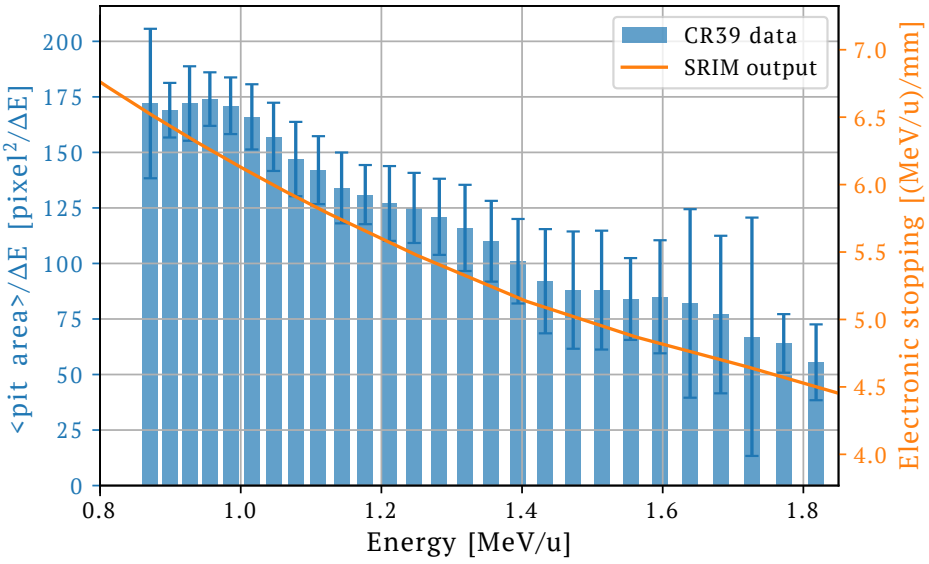

Figure 6.7.: Comparison of the behavior of the average area of the pits per energy bin of the C^{4+} ions of shot #2 (blue) on a 400 nm thick, heated gold target with the electronic stopping power of the CR-39 track detector for this species calculated via SRIM (orange), as a function of the initial ion energy. The error bars are given by the standard deviation of the area of the pits per energy bin. Both values are monotonically decreasing for higher initial energies.

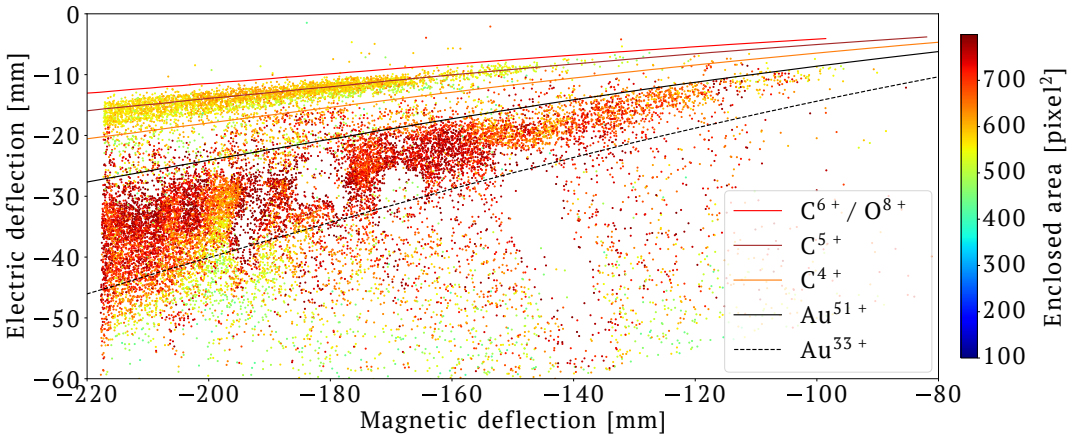

Figure 6.8.: The signal from shot #3 on the CR-39 track detector gated on large pits with an enclosed area between 400 to 800 pixel^2, created by heavy ions and only expected being dominant in the region in-between the black lines calculated for gold charge states of Au^{31+} to Au^{51+}. The data reveals signals from heavy ions unexpectedly registered in the region of light ions, indicated by the traces calculated for C^{6+}, C^{5+} and C^{4+}.

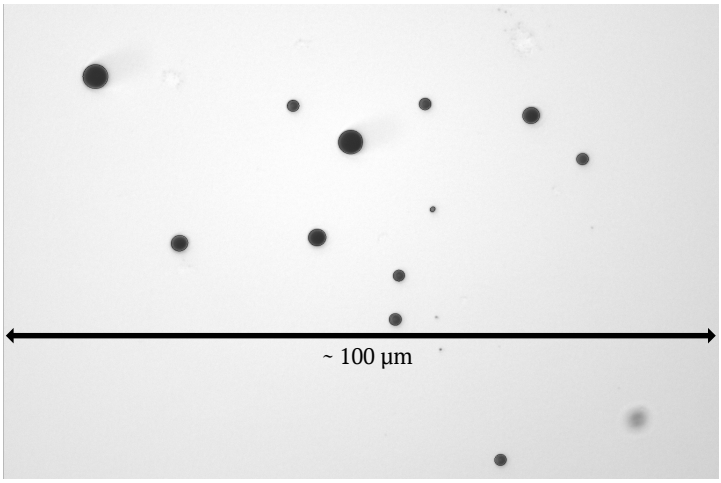

(a) Microscope image of large and small pits next to each other

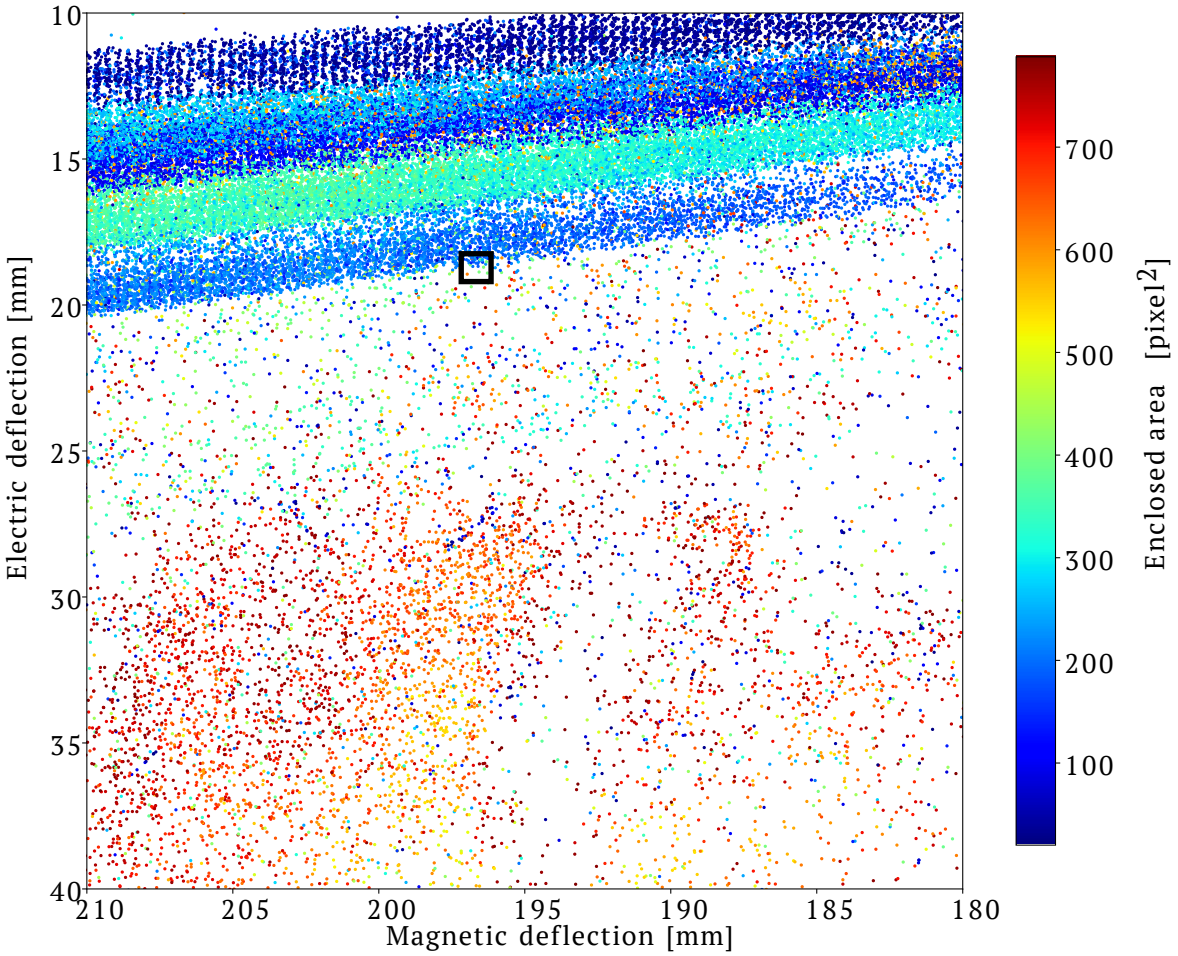

(b) Location on CR-39 track detector, where image in (a) was acquired

Figure 6.9.: The microscope image of the CR-39 track detector from shot #3 on a 400 nm thick, heated gold target, taken at 20x magnification shows large and small pits next to each other in an image frame of $70 \times 100\,\mu m^2$. This clarifies that the signal of heavy ions appearing in the region of light ions and plotted in Fig. 6.8 is representing real data. The black square in the lower panel indicates the location on the CR-39 track detector, where the image was acquired.

Similar signals of heavy ions in the region of light ions were already previously observed by Lindner *et al.* [31], included in orange in Fig. 6.10 for a PHELIX laser shot on a 500 nm thick, unheated gold target. The histogram for the heavy-ion signal from the previous experimental campaign also exhibits a double-peak structure. Due to the better resolution, the data from Lindner *et al.* will be included in this discussion.

In his shots on CR-39, individual traces could be resolved for gold ions as well as for the heavy-ion signal in the region of $2 \leq m/q \leq 3$, with no signals being detected below the unphysical region below a mass-to-charge ratio of 2. Therefore, scattering of heavy ions in the entrance pinhole (only having a diameter of 100 µm in Ref. [31]) could be excluded as a cause for the discussed heavy-ion signal, as a broad, blurred structure would be expected in this case. As a consequence, ions in the second peak with $m/q > 2.7$ can be attributed to gold ions, while pits from ions between $2 \leq m/q \leq 2.5$ cannot be caused by gold. In both experimental campaigns, the number of heavy-ion signals between $2 \leq m/q \leq 3$ amounts to 20 to 40 % of the gold-ion signal numbers, with the gold tracks being at 30 % of the signal level of the light ions.

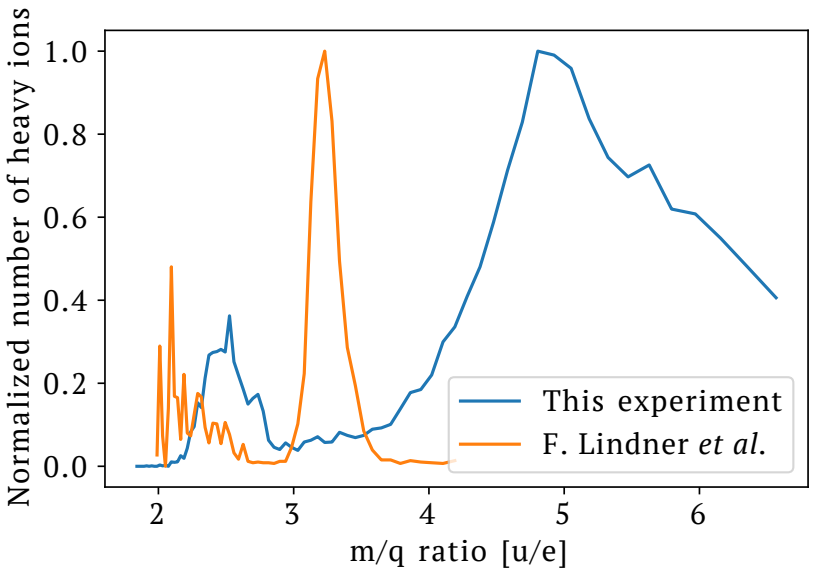

Figure 6.10.: Histogram of the heavy ion signal displayed in Fig. 6.8 as a function of the mass-to-charge ratio (m/q), based on the dispersion by the TPS (blue). In orange, the histogram of the heavy ion signal from Lindner *et al.* [15] from a shot on an unheated 500 nm thick gold target is plotted. The x-axis is binned in fixed intervals of $\Delta(m/q) = 197/q$, with $2 \leq m/q \leq 6.5$, with $q \in \mathbb{N}$.

In order to obtain more information about the unknown heavy ions, the average

pit areas of the clearly identified species gold, oxygen and carbon were analyzed. As previously discussed, besides the charge and the mass of the incident particle, the pit area is also depending on the incident energy. Therefore, only pits within a narrow energy bin of 1.14 to 1.25 MeV/u were considered and plotted as a function on their mass, as shown in Fig. 6.11. Since the stopping power of an absorbing material scales logarithmic with the mass A of the particle (see the Bethe-Bloch formula, Eq. (2.14)), a logarithmic fit was applied, following $f(A) = a \cdot \log(b \cdot A) + c$, with $a = 152\,\text{pixel}^2$, $b = 0.9\,1/\text{u}$ and $c = -124\,\text{pixel}^2$, plotted in orange in Fig. 6.11. The average area of the pits created by the unknown heavy ions amounts to $568\,\text{pixel}^2$, indicated by the horizontal, black line. The intersection of this line with the logarithmic fit occurs for a mass of about 98 u.

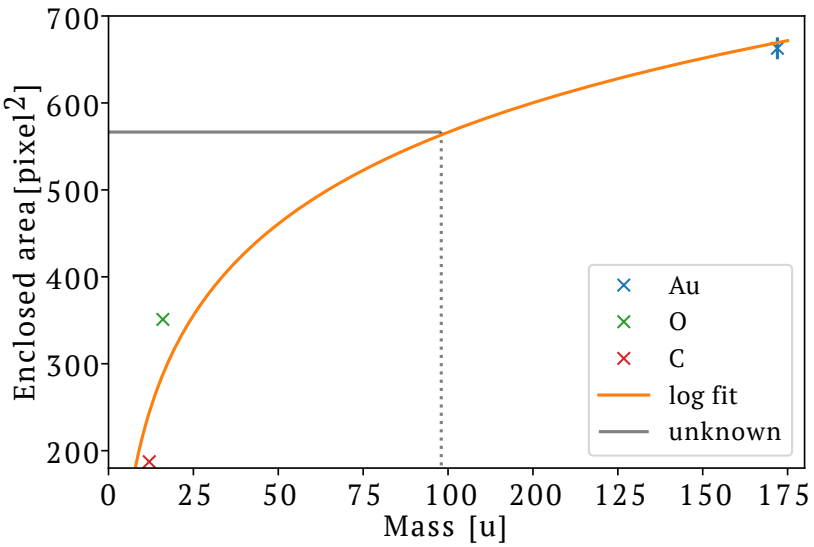

Figure 6.11.: For shot #3 on a 400 nm thick, heated gold target the pit areas of gold, oxygen and carbon ion tracks registered in a CR-39 track detector are averaged for the energy interval from 1.14 to 1.25 MeV/u. The resulting values (colored crosses) are plotted against the respective particle mass and are fitted by a logarithmic curve (orange line). The horizontal solid line indicates the average pit area of the heavy ions observed in the range of $2 \leq m/q \leq 3$ in this energy interval. The intersection point of this line with the fit is marked by a vertical dotted line, indicating a mass range of around 98 u for the unknown heavy ion component. The errorbars for the pit size are indicated but smaller than the markers for the narrow energy width considered here.

To investigate potential impurities causing the heavy-ion signals in the range of $2 \leq m/q \leq 3$, an X-ray fluorescence measurement was performed on the gold targets used during the beamtimes at CALA. For this, a Niton XL3t, a commercially available

X-ray fluorescence analyzer was used [159]. Three sets of measurements were performed, analyzing the gold foil, the gold foil mounted on the target holder and just the target holder, with three measurements per set. The normalized yields of elements are displayed in Fig. 6.12. Contributions below 10^{-2} were excluded, since their signature is too low to cause the strong unidentified heavy-ion signals in the CR-39 track detectors.

The XFA measurement of the gold foil displayed in the top panel of Fig. 6.12 shows the dominant contribution of gold with accompanying signatures of sulfur, zinc, tungsten and mercury. The resolution limit of the detector is $< 185\,\text{eV}$ [159]. Therefore, elements with an emission line closer than 185 eV to an emission line of gold can be falsely attributed as an additional elemental contribution while only stemming from a broader gold emission line. Table 6.2 gives an overview of some X-ray emission lines of the listed elements, where a gold X-ray emission line is located within the resolution limit of the detector, thus bearing the risk of a misassignment [91]. The $K_{\alpha 1}$ line for sulfur as well as the $M_{\alpha 1}$ lines of gold and mercury are close to each other within that limit, as well as the $K_{\beta 1}$ line of zinc, the $L_{\beta 1}$ line of tungsten and the $L_{\alpha 1}$ line of gold. As a consequence, a more in-depth analysis is necessary to determine whether these elements are really present in the gold foil or were just falsely assigned. However, all of these cases represent signal yields smaller by at least an order of magnitude than the leading elemental component. No emission lines from other elements were detected.

Table 6.2.: X-ray emission energies (in eV) for sulfur, zinc, tungsten, gold and mercury [91]. Values within the resolution limit of the detector (<185 eV) located in the vicinity of gold X-ray lines are either indicated in **bold** or underlined.

Element	$K_{\alpha 1}$	$K_{\beta 1}$	$L_{\alpha 1}$	$L_{\beta 1}$	$M_{\alpha 1}$
S	**2307**	2464	–	–	–
Zn	8638	9572	1011	1044	–
W	59318	67244	8397	9672	1775
Au	68803	77984	9713	11442	**2122**
Hg	70819	80253	9988	11822	**2195**

The measurement of the stainless steel target holder shows that it is made of iron with contributions from chromium, manganese and nickel as typical steel alloy components. When measuring the target holder together with the gold foil, the signal registered from the target holder is dominating, because it is much thicker than the target foil ($\approx 0.5\,\text{mm}$ compared to 500 nm). Therefore, the signal level of gold in the measurement of the foil mounted onto the holder amounts only to 0.006 relative to the target holder signal.

None of the additional potential elements identified by the XFA fits into the mass

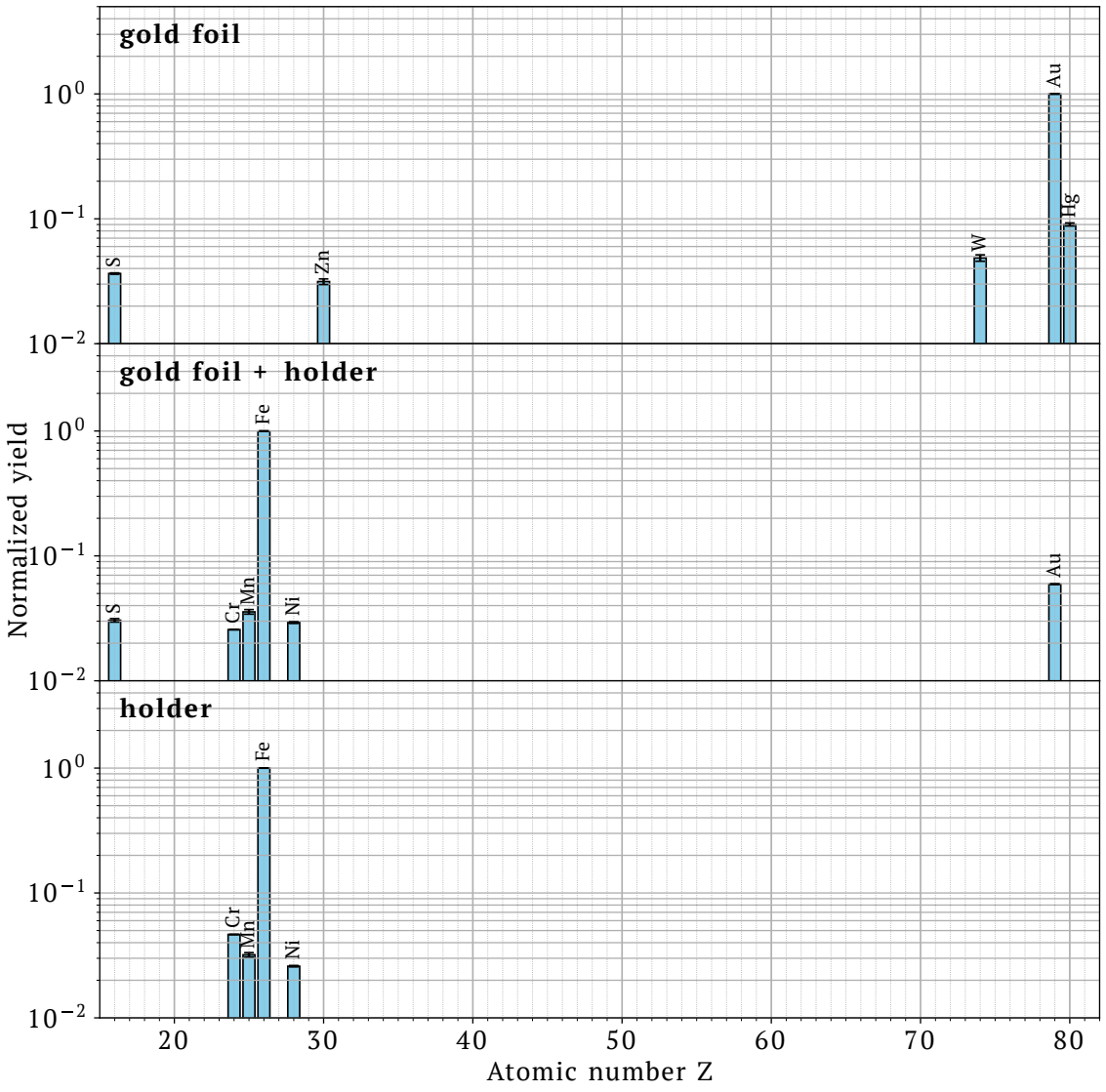

Figure 6.12.: Normalized X-ray fluorescence measurements of the gold foil (top), the gold foil together with the target holder (middle) and the pure target holder (bottom).

range identified in Fig. 6.11, with sulfur and zinc being below this value and tungsten and mercury being heavier (A(S)=32.07 u, A(Zn)=65.38 u, A(W)=183.84 u and A(Hg)=200.59 u [160]). This leads to the hypothesis that the unknown heavy ions are fission fragments of gold ions, as discussed in the following section.

7. Induced Fission: Scenarios of laser-driven in-target fission from gold foils

The increasing laser field intensities realized in recent years made it possible to use them to probe and manipulate nuclei, giving rise to a new field termed nuclear photonics [161]. While numerical studies have explored the possibility that intense laser fields might directly modify nuclear properties or enhance fission rates through mechanisms like nuclear excitation by laser fields [162], these effects remain theoretical and have not been confirmed experimentally.

Studies have shown that in gold and other heavy nuclei, fission only becomes competitive with neutron evaporation at excitation energies of around 50–80 MeV [163]. Even then, the fission cross section is relatively small compared to $(\gamma, x\mathrm{n})$ reactions, where the nucleus emits one or more neutrons when irradiated with γ rays without undergoing fission. Therefore, fission in gold has so far only been observed in experiments at conventional accelerator facilities. This chapter will explore different processes potentially able to generate the fission fragments observed in our experiments in a laser-plasma environment.

7.1. Neutron-induced fission

During the interaction of an ultra-intense laser pulse with deuterated targets, neutrons with energies of about 2.5 MeV were detected, with explanation ranging from beam-target interaction, bulk-plasma motion and fusion events [164–166]. Laser-accelerated protons were further used to induce nuclear reactions in secondary targets for the acceleration of neutrons in dedicated setups with an unmoderated exponentially decreasing neutron energy spectrum from the epithermal (few eV) region reaching out to about 80 MeV [167]. However, this process is not relevant for our setup, only using a single target.

For neutron-induced fission, the neutron transfers its energy to the target nucleus. If the neutron has sufficient kinetic energy to excite the target nucleus above its fission barrier, fission becomes one of the possible deexitation channels. The most prominent

example for neutron-induced fission is uranium. While for ^{235}U already thermal neutrons are sufficient ($kT \approx 25\,\text{meV}$ at room temperature) to cause fission, for ^{238}U energetic neutrons starting from around 1.7 MeV are necessary.

For low-energetic neutrons, an excited gold nucleus decays via the emission of γ rays or β decay [168]. For neutrons with kinetic energies above the fission barrier of gold, i.e. around 22 MeV, other deexitation channels are dominant like (n, xn), (n,p), (n,α) reactions or spallation (the emission of multiple nucleons). This is due to the much lower neutron and proton separation energies S_n and S_p for gold (e.g. $S_n = 6.512\,\text{MeV}$ for ^{198}Au [**?**]) compared to the fission barrier height (23.16 MeV for ^{198}Au [32]). Therefore neutron-induced fission is not expected for our laser-ion acceleration scenario using gold targets.

7.2. Photofission and electron-induced fission

Electron-induced fission occurs when a nucleus absorbs a high-energy electron and becomes excited above its fission barrier, resulting in the nucleus splitting into two fragments. The electrons can either directly transfer their energy to the nucleus or generate secondary γ rays via bremsstrahlung (see Sec. 2.1). These photons can then in turn trigger photon-induced fission, also called photofission. The highest possible photon energy is limited by the maximum energy of the electrons.

Laser-induced fission was first theoretically proposed by Boyer *et al.* in 1988 [169], suggesting a coupling of the laser to the atomic electrons, producing relativistic currents and subsequently causing fission. In experiments so far only photofission in heavy actinides such as ^{238}U [170, 171] (recently also via online detection methods [172]) and ^{232}Th [173] were observed. Similar results using lasers for slightly lighter nuclear species like gold have not been reported. The difference is in the fission barrier height, which amounts to 5.44 MeV for ^{232}Th and 5.63 MeV for ^{238}U, while the fission barrier for ^{197}Au is significantly higher at 22.31 MeV [32], as can be seen in Fig. 7.1.

For electron and photon energies below 100 MeV, i.e. in the vicinity of the pion production threshold of 145 to 151 MeV, the cross sections for fission are steep functions of the energy [174], as can be seen in Tab. 7.1. Therefore, a good knowledge of the energy spectra of electrons and bremsstrahlung is essential to make valid assumptions about the resulting number of fission fragments.

For both laser-ion acceleration experiments where presumably fission fragments from in-target fission were observed, neither the X-ray spectrum of bremsstrahlung was measured

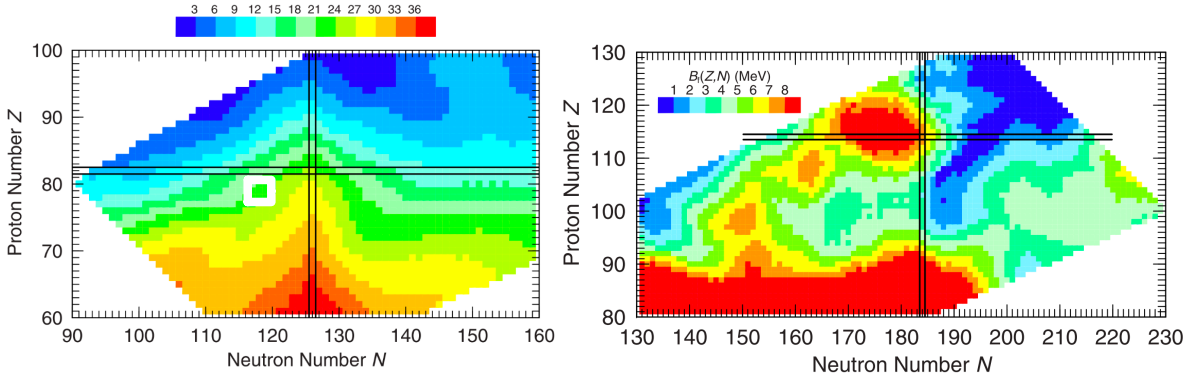

Figure 7.1.: The calculated fission-barriers for nuclei with generally lower proton and neutron numbers (left) and higher proton and neutron numbers (right). In the left image, the location for ^{197}Au with N=118 and Z=79 is indicated by a white square. The different color scale in both images shows the general trend of lower fission-barriers for heavier nuclei. Figure adapted from Ref. [32].

Table 7.1.: Measured cross sections for electron-induced fission and photofission in gold

Particle	Energy [MeV]	Fission cross section σ_f [mb]
Electron	40	$1 \cdot 10^{-7}$ [174]
	100	$1 \cdot 10^{-4}$ [174]
Photon	60	$1 \cdot 10^{-3}$ [174]
	69	$2.4 \cdot 10^{-2}$ [175]
	100	$3.4 \cdot 10^{-2}$ to $1.3 \cdot 10^{-1}$ [174, 176]

via nuclear activation techniques [41], nor was the electron energy spectrum measured. In a dedicated experiment at the PHELIX laser, the target was optimized to maximize the electron energies. For this, a foam target made out of a polymer aerogel consisting of carbon, hydrogen, and oxygen, with a thickness of 1000 µm, was placed in front of a tantalum plate of 6 mm thickness. The foam has a reduced electron density n_e compared to a solid target and therefore enables a high conversion efficiency of laser energy to hot electrons. The tantalum plate then acts as a converter for the electrons into bremsstrahlung photons. In this experiment electrons with energies up to 100 MeV were observed, with nuclear activation measurements in combination with simulations suggesting a maximum photon energy of about 70 MeV [177]. These values can be estimated to form an upper limit for the energies achievable in our experiments, while they most likely will be significantly lower for our case. For example first preliminary PIC simulations for ATLAS suggest that the electron spectrum extends only up to 20 MeV, assuming $I_L = 2 \cdot 10^{21}\,\mathrm{W/cm^2}$, $\tau = 28\,\mathrm{fs}$ and $\omega_0 = 2\,\mu\mathrm{m}$ impinging on a 400 nm thick

gold target with no contamination layer [178]. Calculating $T_{e,h}$ following Eq. (2.11) amounts to $T_{\mathrm{e,h}} = 1.3\,\mathrm{MeV}$ for the ATLAS-3000 system and $T_{\mathrm{e,h}} = 5\,\mathrm{MeV}$ for the PHELIX laser (with $a_{0,\mathrm{ATLAS}} = 4.8$ and $a_{0,\mathrm{PHELIX}} = 15.2$), well below the fission barrier of gold.

Since no exact numbers are known, we will attempt an estimate for the number of reactions by considering the maximum photon energy of about 70 MeV reported for the experiment in Ref. [177]. This corresponds to a fission cross section of $\sigma_f = 2.4 \cdot 10^{-2}\,\mathrm{mb}$ [175]. We assume the interaction volume $V_{\mathrm{acc.}}$ to be cylindrical, with the height of that cylinder given by the thickness of the target (h =400 nm). The radius of the cylinder is assumed to be $r = 50\,\mu\mathrm{m}$, which is larger than the laser focus radius $\omega_0 = 10\,\mu\mathrm{m}$. This choice was made to account for the fact, that the source size can be multiple times larger than the radius of the laser focus [179] but still acknowledging that the here discussed reaction will only occur in the high intensity region of the interaction. The reaction rate $\dot{N}$ is given by

$$\dot{N} = \sigma_f \Phi N_t, \tag{7.1}$$

where Φ is the flux of the γ rays and N_t is the number of target atoms. From the fit of the X-ray bremsstrahlung spectrum measured by Stoyer *et al.*, it can be assumed that up to $1 \cdot 10^6$ photons/MeV/msr can reach energies of 70 MeV. We will assume that the X-rays are uniformly emitted in all directions and therefore integrate over the full solid angle, i.e. multiply by 12 000 msr, which most likely is another overestimation. The X-ray flux Φ is the number of photons N_γ impinging on the target area A during the time interval $t = 1\,\mathrm{s}$, which is the minimum time between two laser shots at the ATLAS-3000 system. It then holds that

$$\Phi = \frac{N_\gamma}{A \cdot t} = \frac{1 \cdot 10^6 \cdot 12000}{\pi \left(50 \cdot 10^{-6}\,\mathrm{m}\right)^2 \cdot 1\,\mathrm{s}} \approx 1.528 \cdot 10^{18}\,\mathrm{m^{-2}s^{-1}}. \tag{7.2}$$

To calculate the number of target atoms, the total interaction volume $V_{\mathrm{acc.}}$ is divided by the volume of a gold atom $V_{\mathrm{au,atom}}$ (assuming the atomic radius of gold to be $r_{\mathrm{au,atom}} = 144\,\mathrm{pm}$ [180]):

$$N_t = \frac{V_{\mathrm{acc.}}}{V_{\mathrm{au,atom}}} = \frac{\pi \cdot (50\,\mu\mathrm{m})^2 \cdot 400\,\mathrm{nm}}{4/3 \cdot \pi \left(144 \cdot 10^{-12}\,\mathrm{m}\right)^3} \approx 2.51 \cdot 10^{14}. \tag{7.3}$$

Using Eq.(7.1) yields

$$\dot{N} = 9.21\,\mathrm{s^{-1}}, \tag{7.4}$$

which is equivalent to 9 fission products that could be produced per laser pulse with

this reaction given the assumptions that were made. Even when assuming higher values for photon energies during our experiments, the number of fission products created in this process is not able to produce the large amount of fission products observed in our experiments. Photofission, as well as electron-induced fission with even lower cross sections, can therefore be ruled out to be responsible for the observed in-target fission of gold nuclei. The next chapter will focus on fission by positively charged particles.

7.3. Fission induced by charged particles

As laid out in Chap. 4, besides gold atoms, surface contaminants are present. For our experiments they are mainly consisting of protons, carbon and oxygen ions. As they are accelerated by the laser, they are potential candidates to induce fission in gold nuclei. Direct reactions are possible but result mostly in the breakup of the projectiles [181]. Direct reactions are, therefore, not suitable to explain the origin of the heavy ions causing large pits in the mass-to-charge ratio of $2 \leq m/q \leq 3$ found on the CR-39 track detectors, indicating a mass of around 98 u. To explain these tracks, the formation of a compound nucleus with subsequent symmetric fission is necessary.

As described in Sec. 2.3.2, the barrier height for the formation of a compound nucleus, consisting of a target nucleus and a projectile nucleus, is empirically described by the Bass barrier height. To calculate this height, the code PACE4 [77] was used, displayed in Tab. 7.2 for the different projectiles. While sub-barrier fusion and subsequent fission is possible, the related cross section is strongly suppressed [182]. Therefore, these values present a minimum energy necessary for fission events to occur. In addition, Tab. 7.2 indicates the resulting compound nucleus of the interaction as well as the fission barrier B_f of the compound nucleus.

Table 7.2.: The Bass barrier height of different projectiles impinging on a gold target given in MeV/u and MeV, calculated using PACE4 [77]. The resulting compound nucleus as well as the according fission barrier B_f of the compound nucleus are indicated, according to Ref. [32].

Projectile	p^+	C^+	O^+
V_{Bass} [MeV/u]	10.6	4.7	4.6
V_{Bass} [MeV]	10.6	56.99	74.84
Compound nucleus	$^{198}_{80}$Hg	$^{209}_{85}$At	$^{213}_{87}$Fr
B_f of compound nucleus [MeV]	21.45	19.10	16.66

For the experiments by Lindner *et al.* [31] these energies are reached by the light ions,

well exceeding 7 MeV/u. For these experiments therefore fission induced by light ions presents a likely candidate. However, for the experiments conducted in the course of this work, the cutoff energies of the carbon and oxygen ions are around 2 to 2.5 MeV/u, as indicated by the spectra of carbon and oxygen ions for shot #2 on a heated 400 nm thick gold foil in Fig. 7.2. These energies are below the Bass barrier. Still, fission products were observed, so a different process needs to be responsible.

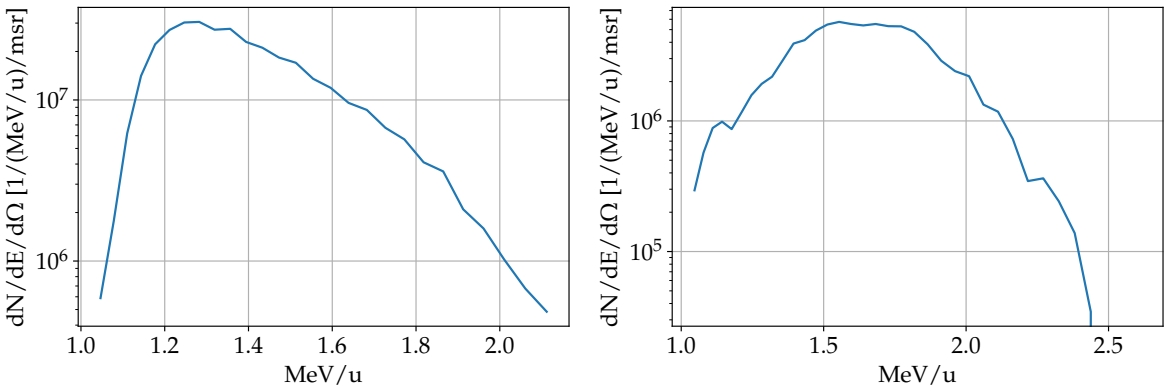

(a) Carbon (b) Oxygen

Figure 7.2.: Energy spectra of carbon and oxygen ions from shot #2 on a heated 400 nm thick gold target, detected with CR-39 track detectors. The cutoff energies are below the Bass barrier height, indicated in Tab. 7.2.

The analysis is complicated by the fact that the observables are restricted to particles after they have been accelerated out of the target. As previously laid out, probing the plasma is linked to significant effort, with no setup for probing currently being implemented in the setup at HF. This implies that the energies of individual particles inside the plasma might exceed the values at the location of the detector.

Protons, carbon and oxygen ions are the main components in our target surface contamination layer and are reported to have caused fission of gold [183–186] with typical bombarding energies ranging from 70 to 160 MeV. Since the number of protons is expected to be significantly reduced by heating the target prior to the laser interaction (see Chap. 4) and carbon ions are more abundant compared to oxygen (compare Fig. 7.2), the following analysis focuses on carbon ions.

Investigating the threshold energies for fission, the important figure of merit is the center-of-mass energy $E_{\mathrm{c.m.}}$, which is calculated via

$$E_{\mathrm{c.m.}} = \sqrt{(m_1^2 + m_2^2)\, c^4 + 2\,(E_1 E_2 + |\vec{p}_1||\vec{p}_2|c^2)}, \tag{7.5}$$

with the masses of the respective particles m_1 and m_2, their energies E_1 and E_2 and their momenta $\vec{p}_1$ and $\vec{p}_2$. Note that the energies include the kinetic energies T and the restmass energy E_0 according to $E + T + E_0$.

When looking at an accelerated particle beam impinging on a target at rest, it holds that $\vec{p}_2 = 0$ and Eq. (7.5) simplifies to

$$E_{\text{c.m.}} = \sqrt{(m_1^2 + m_2^2)\, c^4 + 2E_1 m_2 c^2}. \tag{7.6}$$

In this case, the center-of-mass energy for the collision of a gold target nucleus with an accelerated carbon ion with an assumed kinetic energy of 4.7 MeV/u (corresponding to the Bass barrier height, see Tab. 7.2), impinging on a gold target at rest is $E_{\text{c.m.}} = 53.1\,\text{MeV}$.

However, in our case we are dealing with a turbulent plasma. While the ions are mostly accelerated in the forward direction, collisions of two accelerated particles under an angle are possible. King *et al.* report on counter-propagating Al^{11+} ions and protons observed in their 1D and 2D Particle-In-Cell (PIC) simulations resulting from instabilities due to the interplay of several acceleration mechanisms [187]. In the case of a gold ion, accelerated with $T_2 = 2.5\,\text{MeV/u}$ in the forward direction colliding with a counter-propagating carbon ion with a kinetic energy of $T_1 = 0.15\,\text{MeV/u}$ is $E_{\text{c.m.}} = 54.4\,\text{MeV}$. This approximately corresponds to the center-of-mass energy for a collision with carbon ions with a kinetic energy at the level of the Bass barrier impinging on a gold target at rest. This shows, that this kind of reactions can be responsible for fission of gold nuclei by light nuclei like carbon ions, even though their energies measured outside of the target are below the barrier height needed for compound nucleus formation with subsequent fission.

To calculate the cross section resulting from such a reaction, a few assumptions were made. The acceleration volume $V_{\text{acc.}}$ was again approximated as a cylinder with $h = 400\,\text{nm}$ and $r = 50\,\mu\text{m}$. Additionally, light ions were assumed to be accelerated from a cylindrical volume with the same radius and a height of $h_{\text{cont.}} = 10\,\text{nm}$, corresponding to typical values assumed for the thickness of contamination layers in PIC simulations [188, 189]. The number of light ions was calculated similar to Eq. (7.3), assuming only carbon ions with an atomic radius of 70 pm [190], amounting to $N_p = 5.4 \cdot 10^{13}$. Analogous to Eq. (7.2), the carbon ion flux is estimated to be $\Phi = 6.96 \cdot 10^{21}\,\text{m}^{-2}\text{s}^{-1}$. The number of reaction products per shot, which is equivalent to the reaction rate $\dot{N}$, is estimated from the integration of the spectrum of the fission fragments to be $\dot{N} \approx 1 \cdot 10^7\,\text{s}^{-1}$, assuming that most of the fission fragments get accelerated in the forward direction [184]. From these assumptions, the fission cross section amounts to

$$\sigma_f = \frac{\dot{N}}{\Phi N_t} = 5.7 \cdot 10^{-2}\,\mathrm{b}. \tag{7.7}$$

Note that this estimation varies with the assumed radius of the acceleration volume. When changing it from 50 µm to 10 µm the cross section changes to $\sigma_f = 1.4\,\mathrm{b}$. While this is only a coarse estimation, it fits reported values in literature. Gordon *et al.* investigated fission of gold by carbon ions at different energies. They report a steep increase of the fission cross section for higher carbon energies, reaching up to 1.28 b for carbon ions with 124 MeV (=10.3 MeV/u) [191]. Similar results of $\sigma_f = 1.35\,\mathrm{b}$ for carbon ions with a kinetic energy of 126 MeV (=10.5 MeV/u) have been reported by Britt *et al.* [192]. In their work, they also report on fission induced in gold by oxygen ions with a kinetic energy of 168 MeV (=10.5 MeV/u), amounting to $\sigma_f = 1.8\,\mathrm{b}$. The same cross section was reported by Quinton *et al.* with oxygen ions of 160 MeV [185]. The cross sections for protons are significantly lower. Kruger and Sugarman report on $\sigma_f = 61\,\mathrm{mb}$ for protons with kinetic energies of 450 MeV [193]. Similar values are reported by Hudis and Katcoff starting at $\sigma_f = 59\,\mathrm{mb}$ for 0.6 GeV protons, reaching up to 76 mb for 2 to 3 GeV, before the cross section is declining again for higher energies, e.g. reaching 67 mb for protons with 13 GeV [194].

While the calculation shown here is based on some vague assumptions and the fission cross section is largely influenced by the choice of the acceleration volume as well as the assumptions on the production rate of the fission fragments, it shows that the order of magnitude estimate fits well with reported values in literature. Nevertheless, the calculation is based on center-of-mass energies for the collisions exceeding the energies of the individual species detected via the CR-39 track detectors. Detailed PIC simulations tracking the trajectories of the different species will be necessary to verify whether the assumption of head-on collisions during the acceleration process is realistic.

8. Discussion

The data presented in this thesis present the third experimental campaign conducted by our group accelerating gold ions using lasers with high peak intensities, varying pulse lengths and pulse energies aiming at deepening the understanding of laser-based acceleration of heavy ions in order to realize the fission-fusion reaction scheme. While previous campaigns were conducted as beamtimes as users at external laser facilities, the experiments in this thesis were conducted at the HF cave at CALA in a dedicated vacuum chamber, whose infrastructure was further improved in parallel to this thesis.

Over the course of the previous experimental campaigns, the target heating setup was improved by using more stable heating lasers with a higher output power, such that for some shots of the last campaign at the PHELIX laser, the target surface could be cleaned of protons. To gain a better understanding, a dedicated setup was set up outside of the HF vacuum chamber, to enable dedicated studies of the heating of gold targets, with first attempts of deriving the target temperature from the emitted thermal IR spectrum by the heated targets [131]. This setup was then transferred to the HF cave and in the course of this thesis put into operation, covered by a subsequent master thesis [132]. In the campaign at the TPW, the heating laser was damaged by the light generated during the interaction of the TPW laser pulse with the target. The risk of damage for our setup was quantified and the heating laser was protected by two narrow bandpass filters, blocking damaging back reflected light. The setup was then adapted by guiding the heating laser onto the target from outside the vacuum chamber. An optical fiber was implemented into the microscope, guiding the IR radiation emitted from heated targets to a spectrometer situated outside the HF vacuum chamber. In a dedicated study, the heating of targets in vacuum was investigated, which as expected, required lower heating laser output powers compared to the previous test stand in air due to the lower convection possible in vacuum. Furthermore, the target temperature was successfully determined from the emitted thermal IR spectrum by fitting Planck's law. Targets of the same thickness showed a reproducible response with regard to temperature and damage as a function of the heating laser output power. This way, a so-called safe heating laser setting was determined for every thickness, allowing for a good, uniform heating while maintaining the target's integrity.

In a next step, the influence of the heating on the gold ion acceleration performance was investigated. Without heating, no significant acceleration of gold ions could be observed. On the CR-39 slabs a reduced number of light ions with lower energies as compared to the heated shots were detected. The same was observed using the Lanex screen setup as detection tool. In addition, no protons could be detected for heated foils in contrast to unheated foils. This leads to the conclusion that the heating mostly affects the number of protons remaining on the surface of the gold foils.

The different effect of target heating observed for the experiments at the PHELIX laser, the TPW and the ATLAS-3000 system can be explained based on the pulse length of the respective lasers. For the TNSA ion acceleration mechanism the presence of the accelerating field is closely related to the laser pulse length, with some models stating an explicit relation of $\tau_{\mathrm{acc}} = 1.3 \cdot \tau_{\mathrm{L}}$ [45]. If this field is sustained only for a short amount of time like for the ATLAS-3000 pulse (28 fs) and many protons are present, they are predominantly accelerated and will thus shield the accelerating field from light and heavy ions, decreasing their efficient acceleration. If the acceleration field is sustained for longer times like at the TPW (140 fs), it is still present to accelerate ions with lower charge-to-mass ratios, after the protons are accelerated away from the target foil. For even longer pulse lengths like at the PHELIX laser (500 fs), the accelerating field is sustained long enough to accelerate all present ions over all charge-to-mass ratios, diminishing the effect of target heating.

Within the framework of this thesis, the first successful study at CALA was conducted directly comparing the effect of the target heating on the gold ion acceleration performance. To date, this comparison is only available for one target thickness and one output power setting of the heating laser. Further research will include investigations of correlations between the measured gold cutoff energies with different heating laser output powers for the same thickness of gold foils. A similar trend between these values as for the target temperature presented in Fig. 4.5 would be expected, potentially with an offset with regard to the output power.

Such studies require a large dataset. In contrast to experiments at the PHELIX laser we are not limited by the repetition rate of our laser, but by our offline CR-39 nuclear track detectors, which required timely venting in-between shots. Reliable online diagnostics is therefore crucial. With the investigation of Lanex screens in combination with an sCMOS camera as well as EJ-200 scintillators attached to a CMOS detector, this thesis presents two promising candidates to be used for the characterization and tuning of the ion acceleration.

Accelerated ions could be detected using both setups, while a reliable and quantitative detection of gold ions needs further improvement. The Lanex screen in combination with an sCMOS camera offers a cheap and durable alternative with a linear response to particle numbers and easy handling. In our experiments, using the Lanex screen for a successful detection of gold ions was circumvented by an unfavorable signal-to-noise ratio dominated by abundant X-ray background. The imaging of the Lanex screen onto the sCMOS camera can be significantly improved. Foremost, the relative position of the mirror can be improved following Lambert's law by moving it in a more forward direction to maximize the light collection. In a recent study conducted at CALA using the Cawo Lanex screen and laser-accelerated electrons, a deviation from Lambert's law was observed for the low energetic electrons, that were fully stopped in the screen [195]. Such effects need to be considered when attempting an absolute calibration of the Lanex screen for the online detection of heavy ions and will need further investigations. Furthermore, the zoom objective in our setup was not used to its full capacity, because no sharp image could be produced because of the interplay of zoom setting and permissible focal distances. This way, large parts of the sCMOS chip were wasted to capture regions outside of the Lanex screen, decreasing the resolution. In addition, no bandpass filter adapted to the size of the front side of the camera objective was available. Again, due to the limited range of object and image distances creating a sharp image, it was not possible to install a smaller bandpass filter between the zoom objective and the sCMOS chip. Without a bandpass filter, the setup relied on a reliably tight installation of the black aluminum foil, shielding the camera from laser light and light from the laser-target interaction, which was not always successful. By using a bandpass filter, the signal-to-noise ratio could be improved. The light yield can further be significantly improved by using a larger lens (i.e. with larger numerical aperture for same focal length). In any case, an objective should be chosen with a suitable working distance to create a sharp image of the scintillator at the desired zoom setting. If necessary, a further relay lens or so-called teleconverter adapter could be tested to accommodate the bandpass filter before the camera chip. In addition, the signal-to-noise ratio when using Lanex screens was decreased due to the high background level causing a glowing of the screen, most likely caused by X-rays created by the laser-target interaction by energetic electrons converted via bremsstrahlung either in the target or by scattering of the experimental setup. In future experiments, potential shielding of the X-rays needs to be further investigated in order to increase the signal-to-noise ratio.

The CMOS detector that was used in combination with the EJ-200 scintillator was only

available for a short period of time, which was mostly dedicated to solving EMP issues and obtaining a general understanding of its performance. More systematic acquisition of dark images, e.g. after every shot, could increase the general signal-to-noise ratio by being less susceptible to a thermal increase of the background over time. However, the available active area of the tested detector of $14 \times 12\,\mathrm{cm}^2$ is not sufficient to capture protons and gold ions simultaneously. For experiments in combination with the heavy-ion TPS, the larger detector with an active area of $28.3 \times 24.1\,\mathrm{cm}^2$ would be beneficial [122]. By optimizing the scintillator thickness, fiber optic plate and coupling thereof, a resolution of the order of the pixel size should in principle be attainable, again providing sufficient resolution to resolve the projected pinhole size on the detector. The light yield cannot be influenced significantly in this setup (for a given scintillator material and thickness), so the reduction of background signal is crucial.

Once online measurements of intense gold ion bunches are possible, an absolute calibration of their signal strength to the absolute particle number for our setup is necessary to provide useful information for experiments. Nevertheless, even with the limitations experienced during the experiments presented in this thesis, both detector types can already be used to provide immediate feedback in order to tune the acceleration of gold ions by observing the cutoff energy of accompanying light ions.

All so far studied online detectors lack a sufficiently high signal-to-noise ratio. To mitigate this deficit, the diameter of the entrance pinhole to the TPS was increased from 500 µm to 1.5 mm and 1 mm, respectively, in order to increase the signal strength. In turn, the resolution of the spectrometer was significantly reduced, not reaching any more the single charge-state resolution for gold ions with energies up to 4 MeV/u as achieved with an 100 µm pinhole in the PHELIX laser experiments [31]. Increasing the number of accelerated particles could simplify the requirements on online detection.

In the experiments conducted in the course of this thesis, the maximum intensity that was used was limited by the combination of laser contrast and target thickness. With a maximum gold foil thickness of 600 nm, using higher intensities than discussed in this thesis resulted in a decrease of ion performance. This is most likely due to insufficient laser pulse contrast, i.e. light arriving at the target prior to the main pulse and destroying the target before the main pulse can interact with it. This led to lower charge states and simultaneously lower cutoff energies of the gold ions of about 2.5 MeV/u compared to up to 7 MeV/u in previous campaigns [31]. In recent experiments accelerating protons (and light ions), the applied laser intensity could be increased by using significantly thicker targets, namely 12 µm thick aluminum foils. Thus the achievable maximum proton

energies could be improved from 20 MeV to $\approx$ 30 MeV including a significant increase in particle numbers, with definite numbers still being under investigation at the time of the submission of this thesis. Investigations are currently underway how to produce gold foils with equivalent thicknesses at reasonable costs. If successful, a similar improvement of gold cutoff energies and particle numbers could be expected as for the aluminum foils. As already stated above, a significant increase in particle numbers would enable using entrance pinholes to the TPS with smaller diameters and hence improving the TPS' resolution as well as simplifying the requirements on online detection.

Due to the more stable electric field of the TPS in our experiment, a more robust analysis routine could be employed compared to previous experiments [15]. For future experiments a cross-calibration of the routine would be desirable to estimate its uncertainty. For this for example an aluminum foil with a known thickness could be placed on top of a CR-39 track detectors, creating a so-called cutoff: Only ions with kinetic energies above a threshold value (which can be simulated using SRIM) would be detected. With the current data no cross-check of the simulated particle traces is possible. Therefore, the estimation of the uncertainty of the routine is difficult to make. On the grounds of the current data the simulated traces seem to describe the detected traces well.

Despite the reduced cutoff energy for gold ion acceleration at CALA, we were able to reproduce the unexpected observation of heavy-ion signals with a mass-to-charge ratio of $2 \leq m/q \leq 3$ already reported in previous experiments [31]. These results were further investigated in the course of this thesis. In a first step, the agreement between the change of ion pit size for light ions depending on their energy and the resulting stopping power $\mathrm{d}E/\mathrm{d}x$ as calculated with SRIM was validated. The dependence of the track area on the ion mass for a narrow energy bin of the identified ion species of carbon, oxygen and gold ions could be established. This way, the mass of the unknown heavy ions in the mass-to-charge ratio of $2 \leq m/q \leq 3$ could be constrained to be around 98 u. This supports the former hypothesis [31] that these heavy ions originate from fission of gold ions inside the target during the the laser-plasma interaction.

Therefore, this thesis discussed potential processes causing fission of gold ions in an attempt to identify the mechanism generating the gold fission fragments. The available energies of accelerated species are too low for neutron-induced fission and the cross-section for electron-induced fission as well as photofission are too low to explain the high yield of fission fragments. Currently, fission induced by light charged particles, with carbon ions in particular, seems most likely. The basis of this assumption is the turbulent plasma environment, that proceeds laser-based acceleration of ions, allowing for head-on

collisions of gold and carbon ions. Since no time-resolved probing of such processes is possible, meticulous PIC simulations are necessary to confirm these assumptions.

Figure 8.1 shows the distribution of masses of fission products for three reactions. Besides the mass yield for fission of gold by carbon ions with kinetic energies of 112 MeV, the mass yields for fission of bismuth by deuterons with kinetic energies of 22 MeV and 190 MeV are displayed. Comparing the mass yield curves for fission of bismuth shows a narrower peak for the low-energy bombardment. The authors of Ref. [186] attributes this to a lower excitation energy or less variety of the fissioning nuclei. Therefore, additional insights could be gained if a better detection of the mass distribution of the fission fragments could be achieved. In general an identification of the isotopes present in the fission fragments would increase our understanding.

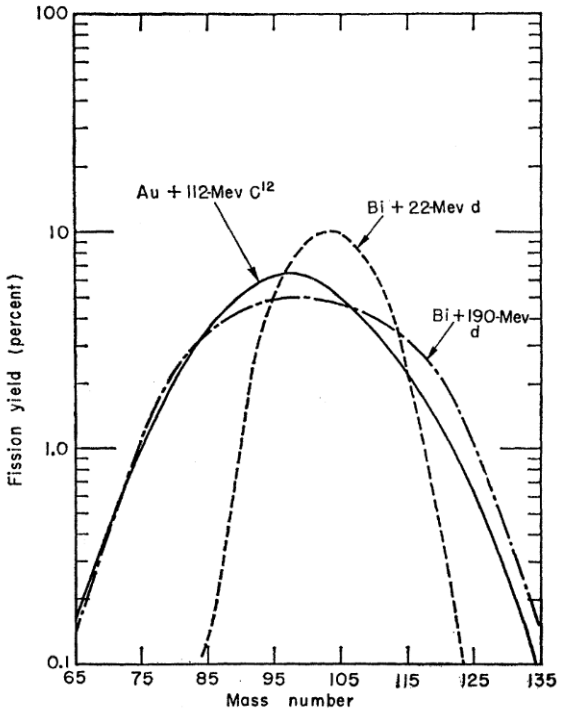

Figure 8.1.: Besides the mass yield curve for the fission of gold by carbon ions with a kinetic energy of 112 MeV also the curves for fission of bismuth by deuterons with energies of 22 MeV and 190 MeV, respectively, are displayed. The data show a broader distribution of fission fragment masses for bombardment with ions with higher kinetic energies, i.e. higher excitation energy of the fissioning nucleus. Figure taken from Ref. [186].

While mass spectroscopy is not feasible at CALA, identification of some of the fission products is expected to be possible via γ spectroscopy. For this, a so-called catcher foil

could be used, capturing and stopping the accelerated fission fragments. By analyzing the thus activated catcher foils via γ spectroscopy, isotopes could potentially be identified by their characteristic γ peaks. This foil could be mounted in front of the TPS with a hole in the middle, aligned to the entrance pinhole to the TPS. This way, a simultaneous measurement of catcher foil activation and accelerated ion spectra would be possible. γ spectroscopy is typically done using high-purity germanium detectors. As these detectors require cooling and only can be operated at distance from the vacuum chamber in order to not be damaged by the high EMP during the laser-target interaction (compare Ref. [196]), the catcher foil would need to be implemented in combination with a vacuum lock, assuring that also isotopes with small half-lives could be detected and not remain undetected due to long venting times. A first feasibility study is planned in the course of a master thesis at HF. In a first step, potential materials for catcher foils need to be tested, also investigating their nuclear activation when simply using plastic foils and thus only accelerating protons and light ions. Angular resolved measurements of fission fragments are a common technique used in fission experiments, giving further insight on the center-of-mass dynamics of the fission process. An implementation of a sophisticated setup with established methods is not feasible in the HF experimental chamber. Using multiple TPS at different angles could be a potential first experimental realization towards angular resolved measurements.

The observed fissioning of gold has major implications. For a long time, using laser-based ion acceleration has been discussed to be used as an ion source for conventional accelerators, focused by a solenoid and then selected for injection by a subsequent magnet [197]. The general feasibility of such an injector is still to be demonstrated, with major limitations of high repetition rate injection in combination with high energy remaining a major challenge. Nevertheless, the fission fragments observed in this thesis would broaden the number of species that could be injected when using gold as a target for a next-generation, compact heavy-ion accelerator. But most interesting are the potential implications for the fission-fusion reaction scheme, which is the underlying motivation for this work. Using the double target configuration as presented in Chap.2, the potential yield could be increased, since the fissioning could already occur in the first reaction target. Nevertheless, the scheme relies on the high density of the created fission fragments. More detailed knowledge about the in-target fission dynamics is necessary to understand how quickly beam parameters would diverge and hence not be able to contribute to the fusion cross section. If the investigations further show that this effect is possible in thick foils (thick in this context means several tens of micrometers, still

allowing laser-based acceleration of ions), maybe the double target configuration can even be replaced by a single target, hereby decreasing the complexity of the experimental setup. However, again careful considerations will be needed to investigate how thick such a target could be in order for the potential fusion nuclei to not be fully stopped in the target, so that they can be detected. If again experiments would show that the stopping power of the material is reduced due to collective effects, this would simplify the requirements.

9. Conclusion and Outlook

The motivation of this work are preparatory studies towards the realization of the fission-fusion reaction scheme, before working towards the realization of the scheme at large scale facilities like the 10 PW beamline at the Extreme Light Infrastructure - Nuclear Physics (ELI-NP) near Bucharest with envisaged intensities of up to $10^{23}\,\mathrm{W/cm^2}$ [198]. The previous experimental campaign by our group reached a milestone by accelerating gold ions above the required threshold energy of 7 MeV/u [15]. Furthermore, the unprecedented single charge-state resolution up to 4 MeV/u for gold ions allowed to understand, that the ionization dynamics do not just rely on field ionization, but follow more complex dynamics. Collisional ionization was later on identified to contribute to these very high charge states [33, 189].

The aim of this work was to further enhance the understanding of laser-based acceleration of heavy ions as well as enabling the acceleration at higher repetition rates compared to previous campaigns. For this, the experiment was conducted using the ATLAS-3000 system, delivering laser pulses with ultrahigh-intensity at 1 Hz repetition rate.

For this, the heating setup was implemented and dedicated studies were conducted, transferring the setup for the previous test stand to the experimental chamber, investigating the heating behavior of targets in vacuum compared to the previous setup in air. The temperature of heated targets was successfully determined and heating laser output power that was safe to operate without damaging the target could be established for every target thickness used throughout this thesis. A full characterization of the heating efficiency was hindered by the limited sensitivity in the detection of protons, which should be improved for following experimental campaigns. This is necessary in order to further improve the heating setup, becoming even more important once thorium is used as a target, being known to oxidize quickly. In summary, the successful acceleration of gold ions up to energies of around 2.5 MeV/u was shown for the first time at CALA. This lays the foundations for further studies regarding the influence of the laser parameters and especially target heating parameters.

To acquire the necessary large dataset, reliable and quantitative readout of online diagnostics is highly beneficial. To this end, this thesis presents two approaches using inorganic and organics scintillators. Both approaches seem to be promising candidates

with some refinements in the setup. So far only reliable detection of lighter ions could be demonstrated, with the detection of heavier ions being limited by the available signal-to-noise ratio of the setup.

This thesis further enforced the interpretation of the unknown heavy ions unexpectedly detected in the mass-to-charge region of $2 \leq m/q \leq 3$ to originate from fissioning of gold, also investigating the potential mechanisms enabling fission of gold for our experimental conditions. This motivates further work in the areas of experiments as well as simulations to enhance the understanding of the dynamics during the interaction of laser pulses with ultrahigh intensity with overdense targets. From this, potential implications and simplifications for the fission-fusion reaction scheme could be derived.

Further steps towards the realization of the fission-fusion reaction scheme include research on fission induced by laser accelerated ions. First experiments investigating the fission of heavy ions by laser-accelerated light ions already have been demonstrated [196], with similar research being undertaken at CALA in the scope of a PhD thesis. The fission of laser-accelerated heavy ions impinging on light ions, as also discussed as part of the fission-fusion reaction scheme, remains yet to be demonstrated. Currently there is no experimental area available, where laser-based acceleration of fissile ions is possible. The reason for this are radiation protection precautions. The focusing of an ultrahigh-intensity laser pulse on a target made of thorium or uranium in order to directly accelerate heavy, fissile ions would result in radioactive contamination of the target chamber, which then afterwards requires dedicated handling and cleaning.

In parallel, experiments are conducted to investigate the relevance of collective effects influencing the stopping power of materials for impinging ion bunches with very high density. The number of fusion fragments that can be produced via the fission-fusion reaction mechanism is expected to be increased by a factor of 10^4, if a reduction of the stopping power by a factor of 100 would prove to be valid.

While previous experiments reached energies of gold ions exceeding 7 MeV/u, the underlying acceleration mechanism was TNSA. Therefore, only a small fraction of the accelerated gold ions were above that threshold. Demonstration of RPA accelerating heavy ions would be important to realize higher densities of the accelerated bunches and simultaneously have a larger fraction of the ions in the spectrum above the threshold energy. This is because RPA is predicted to accelerate ion bunches with close to solid-state density, exhibiting a narrower energy bandwidth.

Besides the already mentioned future experiments, in the close future experiments at the HF vacuum chamber using gold foils of several micrometer thickness are intended,

aiming at higher cutoff energies and particle numbers in combination with higher laser energies that will be accessible when using thicker foils. With this, the results presented in this thesis could be confirmed, especially with regard to the produced fission fragments and the feasibility of online diagnostics for heavy ions beside MCPs.

A. Overview of laser parameters on the different shot days

For every relevant shot day the average energy measured at the last amplifying crystal E_{A2} (the error is given by the standard deviation of the data), the type of the employed scintillator and the drift length between the end of the TPS magnet and the scintillator d_B(Scint.) is given. If applicable the CR-39 track detector d_B(CR-39) as well as the number engraved on the CR-39 are given as well. For days with several values for E_{A2}, the number of pumping lasers were changed in-between runs.

31.05.2023

E_{A2} [J]	14.3 ±0.05
type	Cawo
d_B(Scint.) [mm]	650
d_B(CR-39) [mm]	-
CR-39 #	-

17.08.2023

E_{A2} [J]	13.05 ± 0.43 12.30 ± 0.11 10.67 ±0.10
type	DRZ-high
d_B(Scint.) [mm]	650
d_B(CR-39) [mm]	615
CR-39 #	108

23.08.2023

E_{A2} [J]	12.3 ± 0.69 10.85 ± 0.09 9.13 ± 0.13
type	DRZ-high
d_B(Scint.) [mm]	650
d_B(CR-39) [mm]	615
CR-39 #	104

05.10.2023

E_{A2} [J]	14.25 ± 0.05
type	EJ-200
d_B(Scint.) [mm]	615
d_B(CR-39) [mm]	-
CR-39 #	-

19.12.2023

E_{A2} [J]	7.7 ± 0.4
type	DRZ-high
d_B(Scint.) [mm]	574
d_B(CR-39) [mm]	615
CR-39 #	Shot #1: 101 (heated) Shot #2: 117 (heated) Shot #3: 122 (heated) Shot #4: 132 (unheated) Shot #5: 127 (unheated)

Bibliography

[1] Strickland, D. & Mourou, G. Compression of amplified chirped optical pulses. *Optics Communications* **56**, 219–221 (1985). https://linkinghub.elsevier.com/retrieve/pii/0030401885901208.

[2] C.P.J.Barty. ICUIL World Map (2020). Accessed on 04.09.2025, https://www.icuil.org/downloadss/laser-labs.html.

[3] Yoon, J. W. *et al.* Realization of laser intensity over $10^{23}\,\mathrm{W/cm^2}$. *Optica* **8**, 630–635 (2021). https://doi.org/10.1364/OPTICA.420520.

[4] Preuss, P. BELLA Laser Achieves World Record Power at One Pulse Per Second (27.07.2012). Accessed on 04.09.2025, https://newscenter.lbl.gov/2012/07/27/bella-laser-record-power/.

[5] DFG Research Unit FOR 2783. Probing the quantum vacuum (2025). Accessed on 04.09.2025, http://quantumvacuum.org.

[6] Salgado, F. C. *et al.* Towards pair production in the non-perturbative regime. *New Journal of Physics* **23**, 105002 (2021). https://dx.doi.org/10.1088/1367-2630/ac2921.

[7] Schütze, F., Doyle, L., Schreiber, J., Zepf, M. & Karbstein, F. Dark-field setup for the measurement of light-by-light scattering with high-intensity lasers. *Phys. Rev. D* **109**, 096009 (2024). https://link.aps.org/doi/10.1103/PhysRevD.109.096009.

[8] Picksley, A. *et al.* Matched guiding and controlled injection in dark-current-free, 10-gev-class, channel-guided laser-plasma accelerators. *Physical Review Letters* **133**, 255001 (2024). https://link.aps.org/doi/10.1103/PhysRevLett.133.255001.

[9] Veksler, V. I. Coherent principle of acceleration of charged particles. In *Proceedings of the CERN Symposium on High-Energy Accelerators and Pion Physics*, 80–83 (CERN, 1956). https://cds.cern.ch/record/1241563/files/p80.pdf.

[10] Snavely, R. A. *et al.* Intense high-energy proton beams from petawatt-laser irradiation of solids. *Physical Review Letters* **85**, 2945–2948 (2000). https://link.aps.org/doi/10.1103/PhysRevLett.85.2945.

[11] Clark, E. L. *et al.* Energetic heavy-ion and proton generation from ultraintense laser-plasma interactions with solids. *Physical Review Letters* **85**, 1654–1657 (2000). https://link.aps.org/doi/10.1103/PhysRevLett.85.1654.

[12] Daido, H., Nishiuchi, M. & Pirozhkov, A. S. Review of laser-driven ion sources and their applications. *Reports on Progress in Physics* **75**, 056401 (2012). https://dx.doi.org/10.1088/0034-4885/75/5/056401.

[13] Macchi, A., Borghesi, M. & Passoni, M. Ion acceleration by superintense laser-plasma interaction. *Reviews of Modern Physics* **85**, 751–793 (2013). https://doi.org/10.1103/RevModPhys.85.751.

[14] Bolton, P. R., Parodi, K. & Schreiber, J. *Applications of Laser-driven Particle Acceleration* (Taylor and Francis Group). https://doi.org/10.1201/9780429445101.

[15] Lindner, F. *Laser-driven heavy ion acceleration.* Ph.D. thesis, Ludwig-Maximilians-Universität München (2021). https://edoc.ub.uni-muenchen.de/27632/.

[16] Habs, D. *et al.* Introducing the fission-fusion reaction process: Using a laser-accelerated Th beam to produce neutron-rich nuclei towards the N=126 waiting point of the r-process. *Applied Physics B: Lasers and Optics* **103**, 471–484 (2011). http://link.springer.com/10.1007/s00340-010-4261-x.

[17] Olive, K. A. & Skillman, E. D. A realistic determination of the error on the primordial helium abundance: Steps toward nonparametric nebular helium abundances. *The Astrophysical Journal* **617**, 29 (2004). https://dx.doi.org/10.1086/425170.

[18] Horowitz, C. J. *et al.* r -process nucleosynthesis: connecting rare-isotope beam facilities with the cosmos. *Journal of Physics G: Nuclear and Particle Physics* **46**, 083001 (2019). https://iopscience.iop.org/article/10.1088/1361-6471/ab0849.

[19] Burbidge, E. M., Burbidge, G. R., Fowler, W. A. & Hoyle, F. Synthesis of the elements in stars. *Rev. Mod. Phys.* **29**, 547–650 (1957). https://link.aps.org/doi/10.1103/RevModPhys.29.547.

[20] Mumpower, M., Surman, R., McLaughlin, G. & Aprahamian, A. The impact of individual nuclear properties on r-process nucleosynthesis. *Progress in Particle and Nuclear Physics* **86**, 86–126 (2016). https://www.sciencedirect.com/science/article/pii/S0146641015000897.

[21] Abbott, B. P. *et al.* Gw170817: Observation of gravitational waves from a binary neutron star inspiral. *Physical Review Letters* **119**, 161101 (2017). https://link.aps.org/doi/10.1103/PhysRevLett.119.161101.

[22] Pian, E. *et al.* Spectroscopic identification of r-process nucleosynthesis in a double neutron-star merger. *Nature* **551**, 67–70 (2017). http://dx.doi.org/10.1038/nature24298.

[23] Cowan, J. J. *et al.* Origin of the heaviest elements: The rapid neutron-capture process. *Rev. Mod. Phys.* **93**, 015002 (2021). https://link.aps.org/doi/10.1103/RevModPhys.93.015002.

[24] Blaum, K. High-accuracy mass spectrometry with stored ions. *Physics Reports* **425**, 1–78 (2006). https://www.sciencedirect.com/science/article/pii/S0370157305004643.

[25] Baruah, S. *et al.* Mass measurements beyond the major r-process waiting point Zn80. *Physical Review Letters* **101**, 1–4 (2008). https://doi.org/10.1103/PhysRevLett.101.262501.

[26] Dworschak, M. *et al.* Restoration of the N=82 shell gap from direct mass measurements of Sn132,134. *Physical Review Letters* **100**, 12–15 (2008). https://doi.org/10.1103/PhysRevLett.100.072501.

[27] Dillmann, I. *et al.* $n = 82$ shell quenching of the classical r-process "waiting-point" nucleus ^{130}Cd. *Physical Review Letters* **91**, 162503 (2003). https://link.aps.org/doi/10.1103/PhysRevLett.91.162503.

[28] Bollen, G. FRIB—Facility for Rare Isotope Beams. *AIP Conference Proceedings* **1224**, 432–441 (2010). https://doi.org/10.1063/1.3431449.

[29] Okuno, H., Fukunishi, N. & Kamigaito, O. Progress of ribf accelerators. *Progress of Theoretical and Experimental Physics* **2012**, 03C002 (2012). https://doi.org/10.1093/ptep/pts046.

[30] Gutbrod, H. H., Augustin, I., Eickhoff, H. & Groß, K. D. t. *FAIR-Baseline technical report* (2006). https://www.osti.gov/etdeweb/biblio/20865458.

[31] Lindner, F. H. *et al.* Charge-state resolved laser acceleration of gold ions to beyond 7 MeV/u. *Scientific Reports* **12**, 1–11 (2022). https://doi.org/10.1038/s41598-022-08556-8.

[32] Möller, P., Sierk, A. J., Ichikawa, T., Iwamoto, A. & Mumpower, M. Fission barriers at the end of the chart of the nuclides. *Phys. Rev. C* **91**, 024310 (2015). https://link.aps.org/doi/10.1103/PhysRevC.91.024310.

[33] Afshari, M. *et al.* The role of collisional ionization in heavy ion acceleration by high intensity laser pulses. *Scientific Reports* **12**, 1–8 (2022). https://doi.org/10.1038/s41598-022-23148-2.

[34] Mainfray, G. & Manus, G. Multiphoton ionization of atoms. *Reports on Progress in Physics* **54**, 1333 (1991). https://dx.doi.org/10.1088/0034-4885/54/10/002.

[35] Chen, F. *Introduction to Plasma Physics and Controlled Fusion* (Springer International Publishing, 2016), 3rd edn.

[36] Gibbon, P. *Short Pulse Laser Interactions with Matter* (Published by Imperial College Press and distributed by World Scientific Publishing Co.).

[37] Wilks, S. C., Kruer, W. L., Tabak, M. & Langdon, A. B. Absorption of Ultra-Intense Laser Pulses. *Physical Review Letters* **69**, 1383–1386 (1992). https://doi.org/10.1103/PhysRevLett.69.1383.

[38] Wickens, L. M., Allen, J. E. & Rumsby, P. T. Ion emission from laser-produced plasmas with two electron temperatures. *Physical Review Letters* **41**, 243–246 (1978). https://link.aps.org/doi/10.1103/PhysRevLett.41.243.

[39] Wilks, S. C. *et al.* Energetic proton generation in ultra-intense laser-solid interactions. *Physics of Plasmas* **8**, 542–549 (2001). https://doi.org/10.1063/1.1333697.

[40] Lindgren, K. & Jonsson, G. High-energy (γ, xn) reactions in 197-Au. *Nuclear Physics A* **166**, 643–660 (1971). https://www.sciencedirect.com/science/article/pii/0375947471909110.

[41] Stoyer, M. A. *et al.* Nuclear diagnostics for petawatt experiments. *Review of Scientific Instruments* **72**, 767–772 (2001). https://doi.org/10.1063/1.1319355.

[42] Maksimchuk, A., Gu, S., Flippo, K., Umstadter, D. & Bychenkov, V. Y. Forward ion acceleration in thin films driven by a high-intensity laser. *Physical Review Letters* **84**, 4108–4111 (2000). https://link.aps.org/doi/10.1103/PhysRevLett.84.4108.

[43] Mackinnon, A. J. *et al.* Enhancement of proton acceleration by hot-electron recirculation in thin foils irradiated by ultraintense laser pulses. *Physical Review Letters* **88**, 215006 (2002). https://link.aps.org/doi/10.1103/PhysRevLett.88.215006.

[44] Mora, P. Plasma expansion into a vacuum. *Physical Review Letters* **90**, 185002 (2003). https://link.aps.org/doi/10.1103/PhysRevLett.90.185002.

[45] Fuchs, J. *et al.* Laser-driven proton scaling laws and new paths towards energy increase. *Nature Physics* **2**, 48–54 (2006). https://doi.org/10.1038/nphys199.

[46] Schreiber, J. *et al.* Analytical model for ion acceleration by high-intensity laser pulses. *Physical Review Letters* **97**, 045005 (2006). https://link.aps.org/doi/10.1103/PhysRevLett.97.045005.

[47] Esirkepov, T., Borghesi, M., Bulanov, S. V., Mourou, G. & Tajima, T. Highly efficient relativistic-ion generation in the laser-piston regime. *Physical Review Letters* **92**, 175003 (2004). https://journals.aps.org/prl/abstract/10.1103/PhysRevLett.92.175003.

[48] Esirkepov, T., Yamagiwa, M. & Tajima, T. Laser ion-acceleration scaling laws seen in multiparametric particle-in-cell simulations. *Physical Review Letters* **96**, 105001 (2006). https://link.aps.org/doi/10.1103/PhysRevLett.96.105001.

[49] Brantov, A. V., Govras, E. A., Kovalev, V. F. & Bychenkov, V. Y. Synchronized ion acceleration by ultraintense slow light. *Physical Review Letters* **116**, 085004 (2016). https://link.aps.org/doi/10.1103/PhysRevLett.116.085004.

[50] Göthel, I. *et al.* Optimized laser ion acceleration at the relativistic critical density surface. *Plasma Physics and Controlled Fusion* **64**, 044010 (2022). https://dx.doi.org/10.1088/1361-6587/ac4e9f.

[51] Haberberger, D. *et al.* Collisionless shocks in laser-produced plasma generate monoenergetic high-energy proton beams. *Nature Physics* **8**, 95–99 (2012). https://www.nature.com/articles/nphys2130.

[52] Henig, A. *et al.* Radiation-pressure acceleration of ion beams driven by circularly polarized laser pulses. *Physical Review Letters* **103**, 245003 (2009). https://link.aps.org/doi/10.1103/PhysRevLett.103.245003.

[53] Ziegler, T. *et al.* Laser-driven high-energy proton beams from cascaded acceleration regimes. *Nature Physics* **20**, 1211–1216 (2024). https://www.nature.com/articles/s41567-024-02505-0.

[54] Bethe, H. Zur Theorie des Durchgangs schneller Korpuskularstrahlen durch Materie. *Annalen der Physik* **397**, 325–400 (1930). https://onlinelibrary.wiley.com/doi/abs/10.1002/andp.19303970303.

[55] Navas, S. *et al.* Review of particle physics. *Physical Review D* **110**, 030001 (2024). https://pdg.lbl.gov/2022/reviews/rpp2022-rev-passage-particles-matter.pdf.

[56] Lindhard, J., Scharff, M. & tt, H. E. S. Range Concepts and Heavy Ion Ranges (Notes on Atomic Collisions, II). *Mat. Fys. Medd. Dan. Vid. Selsk.* **33**, 1–42 (1963). https://www.osti.gov/biblio/4153115.

[57] Ichimaru, S. *Basic Principles of Plasma Physics, A statistical aproach.* Frontiers in Physics (W. A. Benjamin, Inc., 1973), 1 edn.

[58] Wu, H.-C., Tajima, T., Habs, D., Chao, A. W. & Meyer-ter Vehn, J. Collective deceleration: Toward a compact beam dump. *Physical Review Accelerators and Beams* **13**, 101303 (2010). https://link.aps.org/doi/10.1103/PhysRevSTAB.13.101303.

[59] Ziegler, J. F., Ziegler, M. D. & Biersack, J. P. SRIM - The stopping and range of ions in matter (2010). *Nuclear Instruments and Methods in Physics Research, Section B: Beam Interactions with Materials and Atoms* **268**, 1818–1823 (2010). http://dx.doi.org/10.1016/j.nimb.2010.02.091.

[60] Blatt, J. M. & Weisskopf, V. F. *Theoretical Nuclear Physics* (John Wiley and Sons, New York, 1952).

[61] Bohr, N. & Wheeler, J. A. The mechanism of nuclear fission. *Phys. Rev.* **56**, 426–450 (1939). https://link.aps.org/doi/10.1103/PhysRev.56.426.

[62] Green, A. E. S. Coulomb radius constant from nuclear masses. *Phys. Rev.* **95**, 1006–1009 (1954). https://link.aps.org/doi/10.1103/PhysRev.95.1006.

[63] Vandenbosch, R. & Huizenga, J. R. *Nuclear fission* (Academic Press, Inc., New York, 1973). https://www.osti.gov/biblio/4359815.

[64] Hahn, O. & Strassmann, F. Über den Nachweis und das Verhalten der bei der Bestrahlung des Urans mittels Neutronen entstehenden Erdalkalimetalle. *Naturwissenschaften* **27**, 11–15 (1939). https://doi.org/10.1007/BF01488241.

[65] Hahn, O. & Strassmann, F. Nachweis der Entstehung aktiver Bariumisotope aus Uran und Thorium durch Neutronenbestrahlung; Nachweis weiterer aktiver Bruchstücke bei der Uranspaltung. *Naturwissenschaften* **27**, 89–95 (1939). https://link.springer.com/article/10.1007/BF01488988.

[66] Meitner, L. & Frisch, O. R. Disintegration of Uranium by Neutrons: a New Type of Nuclear Reaction. *Nature* **143**, 239–240 (1939). https://doi.org/10.1038/143239a0.

[67] Meitner, L. & Frisch, O. R. Products of the Fission of the Uranium Nucleus. *Nature* **143**, 471–472 (1939). https://www.nature.com/articles/143471a0.

[68] Haxby, R. O., Shoupp, W. E., Stephens, W. E. & Wells, W. H. Photo-fission of uranium and thorium. *Physical Review* **58**, 92–92 (1940). https://link.aps.org/doi/10.1103/PhysRev.58.92.

[69] Haxby, R. O., Shoupp, W. E., Stephens, W. E. & Wells, W. H. Photo-fission of uranium and thorium. *Physical Review* **59**, 57–62 (1941). https://link.aps.org/doi/10.1103/PhysRev.59.57.

[70] Goldhaber, M. & Teller, E. On nuclear dipole vibrations. *Physical Review* **74**, 1046–1049 (1948). https://doi.org/10.1103/PhysRev.74.1046.

[71] Speth, J. & van der Woude, A. Giant resonances in nuclei. *Reports on Progress in Physics* **44**, 719 (1981). https://dx.doi.org/10.1088/0034-4885/44/7/002.

[72] Bass, R. Fusion of heavy nuclei in a classical model. *Nuclear Physics, Section A* **231**, 45–63 (1974). https://doi.org/10.1016/0375-9474(74)90292-9.

[73] Bock, R. *et al.* Dynamics of intermediate-energy heavy-ion collisions: The phenomenon of quasi-fission. *Nucl. Phys. A* **388**, 334–350 (1982). https://doi.org/10.1016/0375-9474(82)90569-3.

[74] Hinde, D. J. *et al.* Dynamics of nuclear fusion: Quasi-fission and the transition from compound nucleus formation to deep-inelastic scattering. *Phys. Rev. C* **53**, 1290–1300 (1996). https://doi.org/10.1103/PhysRevC.53.1290.

[75] Back, B. B., Esbensen, H., Jiang, C. L. & Rehm, K. E. Recent developments in heavy-ion fusion reactions. *Rev. Mod. Phys.* **86**, 317–360 (2014). https://doi.org/10.1103/RevModPhys.86.317.

[76] Lindner, F. H. *et al.* Towards swift ion bunch acceleration by high-power laser pulses at the Centre for Advanced Laser Applications (CALA). *Nuclear Instruments and Methods in Physics Research, Section B: Beam Interactions with Materials and Atoms* **402**, 354–357 (2017). http://dx.doi.org/10.1016/j.nimb.2017.02.088.

[77] Gavron, A. Statistical model calculations in heavy ion reactions. *Physical Review C* **21**, 230–236 (1980). https://doi.org/10.1103/PhysRevC.21.230.

[78] Tarasov, O. B. & Bazin, D. Development of the program LISE: Application to fusion-evaporation. *Nuclear Instruments and Methods in Physics Research Section B: Beam Interactions with Materials and Atoms* **204**, 174–178 (2003). https://doi.org/10.1016/S0168-583X(02)01917-1.

[79] Tarasov, O. B. & Bazin, D. LISE++: Design your own spectrometer. *Nuclear Physics A* **746**, 411–414 (2004). https://doi.org/10.1016/j.nuclphysa.2004.09.063.

[80] Fitzpatrick, E.-G. PhD thesis, Ludwig-Maximilians-Universität, work in progress .

[81] Foerster, F. *Hybrid Wakefield Acceleration A Source of Stable and High-Density Electron Beams München.* Ph.D. thesis, Ludwig-Maximilians-Universität (2024). https://edoc.ub.uni-muenchen.de/34651/.

[82] Hartmann, J. *Quantitative Ion Spectrometry and first laser-ion acceleration results at the Centre for Advanced Laser Applications.* Ph.D. thesis, Ludwig-Maximilians-Universität München (2022). https://edoc.ub.uni-muenchen.de/31226/1/Hartmann_Jens.pdf.

[83] Doyle, L. *Implementation of an Adaptive Optics System for Focus Optimization at the Centre for Advanced Laser Applications*. Master's thesis, Ludwig-Maximilians-Universität (2019).

[84] Weiße, N. *et al.* Tango Controls and data pipeline for petawatt laser experiments. *High Power Laser Science and Engineering* **11**, e44 (2023). https://www.cambridge.org/core/product/identifier/S2095471923000178/type/journal_article.

[85] Guo, R. *Transmission Diagnostic of High-intensity Short Laser Pulses for Ion Acceleration* . Master's thesis, Ludwig-Maximilians-Universität (2024).

[86] Magin, V. X. K. *Commissioning of the nano-Foil Target Positioning System*. Bachelor's thesis, Ludwig-Maximilians-Universität München (2023).

[87] SYRUSpro series (2025). Accessed on 04.09.2025, https://www.buhlergroup.com/global/de/products/syruspro_series_precisionopticsvacuumcoater.html.

[88] Goodfellow GmbH. Gold foil specifications (2025). Accessed on 06.09.2025, https://docs.rs-online.com/873d/A700000014144095.pdf.

[89] Bohr, N. I. On the constitution of atoms and molecules . *The London, Edinburgh, and Dublin Philosophical Magazine and Journal of Science* **26**, 1–25 (1913). https://doi.org/10.1080/14786441308634955.

[90] Uo, M., Wada, T. & Sugiyama, T. Applications of x-ray fluorescence analysis (xrf) to dental and medical specimens. *Japanese Dental Science Review* **51**, 2–9 (2015). https://www.sciencedirect.com/science/article/pii/S1882761614000258.

[91] Thompson, A. C. *et al. X-RAY DATA BOOKLET* (Center for X-ray Optics and Advanced Light Source, Lawrence Berkeley National Laboratory, October 2009), 3 edn. http://xdb.lbl.gov/.

[92] Gasdia-Cochrane, M. Technology Focus: X-ray Fluorescence (XRF) in Mining (21.02.2024). Accessed on 17.08.2025, https://www.thermofisher.com/blog/mining/technology-focus-x-ray-fluorescence-xrf-in-mining/.

[93] Thomson, J. XXVI. rays of positive electricity. *The London, Edinburgh, and Dublin Philosophical Magazine and Journal of Science* **21**, 225–249 (1911). https://doi.org/10.1080/14786440208637024.

[94] Bolton, P. R. *et al.* Instrumentation for diagnostics and control of laser-accelerated proton (ion) beams. *Physica Medica* **30**, 255–270 (2014). http://dx.doi.org/10.1016/j.ejmp.2013.09.002.

[95] Schillaci, F. *et al.* Calibration and energy resolution study of a high dispersive power Thomson Parabola Spectrometer with monochromatic proton beams. *Journal of Instrumentation* **9**, T10003 (2014). https://doi.org/10.1088/1748-0221/9/10/T10003.

[96] Ponnath, L. *Development of Diagnostics Components for Laser-Accelerated Heavy Ions.* Master's thesis, Ludwig-Maximilians-Universität München (2018).

[97] Jung, D. *et al.* Development of a high resolution and high dispersion Thomson parabola. *Review of Scientific Instruments* **82**, 013301 (2011). https://doi.org/10.1063/1.3523428.

[98] Dassault Systèmes. CST Studio Suite 2024. https://www.3ds.com/products-services/simulia/products/cst-studio-suite/ (2024).

[99] Doyle, L. Physicsbox. https://gitlab.lrz.de/cala-public/packages/physicsbox.

[100] Hairer, E., Norsett, S. P. & Wanner, G. *Solving Ordinary Differential Equations i. Nonstiff Problems* (Springer-Verlag, 1993), 2nd edn.

[101] Wang, P. *et al.* Super-heavy ions acceleration driven by ultrashort laser pulses at ultrahigh intensity. *Physical Review X* **11**, 021049 (2021). https://link.aps.org/doi/10.1103/PhysRevX.11.021049.

[102] Reinhardt, S., Draxinger, W., Schreiber, J. & Assmann, W. A pixel detector system for laser-accelerated ion detection. *Journal of Instrumentation* **8**, P03008 (2013). https://doi.org/10.1088/1748-0221/8/03/P03008.

[103] Fleischer, R. L., Price, P. B. & Walker, R. M. Ion explosion spike mechanism for formation of charged-particle tracks in solids. *Journal of Applied Physics* **36**, 3645–3652 (1965). https://doi.org/10.1063/1.1703059.

[104] Hegelich, B. M. *Acceleration of heavy Ions to MeV/nucleon Energies by Ultrahigh-Intensity Lasers.* Ph.D. thesis, Ludwig-Maximilians-Universität München (2002).

[105] Cartwright, B., Shirk, E. & Price, P. A nuclear-track-recording polymer of unique sensitivity and resolution. *Nuclear Instruments and Methods* **153**, 457–460 (1978). https://www.sciencedirect.com/science/article/pii/0029554X78909898.

[106] Schollmeier, M. S. *et al.* Differentiating multi-MeV, multi-ion spectra with CR-39 solid-state nuclear track detectors. *Scientific Reports* **13**, 18155 (2023). https://www.nature.com/articles/s41598-023-45208-x.

[107] Track Analysis Systems Ltd. (TASL). Accessed on 22.05.2025, https://www.tasl.co.uk/.

[108] ELBEK-Bildanalyse GmbH. SAMAICA V2.0 User's Manual (2002). Available via local drive on Cala_hf/Manuals.

[109] Adams, J. H. Automated track measurements in CR-39. *Nuclear Tracks* **4**, 67–76 (1980). https://www.sciencedirect.com/science/article/pii/0191278X80900165.

[110] Buck, A. *et al.* Absolute charge calibration of scintillating screens for relativistic electron detection. *Review of Scientific Instruments* **81**, 033110 (2010). https://doi.org/10.1063/1.3310275.

[111] Kurz, T. *et al.* Calibration and cross-laboratory implementation of scintillating screens for electron bunch charge determination. *Review of Scientific Instruments* **89**, 093303 (2018). http://aip.scitation.org/doi/10.1063/1.5041755.

[112] Green, J. S. *et al.* Scintillator-based ion beam profiler for diagnosing laser-accelerated ion beams. In *Laser Acceleration of Electrons, Protons, and Ions; and Medical Applications of Laser-Generated Secondary Sources of Radiation and Particles*, vol. 8079, 807919 (SPIE, 2011).

[113] Metzkes, J. *et al.* A scintillator-based online detector for the angularly resolved measurement of laser-accelerated proton spectra. *Review of Scientific Instruments* **83**, 123301 (2012). https://doi.org/10.1063/1.4768672.

[114] Xu, M. H. *et al.* Development of a real-time ion spectrometer with a scintillator for laser-driven ion acceleration experiments. *Chinese Physics Letters* **28** (2011).

[115] Cawo Solutions. Blue-emitting screens (2022). Accessed on 19.07.2025, https://www.cawo.com/products/intensifying-screens/blue-emitting/.

[116] MCI Optonic, LLC. Drz screens (2025). Accessed on 19.07.2025, http://www.mcio.com/Products/drz-screens.aspx.

[117] Schilz, J. D. *et al.* Absolute energy-dependent scintillating screen calibration for real-time detection of laser-accelerated proton bunches. *Review of Scientific Instruments* **95**, 073302 (2024). https://doi.org/10.1063/5.0206931.

[118] Schwinkendorf, J.-P. *et al.* Charge calibration of drz scintillation phosphor screens. *Journal of Instrumentation* **14**, P09025–P09025 (2019). https://iopscience.iop.org/article/10.1088/1748-0221/14/09/P09025.

[119] Teledyne Princton Instruments. Kuro Back-illuminated scientific CMOS cameras datasheet. Accessed on 23.05.2025, https://www.mtb.es/files/products/KURO_datasheet_all_models_sch_07222021.pdf.

[120] Tamron. Zoom Objective Datasheet. Accessed on 23.05.2025, https://www.tamron.eu/de-DE/p/502cb513-2c32-46c3-84c4-0c41eaf72a50/sp-24-70mm-f28-di-vc-usd-g2.

[121] Eljen Technology. Specifications of EJ-200 scintillator. Accessed on 26.05.2025, https://eljentechnology.com/products/plastic-scintillators/ej-200-ej-204-ej-208-ej-212.

[122] ISDI Ltd. *CMOS image sensor, PS Series, 50 µm pixel.* https://static1.squarespace.com/static/589056c437c5811e7fccde6d/t/61ee9bca8368c17d1f5d6c22/1643027438471/PS+50um+product+brief+1_5.pdf.

[123] Knoll, G. F. *Radiation Detection and Measurement* (John Wiley & Sons, New York, 2010), 4 edn.

[124] Wang, X. *et al.* Medical Imaging 2011: Physics of Medical Imaging. In *Proceedings of SPIE – Medical Imaging 2011: Physics of Medical Imaging*, vol. 7961, 79611V (SPIE, Orlando, FL, 2011). https://doi.org/10.1117/12.877469.

[125] Lécz, Z., Budai, J., Andreev, A. & Ter-Avetisyan, S. Thickness of natural contaminant layers on metal surfaces and its effects on laser-driven ion acceleration. *Physics of Plasmas* **27** (2020). https://pubs.aip.org/pop/article/27/1/013105/262945/Thickness-of-natural-contaminant-layers-on-metal.

[126] Hegelich, M. *et al.* MeV ion jets from short-pulse-laser interaction with thin foils. *Physical Review Letters* **89**, 085002/1–085002/4 (2002). https://doi.org/10.1103/PhysRevLett.89.085002.

[127] Zepf, M. *et al.* Proton acceleration from high-intensity laser interactions with thin foil targets. *Physical Review Letters* **90**, 064801 (2003). https://link.aps.org/doi/10.1103/PhysRevLett.90.064801.

[128] McKenna, P. *et al.* Effect of target heating on ion-induced reactions in high-intensity laser-plasma interactions. *Applied Physics Letters* **83**, 2763–2765 (2003). https://doi.org/10.1063/1.1616972.

[129] Martinez, M. *et al.* The Texas Petawatt Laser. In *Proceedings Volume 5991, Laser-Induced Damage in Optical Materials: 2005; 59911N* (Boulder Damage Symposium XXXVII: Annual Symposium on Optical Materials for High Power Lasers, Boulder, CO, United Stated, 2006). https://doi.org/10.1117/12.638939.

[130] Bagnoud, V. *et al.* Commissioning and early experiments of the PHELIX facility. *Applied Physics B: Lasers and Optics* **100**, 137–150 (2010). https://doi.org/10.1007/s00340-009-3855-7.

[131] Weiser, M. *Development of a Spectroscopic Real Time Temperature Diagnostic for Laser Heated Thin Gold Foils.* Master's thesis, Ludwig-Maximilians-Universität München (2021).

[132] Kratzer, V. *Enhancing the Efficiency of Laser-Based Heavy Ion Acceleration by Radiative Target Heating.* Master's thesis, Ludwig-Maximilians-Universität (2024).

[133] Planck, M. Ueber irreversible Strahlungsvorgänge. *Annalen der Physik* **306**, 69–122 (1900). https://onlinelibrary.wiley.com/doi/abs/10.1002/andp.19003060105.

[134] Planck, M. Ueber das Gesetz der Energieverteilung im Normalspectrum. *Annalen der Physik* **309**, 553–563 (1901). https://onlinelibrary.wiley.com/doi/abs/10.1002/andp.19013090310.

[135] Howell, J. R., Mengüç, M. P. & Siegel, R. *Thermal Radiation Heat Transfer* (CRC Press, Boca Raton, FL, 2010), 5 edn.

[136] Worthing, A. G. Spectral emissivities of tantalum, platinum, nickel and gold as a function of temperature, and the melting point of tantalum. *Physical Review* **28**, 174–189 (1926). https://doi.org/10.1103/PhysRev.28.174.

[137] Zhu, C., Hobbs, M. J. & Willmott, J. R. An accurate instrument for emissivity measurements by direct and indirect methods. *Measurement Science and Technology* **31**, 044007 (2020). https://doi.org/10.1088/1361-6501/ab5e9b.

[138] Novanta Photonics. Opus 532 with MPC6000 User Manual. Accessed on 14.09.2025, https://novantaphotonics.com/product/opus-solid-state-continuous-wave-lasers/.

[139] Mitutoyo Corporation. Long working distance objectives. Accessed on 14.09.2025, https://shop.mitutoyo.de/web/mitutoyo/en_DE/mitutoyo/\protect\T1\textdollarcatalogue/mitutoyoData/PR/378-867-5/datasheet.xhtml.

[140] Ocean Insight. *NIRQuest, Scientific-grade Spectrometer, Installation and Operation Manual*. Accessed on 10.09.2025, https://www.oceanoptics.com/wp-content/uploads/2024/05/MNL-1002-NIRQuest-UserManual-Rev-C-1.pdf.

[141] Blaber, M. G., Ford, M. J. & Cortie, M. B. *The Physics and Optical Properties of Gold*, 481–508 (CRC Press, 2009). http://hdl.handle.net/10453/14248.

[142] Hesse, M. *et al.* Spatially resolved online particle detector using scintillators for laser-driven particle sources. *Review of Scientific Instruments* **92**, 093302 (2021). https://doi.org/10.1063/5.0052507.

[143] Scuderi, V. *et al.* TOF diagnosis of laser accelerated, high-energy protons. *Nuclear Instruments and Methods in Physics Research Section A* **978**, 164364 (2020). https://doi.org/10.1016/j.nima.2020.164364.

[144] Kroll, F. *et al.* Tumour irradiation in mice with a laser-accelerated proton beam. *Nature Physics* **18**, 316–322 (2022). https://doi.org/10.1038/s41567-022-01520-3.

[145] Geulig, L. D. *et al.* Online charge measurement for petawatt laser-driven ion acceleration. *Review of Scientific Instruments* **93**, 103301 (2022). https://doi.org/10.1063/5.0096423.

[146] Gerlach, S. *et al.* Three-dimensional acoustic monitoring of laser-accelerated protons in the focus of a pulsed-power solenoid lens. *High Power Laser Science and Engineering* **11**, e38 (2023). https://doi.org/10.1017/hpl.2023.16.

[147] Harres, K. *et al.* Development and calibration of a Thomson parabola with microchannel plate for the detection of laser-accelerated MeV ions. *Review of Scientific Instruments* **79**, 093301 (2008). https://doi.org/10.1063/1.2987687.

[148] Gershman, D. J. *et al.* Extending the dynamic range of microchannel plate detectors using charge-integration-based counting. *Review of Scientific Instruments* **89**, 073301 (2018). https://doi.org/10.1063/1.5027376.

[149] Hsu, M.-Y. *Implementation of a Monitor for Electromagnetic Pulses at the High-Fields Cave of the Center for Advanced Laser Applications (CALA).* Bachelor's thesis, Ludwig-Maximilians-Universität (2023).

[150] Hollinger, R. *et al.* Extreme ionization of heavy atoms in solid-density plasmas by relativistic second-harmonic laser pulses. *Nature Photonics* **14**, 607–611 (2020). http://dx.doi.org/10.1038/s41566-020-0666-1.

[151] Morris, S. *et al.* Recombination effects in laser-driven acceleration of heavy ions. *Physical Review E* **111**, 65209 (2025). https://doi.org/10.1103/PhysRevE.111.065209.

[152] Hartmann, J. *et al.* The spatial contrast challenge for intense laser-plasma experiments. *Journal of Physics: Conference Series* **1079** (2018). https://doi.org/10.1088/1742-6596/1079/1/012003.

[153] Weiser, M. FocusAnalysis. https://gitlab.lrz.de/cala-internal/hf/wip/-/tree/main/Scripts/FocusAnalysis?ref_type=heads.

[154] Schäfer, P. *Attenuation of a Petawatt Class Laser System.* Bachelor's thesis, Ludwig-Maximilians-Universität (2024).

[155] Braenzel, J. *et al.* Coulomb-driven energy boost of heavy ions for laser-plasma acceleration. *Physical Review Letters* **114**, 124801 (2015). https://link.aps.org/doi/10.1103/PhysRevLett.114.124801.

[156] Bangs Laboratories, Inc. Material Properties of Polystyrene and Poly(methul methacrylate) (PMMA) Microspheres. Accessed

on 28.04.2015, https://bangslabs.com/wp-content/uploads/BLI.TSD-0021-Material-Properties-Web.pdf.

[157] Midland Plastics, Inc. AcrylicPolymethul Methacrylate (PMMA). Accessed on 23.07.2025, https://www.google.com/url?sa=t&source=web&rct=j&opi=89978449&url=https://midlandplastics.com/download_file/force/85/201&ved=2ahUKEwjK-rXdv9mPAxU32wIHHU46KqcQFnoECBsQAQ&usg=AOvVaw2K3df1ajreEbceFWVg5w73.

[158] BCE Special Ceramics GmbH. Material characteristics, Alumina ceramics A-997. Accessed on 23.07.2025, https://www.bce-special-ceramics.com/wp-content/uploads/2016/11/A_997.pdf.

[159] Thermo Fischer Scientific. Thermo Scientific Niton XL3t GOLD XRF Analyzer (2013). https://assets.thermofisher.com/TFS-Assets/CAD/Specification-Sheets/Niton-XL3t-GOLDD-Spec-Sheet-2013Jan15.pdf.

[160] Kramida, A., Olsen, K. & Ralchenko, Y. Periodic Table of Elements (June 2024). Accessed on 14.05.2025, https://www.nist.gov/pml/periodic-table-elements.

[161] Thirolf, P. G. & Habs, D. Bright perspectives for nuclear photonics. *European Physical Journal: Special Topics* **223**, 1213–1219 (2014). https://doi.org/10.1140/epjst/e2014-02175-1.

[162] Qi, J., Fu, L. & Wang, X. Nuclear fission in intense laser fields. *Physical Review C* **102**, 1–7 (2020). 2008.03498.

[163] Davydovska, O. I., Denisov, V. Y. & Sedykh, I. Y. Evaluation of the fission barrier values using the experimental values of the ratio $\Gamma_{\mathrm{f}}(E)/\Gamma_{\mathrm{n}}(E)$. *Physical Review C* **105**, 1–8 (2022). https://doi.org/10.1103/PhysRevC.105.014620.

[164] Norreys, P. A. *et al.* Neutron production from picosecond laser irradiation of deuterated targets at intensities of. *Plasma Physics and Controlled Fusion* **40**, 175 (1998). https://dx.doi.org/10.1088/0741-3335/40/2/001.

[165] Ditmire, T. *et al.* Nuclear fusion from explosions of femtosecond laser-heated deuterium clusters. *Nature* **398**, 489–492 (1999). https://www.nature.com/articles/19037.

[166] Tanaka, K. A. *et al.* Studies of ultra-intense laser plasma interactions for fast ignition. *Physics of Plasmas* **7**, 2014–2022 (2000). https://doi.org/10.1063/1.874023.

[167] Zimmer, M. *et al.* Demonstration of non-destructive and isotope-sensitive material analysis using a short-pulsed laser-driven epi-thermal neutron source. *Nature Communications* **13**, 1173 (2022). https://www.nature.com/articles/s41467-022-28756-0.

[168] Schuh, A. *et al.* Discovery of the gold isotopes. *Atomic Data and Nuclear Data Tables* **96**, 307–314 (2010). https://www.sciencedirect.com/science/article/pii/S0092640X09000862.

[169] Boyer, K., Luk, T. S. & Rhodes, C. K. Possibility of optically induced nuclear fission. *Physical Review Letters* **60**, 557–560 (1988). https://doi.org/10.1103/PhysRevLett.60.557.

[170] Ledingham, K. W. D. *et al.* Photonuclear Physics when a Multiterawatt Laser Pulse Interacts with Solid Targets 899 (2000). https://doi.org/10.1103/PhysRevLett.84.899.

[171] Cowan, T. E. *et al.* Photonuclear Fission from High Energy Electrons from Ultraintense Laser-Solid Interactions. *Physical Review Letters* **84**, 903 (2000). https://doi.org/10.1103/PhysRevLett.84.903.

[172] Kalla, R. *et al.* On-shot detection of fission isotopes of 238U, produced by laser-driven x-rays. *Physics of Plasmas* **32**, 073106 (2025). https://doi.org/10.1063/5.0251735.

[173] Schwoerer, H. *et al.* Fission of actinides using a tabletop laser. *Europhysics Letters* **61**, 47–52 (2003). https://doi.org/10.1209/epl/i2003-00243-1.

[174] Arruda-Neto, J. D. T. *et al.* Observation of pion-related effects in the photofission of preactinide nuclei **48**, 1594 (1993). https://doi.org/10.1103/PhysRevC.48.1594.

[175] Martins, J. B. *et al.* Absolute photofission cross section of ^{197}Au, ^{nat}Pb, ^{209}Bi, ^{232}Th, ^{238}U, and ^{235}U nuclei by 69-MeV monochromatic and polarized photons. *Physical Review C* **44**, 354–364 (1991). https://doi.org/10.1103/PhysRevC.44.354.

[176] Lucherini, V. *et al.* Au photofission cross section by quasimonochromatic photons in the intermediate energy region. *Physical Review C* **39**, 911 (1989). https://doi.org/10.1103/PhysRevC.39.911.

[177] Tavana, P. *et al.* Ultra-high efficiency bremsstrahlung production in the interaction of direct laser-accelerated electrons with high-Z material. *Frontiers in Physics* **11** (2023). https://doi.org/10.3389/fphy.2023.1178967.

[178] Afshari, M. Private communication (2025).

[179] Schreiber, J. *et al.* Source-size measurements and charge distributions of ions accelerated from thin foils irradiated by high-intensity laser pulses. In *Applied Physics B*, vol. 79, 1041–1045 (2004). https://doi.org/10.1007/s00340-004-1665-5.

[180] 28 - Copper, Silver and Gold. In GREENWOOD, N. & EARNSHAW, A. (eds.) *Chemistry of the Elements*, 1173–1200 (Butterworth-Heinemann, Oxford, 1997), 2 edn. https://doi.org/10.1016/B978-0-7506-3365-9.50034-1.

[181] Britt, H. C. & Quinton, A. R. Alpha Particles and Protons Emitted in the Bombardment of Au^{197} and Bi^{209} by C^{12}, N^{14}, and O^{16} Projectiles. *Physical Review* **124**, 877–887 (1961). https://link.aps.org/doi/10.1103/PhysRev.124.877.

[182] Bass, R. *Nuclear Reactions with Heavy Ions* (Springer-Verlag, Berlin, Heidelberg, 1980).

[183] Druin, V. A., Polikanov, S. M. & Flerov, G. N. Fission of Nuclei under the Influence of Accelerated Nitrogen Nuclei. *Soviet Physics JETP* **5**, 1298–1304 (1957). http://jetp.ras.ru/cgi-bin/dn/e_005_06_1059.pdf.

[184] Polikanov, S. M. & Druin, V. A. Fission Induced in Heavy Elements by Carbon, Nitrogen, and Oxygen Nuclei. *Soviet Physics JETP* **36**, 744–747 (1959). http://jetp.ras.ru/cgi-bin/dn/e_009_03_0522.pdf.

[185] Quinton, A. R., Britt, H. C., Knox, W. J. & Anderson, C. E. The Fission of Gold by Oxygen Nuclei. *Nuclear Physics* **17**, 74–88 (1960). https://doi.org/10.1016/0029-5582(60)90102-4.

[186] Blann, H. M. Fission of Gold with 112-MeV C12 Ions: A Yield-Mass and Charge-Distribution Study. *Physical Review* **123**, 1356 (1961). https://doi.org/10.1103/PhysRev.123.1356.

[187] King, M., Gray, R. J., Powell, H. W., Capdessus, R. & McKenna, P. Energy exchange via multi-species streaming in laser-driven ion acceleration. *Plasma Physics and Controlled Fusion* **59**, 014003 (2017). https://doi.org/10.1088/0741-3335/59/1/014003.

[188] Nishiuchi, M. *et al.* Acceleration of highly charged GeV Fe ions from a low-Z substrate by intense femtosecond laser. *Physics of Plasmas* **22**, 033107 (2015). http://dx.doi.org/10.1063/1.4913434.

[189] Hata, M. *et al.* Creation of highly charged gold ion beam through collisional ionizations in a dense gold plasma driven by a femtosecond petawatt laser. *Physical Review Research* **7**, 033200 (2025). https://link.aps.org/doi/10.1103/8k98-6q48.

[190] Slater, J. C. Atomic radii in crystals. *The Journal of Chemical Physics* **41**, 3199–3204 (1964). https://doi.org/10.1063/1.1725697.

[191] Gordon, G. E., Larsh, A. E., Sikkeland, T. & Seaborg, G. T. Fission of Gold by Carbon Ions. *Physical Review* **120**, 1341–1348 (1960). https://doi.org/10.1103/PhysRev.120.1341.

[192] Britt, H. C. & Quinton, A. R. Fission of Au-197 and Bi-209 by C-12 and O-16 Projectiles. *Physical Review* **120**, 1768–1777 (1960). https://doi.org/10.1103/PhysRev.120.1768.

[193] Kruger, P. & Sugarman, N. High-energy fission of heavy elements. Nuclear charge dependence. *Physical Review* **99**, 1459–1469 (1955). https://doi.org/10.1103/PhysRev.99.1459.

[194] Hudis, J. & Katcoff, S. High-energy-proton fission cross sections of U, Bi, Au, and Ag measured with mica track detectors. *Physical Review* **180**, 1122–1130 (1969). https://doi.org/10.1103/PhysRev.180.1122.

[195] Rosenmund, P. *Incidence and Viewing Angle Dependence for Light Output of Scintillator Screens.* Bachelor's thesis, Ludwig-Maximilians-Universität (2025).

[196] Boller, P. *et al.* First on-line detection of radioactive fission isotopes produced by laser-accelerated protons. *Scientific Reports* **10**, 1–9 (2020). https://doi.org/10.1038/s41598-020-74045-5.

[197] Krushelnick, K. *et al.* Ultrahigh-intensity laser-produced plasmas as a compact heavy ion injection source. *IEEE Transactions on Plasma Science* **28**, 1110–1155 (2000). `http://ieeexplore.ieee.org/document/893296/`.

[198] Gales, S. *et al.* The extreme light infrastructure—nuclear physics (ELI-NP) facility: new horizons in physics with 10 PW ultra-intense lasers and 20 MeV brilliant gamma beams. *Reports on Progress in Physics* **81**, 094301 (2018). `https://dx.doi.org/10.1088/1361-6633/aacfe8`.

Danksagung

CALA ist ein wunderbarer Ort für eine Promotion mit einer tollen Mischung aus Fordern und Fördern. An dieser Stelle möchte ich mich bei ein paar Menschen bedanken, die nicht müde wurden mich zu fördern (fordern tut eine Anlage wie der ATLAS-3000 einen ganz automatisch).

Allen voran gilt mein größter Dank Prof. Peter Thirolf, durch den diese Arbeit überhaupt erst möglich geworden ist. Peter hat mir in meiner Promotion das perfekte Umfeld geschaffen, in dem ich mich wissenschaftlich frei entfalten konte und gleichzeitig immer auf seine unermüdliche und wertvolle Unterstützung zählen konnte, wenn er mir mit viel Geduld meine immer gleichen Fragen zu Kernspaltung erklärt hat und mich bei der Experimentplanung und Datenauswertung mit seinem Rat immer hat besser werden lassen. Danke Peter, für dein Vertrauen und die vielen Möglichkeiten, meine Arbeit auf internationalen Konferenzen vorzustellen. Ebenfalls sehr herzlich bedanken möchte ich mich bei Prof. Jörg Schreiber für die Übernahme des Zweitgutachtens dieser Arbeit, für die vielen bereichernden und anregenden Diskussionen und Ratschläge, aber auch dafür, dass er mit LION eine tolle Arbeitsgruppe aufgebaut hat, die mich lieb aufgenommen und mich und uns bei HF immer unterstützt haben.

Ebenfalls zu erwähnen ist Prof. Stefan Karsch, der mit seinem "Studentenlaser" ATLAS-3000 das Licht für diese Arbeit zur Verfügung gestellt hat, als auch seiner gesamten Arbeitsgruppe. Einen Petawattlaser hauptsächlich von Studenten betreiben zu lassen ist eine weltweit einzigartige Möglichkeit zur Ausbildung der zukünftigen Generation von Wissenschaftlern, die Mut, Geduld und wahrscheinlich Gelassenheit der Verantwortlichen erfordert, wofür ich sehr dankbar bin. In diesem Zusammenhang möchte ich mich auch bei Martin Gross, Hans, Florian Saran, Nik, Oli und vor allem Gregor für ihre Unterstützung bedanken.

Danke an EG, die bereits so viel Arbeit in den Aufbau von HF gesteckt hat, sodass ich direkt von Anfang an Ionen beschleunigen konnte und an Max, der unser Team dann verstärkt hat. Ohne euch wären die vielen Strahlzeiten nicht möglich gewesen. Ebenfalls erwähnen möchte ich meinen Vorgänger Florian Lindner für tolle Vorarbeit, ohne die meine Promotion nicht zu ihrem heutigen Stand hätte kommen können. Auch hier sei nochmal (wie immer) erwähnt, wie schade es ist, dass wir nicht länger Überlapp am Lehrstuhl

hatten. Ich hatte auch das Vergnügen während meiner Promotion tolle Studenten betreuen zu dürfen. Allen voran Vroni, die mich als Masterstudentin maßgeblich unterstützt hat und über deren Abschluss ich auch menschlich unglaublich froh und stolz bin. Ebenso wie meine Bachelorstudenten Vitus, Ming-Yang und Liam, die alle tolle Arbeit geleistet haben, sowie Runjia und Jinbao, die unser Team auf Zeit ergänzt haben.

Ich hatte das große Glück während meiner gesamten Promotion stets im engen Kontakt mit dem gesamten Team von LION zu stehen. Ich möchte mich sowohl bei unseren Eternals Thomas, Jens, Johannes und Martin Speicher bedanken, als auch bei allen noch aktiven um Sonja, Lenny, Michi, Flo Schweiger, Anna, Julia, Timo und Lianren, als auch bei Felix bedanken für die tolle Arbeitsatmosphäre auf unserem Gang. Darüber hinaus ist es eine tolle Erfahrung, wenn aus Kollegen Freunde werden. Danke Martin, dass du immer eingesprungen bist, falls die Gefahr auf Unterhopfung bestand. Ganz besonders erwähnen möchte ich auch meine tolle Coffee Crew, Sonja und Lenny. Ohne Lenny wäre nicht nur CALA nicht zu denken, gleiches gilt für meine Promotion. Danke für dein tiefgehendes Wissen von Physik, aber auch von Technik im allgemeinen, dass du nicht müde wirst mit unglaublicher Geduld und Begeisterung zu teilen. Einer der besten Tage meiner Promotion ist wahrscheinlich der Tag, an dem Sonja mich gefragt hat, ob ich in ihr Büro ziehen möchte, dass immer ein sicherer Hafen für geteiltes, albernes giggeln oder ernsthafte, bereichernde Diskussionen wurde. Dass Lelo uns als das 'work couple' bezeichnet, fasst es perfekt zusammen.

Da ich dank Peter meine Arbeit auf vielen Konferenzen vorstellen durfte möchte ich mich auch bei meinen Kollegen aus Dresden als auch aus Darmstadt bedanken, durch die ich mich nie alleine gefühlt habe und die meine Arbeit bereichert haben, genauso wie bei den Darmstädter Füsikern, ohne die ich es nicht durch die ersten Jahre des Studiums geschafft hätte.

Neben der ganzen Arbeit habe ich das große Glück von Leuten umgeben zu sein, die immer wieder für meinen privaten Ausgleich sorgen. Danke an Martin Schanz, der zusammen mit Philipp dafür gesorgt hat, das Physikstudium cool aussehen zu lassen, mich als mein Trainer selten fallen gelassen hat und von dem ich darüber hinaus viel gelernt habe, genauso wie vom Rest der Turner. Auch ohne meine Mädels hätte ich nicht den nötigen Ausgleich zur Physik gehabt. Danke für unsere Freundschaft an Anna, Julia, Leoni und allen voran Laura, die nicht müde wurde mich sanft zu ermahnen, falls ich "Wie geht es dir?"-Fragen zu lange ignoriert habe.

Ich möchte mich bei Uta und Oliver bedanken, die mich mit sehr viel Wärme aufgenommen haben. Meine eigene Familie ist die Säule meines Lebens und ich bin dankbar für

das Nest aus dem ich komme, auch wenn nicht mehr alle diese Arbeit erleben können. Ich möchte mich bei Opa Staudt und Omama entschuldigen, für die ich mir in den letzten Monaten zu wenig Zeit genommen habe und die alle meine Schritte mit so viel Liebe verfolgen. Es gibt niemanden, auf den ich so stolz bin, wie auf meinen kleinen Bruder. Martinlein, ich bin so froh, dass es dich gibt und wir uns immer haben werden, egal was passiert. Während ich meinem Vater wahrscheinlich meine Zuneigung für Physik und meine ruhige Art habe zu verdanken habe, habe ich von meiner Löwen-Mama ihre Wärme, Stärke und Mut, mit der sie mich durchs Leben trägt und beschützt. Ich hätte es nicht besser treffen können.

Und das beste kommt bekanntlich zum Schluss: Leonard ich möchte dir von ganzem glühenden Herzen dafür danken, dass du an meiner Seite bist, mich immer unterstützt und mir Liebe und Zuneigung schenkst. Danke, dass sich der Alltag mit dir nach dem größten Abenteuer meines Lebens anfühlt. Ich freue mich so sehr auf alles, was noch kommt!

Publications and Conference Contributions

Journal articles

- Jianhui Bin, Lieselotte Obst-Huebl, Jian-Hua Mao, Kei Nakamura, **Laura D. Geulig**, Hang Chang, Qing Ji, Li He, Jared De Chant, Zachary Kober, Anthony J. Gonsalves, Stepan Bulanov, Susan E. Celniker, Carl B. Schroeder, Cameron G. R. Geddes, Eric Esarey, Blake A. Simmons, Thomas Schenkel, Eleanor A. Blakely, Sven Steinke and Antoine M. Snijders *Scientific Reports* **12**, 1484 (2022)

- **Laura D. Geulig**, Lieselotte Obst-Huebl, Kei Nakamura, Jianhui Bin, Qing Ji, Sven Steinke, Antoine M. Snijders, Jian-Hua Mao, Eleanor A. Blakely, Anthony J. Gonsalves, Stepan Bulanov, Jeroen van Tilborg, Carl B. Schroeder, Cameron G. R. Geddes, Eric Esarey, Markus Roth and Thomas Schenkel *Review of Scientific Instruments* **93**, 103301 (2022)

- Masoud Afshari, Stuart Morris, **Laura D. Geulig**, Zahra M. Chitgar, Paul Gibbon, Peter G. Thirolf and Jörg Schreiber *Scientific Reports* **12**, 18260 (2022)

- Walid Redjem, Ariel J. Amsellem, Frances I. Allen, Gabriele Benndorf, Jianhui Bin, Stepan Bulanov, Eric Esarey, Leonard C. Feldman, Javier Ferrer Fernandez, Javier Garcia Lopez, **Laura Geulig**, Cameron R. Geddes, Hussein Hijazi, Qing Ji, Vsevolod Ivanov, Boubacar Kanté, Anthony Gonsalves, Jan Meijer, Kei Nakamura, Arun Persaud, Ian Pong, Lieselotte Obst-Huebl, Peter A. Seidl, Jacopo Simoni, Carl Schroeder, Sven Steinke, Liang Z. Tan, Ralf Wunderlich, Brian Wynne and Thomas Schenkel *Communications Materials* **4**, 22 (2023)

- Nils Weiße, Leonard Doyle, Johannes Gebhard, Felix Balling, Florian Schweiger, Florian Haberstroh, **Laura D. Geulig**, Jinpu Lin, Faran Irshad, Jannik Esslinger, Sonja Gerlach, Max Gilljohann, Vignesh Vaidyanathan, Dennis Siebert, Andreas Münzer, Gregor Schilling, Jörg Schreiber, Peter G. Thirolf, Stefan Karsch and Andreas Döpp *High Power Laser Science and Engineering* **11**, e44 (2023)

Conference Proceedings

- Veronika Kratzer, **Laura D. Geulig**, Erin G. Fitzpatrick, Florian H. Lindner, Vitus Magin, Maximilian J. Weiser and Peter G. Thirolf: Spectroscopic real-time temperature diagnostic for laser-heated thin gold foils. In *SPIE Optics + Optoelectronics, Applying Laser-driven Particle Acceleration III* **12582**, 1258307 (2023)

Conference contributions

- **Oral:** Spectroscopic Real Time Temperature Diagnostic for Laser Heated Thin Gold Foils. *Targetry for High Repetition Rate Laser-Driven Sources Workshop 5*, Dresden (Germany), 2021
- **Oral:** Update on the Laser-Driven Heavy Ion Acceleration at CALA. *42nd International Workshop on High- Energy-Density Physics with Intense Ion and Laser Beams*, Hirschegg (Austria) - virtual, 2022
- **Oral:** Update on the laser heavy ion acceleration at CALA. *Spring meeting of the German Physical Society*, Erlangen (Germany) - virtual, 2022
- **Oral:** Update on the laser heavy ion acceleration at CALA. *9th International Conference on Ultrahigh Intensity Lasers*, Jeju Island (Republic of Korea), 2022.
- **Oral:** Online Charge Measurement for Petawatt Laser-Driven Ion Acceleration. *Beam-Line & Instrumentation for Laser-Driven Particle Acceleration 5*, Garching (Germany), 2022
- **Oral:** Laser-Driven Acceleration of Gold Ions. *Spring meeting of the German Physical Society, SAMOP*, Hannover (Germany), 2023
- **Oral:** Group report: Laser-Driven Acceleration of Gold Ions. *Spring meeting of the German Physical Society, SMuK*, Dresden (Germany), 2023
- **Oral:** Towards the fission-fusion reaction mechanism. *Applying Laser-driven Particle Acceleration III*, Prague (Czech Republic), 2023
- **Oral:** Laser-Driven Acceleration of Gold Ions at the Centre for Advanced Laser Applications. *44th International Workshop on High- Energy-Density Physics with Intense Ion and Laser Beams*, Hirschegg (Austria), 2024

- **Oral:** Laser-Driven Acceleration of Gold Ions at the Centre for Advances Laser Applications. *10^{th} International Conference on Ultrahigh Intensity Lasers*, Cozumel (Mexico), 2024
- **Oral:** Acceleration of In-Target Fission Fragments with the ATLAS-3000 Laser System. *45^{th} International Workshop on High- Energy-Density Physics with Intense Ion and Laser Beams*, Hirschegg (Austria), 2025

Supervised theses

- **Bachelor's thesis** *Vitus X. K. Magin* Commissioning of the nano-Foil Target Positioning System, 2023
- **Bachelor's thesis** *Ming-Yang Hsu* Implementation of a Monitor for Electromagnetic Pulses at the High-Fields Cave of the Centre for Advanced Laser Applications (CALA), 2024
- **Bachelor's thesis** *Liam Desai* Characterization of Electromagnetic Pulses (EMPs) during Laser-Driven Ion Acceleration, 2024
- **Master's thesis** *Veronika Kratzer* Enhancing the Efficiency of Laser-Based Heavy Ion Acceleration by Radiative Target Heating, 2024